Effect of Iron on Photocatalytic Properties of Titanium Dioxide

A thesis by

Md Elias Mollah (student ID: 18256404)

Submitted in fulfilment of the requirements for the degree of

Doctor of Philosophy (PhD)

Supervisors

Professor Janusz Nowotny (WSU)

Associate Professor Tadeusz Bak (WSU)

Professor Mihail Ionescu (ANSTO)

Dr Armand Atanacio (ANSTO)

Chair of the solar energy technology advisory panel

Professor Bill Price (WSU)

SOLAR ENERGY TECHNOLOGIES GROUP

SCHOOL OF COMPUTING, ENGINEERING AND MATHEMATICS

WESTERN SYDNEY UNIVERSITY (WSU), AUSTRALIA

SEPTEMBER 2019

Dedication

Dedicated to my parents whom I love the most.

Acknowledgements

I have been waiting for this great moment over the last four and half years. It has certainly been made possible with the help and support of my supervisors, colleagues, friends, and most importantly, family members. During this time span, I have learned the science and also to be a good human being from the people surrounding me. It was a difficult path in the beginning of my study, however, I have enjoyed every moment in learning this new knowledge.

First of all, I would like to thank my principal supervisor, Professor Janusz Nowotny, for sharing his abundant knowledge, guidance, and encouragement to carry out the research. He was so supportive throughout my study. I always spent quality time with him discussing the research and data interpretations.

I also thank my supervisor, Associate Professor Tadeusz Bak. He helped me a lot from the very beginning of my candidature and on the first day in the solar energy lab. I would be in the lab still now without his assistance. He taught me the practicalities of the work in hand, installing a new set up, repairing the furnace and so on.

I would like to thank Professor Mihail Ionescu and Dr. Armand Atanacio for their great assistance. We spent a lot of time talking over the telephone in analysing raw data. This really alleviated my work and as a result I am here. I also need to thank ANSTO (Australia's Nuclear Science and Technology Organization) for letting me use their facilities, such as PIXE and SEM.

My special thanks go to Professor Bill Price, chair of the solar energy technology advisory panel, for his advices on this PhD project.

I want to thank my colleagues, Dr. Abdul Alim and Dr Kazi Akikur Rahman, who inspired and motivated me throughout my studies. I am indebted to my parents and my beautiful wife. Their love, motivation and support always embolden me in every stage of life.

Statement of authentication

The work presented in this thesis is, to the best of my knowledge and belief, original except as acknowledged in the text. I hereby declare that I have not submitted this material, either in full or in part, for a degree at this or any other institution.

.....

Md Elias Mollah

Table of Contents

List of tables

List of figures and illustrations

Notations

A	Acceptor
CB	Conduction band
C_o	Initial concentration of methylene blue solution [mol/L]
C_t	Concentration of methylene blue solution after time t [mol/L]
D	Donor
α	Optical absorption coefficient [m^{-1}]
EDX	Energy dispersive X-ray
ESR	Electron spin resonance
E_A	Acceptor energy level [eV]
E_F	Fermi level [eV]
E_g	Band gap [eV]
hv	Photon energy [eV]
ΔH_{seg}	The heat enthalpy of segregation [J/kg]
ICP	Inductively coupled plasma
σ	Electrical conductivity [$\Omega^{-1}m^{-1}$]
λ	Wavelength [nm]
K	Rate constant [min^{-1}]
KPPs	Key performance related properties
MB	Methylene blue
PIXE	Proton-induced X-ray emission
$p(O_2)$	Oxygen activity [Pa]
R	Reflectance
k_B	Boltzmann constant [J/K]
SEM	Scanning electron microscopy
SIMS	Secondary ion mass spectrometry
s	Scattering coefficient [m^{-1}]
T	Temperature [K]
t	Reaction time [min.]
TEM	Transmission electron microscopy
UV-Vis	Ultraviolet-Visible
VB	Valence band
XPS	X-ray photoelectron spectroscopy
X_1^s	The surface molar fraction of the solute
X_1^b	The bulk molar fraction of the solute
X_2^s	The surface molar fraction of the solvent
X_2^b	The bulk molar fraction of the solvent
XRD	X-ray diffraction

Postulation of the thesis

The PhD thesis postulates that the solar-to-chemical energy conversion of nonstoichiometric compounds, such as TiO_2 and its solid solutions, is profoundly influenced by atomic size structural defects (point defects).

Abstract

Technological advancements and population growth are placing enhanced stress on global energy resources. At the same time, the increasingly apparent negative effects of climate change indicate the need to generate clean energy, such as solar energy. This thesis is an attempt in making a contribution towards the development of materials for solar energy conversion.

The present technology of solar devices is focused on silicon-based solar cells. Awareness is growing, however, that titanium dioxide, TiO_2, is a promising candidate as a raw material for processing a new generation of solar materials that can be applied for solar-to-chemical energy conversion. The pioneering work of Fujishima and Honda [1] indicates that TiO_2 may be used as photo-electrode for the generation of hydrogen fuel by water oxidation. The report of Fujishima and Honda resulted in intensive studies on processing TiO_2 with enhanced performance in solar energy conversion.

TiO_2 exhibits an outstanding stability in water and, at the same time, strong reactivity with water upon UV irradiation leading to its oxidation. The main shortcoming of TiO_2 for sunlight absorption is its relatively large band gap, which is 3.0 eV and 3.2 eV for rutile and anatase, respectively, while the maximum efficiency of solar energy conversion can be achieved at 1.5 eV. Therefore, the most commonly reported research aims at reduction of the band gap of TiO_2 by incorporation of extrinsic ions [2, 3].

The recent progress in photocatalysis indicates that the efficiency of solar-to-chemical energy conversion by TiO_2-based semiconductors is determined by a range of key performance-related properties (KPPs), including the concentration of surface active sites, Fermi level, charge transport, and charge transfer, in addition to the band gap [4, 5]. All these KPPs are defect-related. Therefore, processing the TiO_2-based photocatalysts with enhanced performance imposes the need to better understand the effect of defect disorder on the reactivity of TiO_2 and its solid solutions with water.

When considering the effect of extrinsic ions on properties of TiO_2, it is important to realize that the surface composition, which is mainly responsible for photocatalytic activity, is entirely different from that of the bulk phase as a result of segregation [6]. Recognition of this effect imposes the need to understand the effect of segregation on surface vs. bulk composition of TiO_2-based solid solutions.

The present work aims at understanding the effect of extrinsic ions, specifically iron ions, on electronic structure, surface vs. bulk composition, and photocatalytic activity of TiO_2. Iron was selected as the dopant of TiO_2 for the following reasons:

- Iron exhibits lower valence than the host cation of the TiO_2 lattice (Ti^{4+}) and, therefore, forms acceptor-type defects required for water oxidation.
- Incorporation of iron results in a reduction of the band gap of TiO_2 [2, 7] and, consequently, enhances sunlight absorption.
- Iron shows a variable oxidation state, including Fe^{2+}, Fe^{3+} and Fe^{4+} [8], which may be modified by a change of oxygen activity.
- Iron exhibits surface segregation in Fe-TiO_2 [9, 10]. Therefore, iron could serve as a good template for determining the effect of processing on segregation and segregation-induced effects.

- When dissolved in water in small quantities, iron ions may contribute to the desired mineralization of drinking water.

The effect of iron on photocatalytic activity of TiO_2 has been the subject of intensive studies [2, 9]. However, the reported results on the effect of iron on photocatalytic activity of Fe-TiO_2 [7, 11] and iron segregation in TiO_2 [12, 13] are conflicting. Therefore, there is a need to clarify the conflicting reports.

The effect of iron on properties of TiO_2 discussed in the present project considers the following properties:

(1) Electronic structure

(2) Effect of segregation on surface vs. bulk composition

(3) Photocatalytic activity

The present project resulted in the following key findings:

(1) Electronic structure

- Incorporation of iron into the TiO_2 lattice results in reduction of the band gap from 3.04 eV for pure TiO_2 to 2.78 eV for Fe-doped TiO_2 involving 1.4 at% Fe.
- Increase of oxygen activity results in slight widening of the band gap. For instance, the band gap for Fe-doped TiO_2 (0.18 at%) is to 2.90 eV and 2.96 eV in reducing [$p(O_2) = 10^{-12}$ Pa] and oxidising [$p(O_2) = 100$ kPa] conditions, respectively.

(2) Surface vs. bulk composition

This project reports the effect of iron segregation in Fe-doped TiO_2 after annealing at elevated temperatures in the gas phase of controlled oxygen activity in the range of 10^{-12} Pa to 10^{5} Pa. The elemental surface analysis was performed using both

secondary ion mass spectrometry (SIMS), and X-ray photoelectron spectroscopy (XPS). The obtained results indicate that:

- The segregation-induced iron concentration at the surface increases with the increase of bulk concentration of iron.
- The segregation-induced surface iron concentration assumes maximum after annealing in reducing condition, and decreases with the increase of oxygen activity.
- The ratio of di- to tri-valent iron at the surface decreases with the increase of oxygen activity during processing.

(3) Photocatalytic activity

The photocatalytic performance of Fe-doped TiO_2 was determined from the progress of light-induced degradation of methylene blue (MB) as a testing agent. The mechanism of MB degradation was considered in terms of the predominant effect of surface active sites on water oxidation. The obtained results on the effect of oxygen activity on photocatalytic performance indicate that:

- ***Oxidising condition***. The photocatalytic activity increases for dilute solid solution (up to 0.09 at% Fe) and decreases with further incorporation of iron despite of reduced band gap.
- ***Reducing condition***. Incorporation of iron into TiO_2 lattice results in a decrease of photocatalytic activity within the entire range of iron concentrations.
- ***Variable oxygen activity***. The highest photocatalytic activity of Fe-doped TiO_2 is observed for the samples annealed in pure oxygen, and the lowest for the samples annealed in the conditions corresponding to the n-p transition point, where the charge transport assumes the minimum value.

References

1. Fujishima, A. and K. Honda, *Electrochemical Photolysis of Water at a Semiconductor Electrode.* Nature, 1972. **238**: p. 37.

2. Delekar, S.D., et al., *Structural refinement and photocatalytic activity of Fe-doped anatase TiO_2 nanoparticles.* Applied Surface Science, 2012. **263**: p. 536-545.

3. Deng, Q., et al., *Mn-doped TiO_2 nanopowders with remarkable visible light photocatalytic activity.* Materials Letters, 2011. **65**(13): p. 2051-2054.

4. Bak, T., et al., *Photocatalytic Properties of TiO_2: Evidence of the Key Role of Surface Active Sites in Water Oxidation.* The Journal of Physical Chemistry A, 2015. **119**(36): p. 9465-9473.

5. Li, W., et al., *Photocatalytic Properties of TiO_2: Effect of Niobium and Oxygen Activity on Partial Water Oxidation.* Applied Catalysis B: Environmental, 2016. **198**: p. 243-253.

6. Rahman, K.A., et al., *Towards sustainable energy: photocatalysis of Cr-doped TiO_2. 5. Effect of segregation on surface versus bulk composition.* Ionics, 2017: p. 1211-1219.

7. Fàbrega, C., et al., *Location and catalytic role of iron species in TiO_2:Fe photocatalysts: An EPR study.* Journal of Photochemistry and Photobiology A: Chemistry, 2010. **211**(2–3): p. 170-175.

8. Khan, H. and I.K. Swati, *Fe^{3+}-doped Anatase TiO_2 with d–d Transition, Oxygen Vacancies and Ti^{3+} Centers: Synthesis, Characterization, UV–vis Photocatalytic and Mechanistic Studies.* Industrial & Engineering Chemistry Research, 2016.

9. Yu, J., Q. Xiang, and M. Zhou, *Preparation, characterization and visible-light-driven photocatalytic activity of Fe-doped titania nanorods and first-principles study for electronic structures.* Applied Catalysis B: Environmental, 2009. **90**(3–4): p. 595-602.

10. Bickley, R.I., et al., *Characterisation of iron/titanium oxide photocatalysts. Part 2.—Surface studies.* Journal of the Chemical Society, Faraday Transactions, 1994. **90**(15): p. 2257-2264.

11. Ambrus, Z., et al., *Synthesis, structure and photocatalytic properties of Fe(III)-doped TiO_2 prepared from TiCl3.* Applied Catalysis B: Environmental, 2008. **81**(1–2): p. 27-37.

12. Bernasik, A., et al., *Electrical surface versus bulk properties of Fe-doped TiO_2 single crystals.* Solid State Ionics, 1994. **72**: p. 12-18.

13. Adán, C., et al., *New insights on solar photocatalytic degradation of phenol over Fe-TiO_2 catalysts: Photo-complex mechanism of iron lixiviates.* Applied Catalysis B: Environmental, 2009. **93**(1–2): p. 96-105.

CHAPTER ONE

1 Background

1.1 Introduction

Energy is needed for economic development. However, the unrestrained use of fossil-fuel based energy imposes a serious threat to the global environment, leading to climate change. There is thus an urgent need to develop new energy technologies using alternative sources of clean energy, such as solar energy.

Main stream studies in solar energy conversion is focused on photovoltaic solar cells, known as silicon-based solar cells, which are used for solar-to-electrical energy conversion. The advancement of this technology has led solar power to be more competitive over energy generated from fossil fuels. This competitiveness will arguably lead to a decrease in the use of fossil fuels in energy generation.

Another stream of research in solar energy conversion focuses on developing new generation of oxide materials, photosensitive oxide semiconductors (POSs) [1, 2], which can be used for solar-to-chemical energy conversion. Awareness is growing that the properties of POSs are profoundly influenced by lattice imperfections (point defects) which are thermodynamically reversible [3-6]. The present study focuses on the POSs, which are the most abundant functional materials.

1.2 Oxide-based semiconductors

The POSs include a range of metal oxides, such as TiO_2 [7, 8], WO_3 [9], ZnO [10], and Fe_2O_3 [11]. The present thesis is focused on TiO_2 (also known as titania) which is a promising material for solar energy conversion [8].

The photosensitivity of TiO_2 is relatively low due to its large band gap. Therefore, the research strategy to modify its properties, especially the band gap, consist in the incorporation of extrinsic ions into TiO_2, such as Fe [12, 13], Cr [14], Mn [15, 16], Ta [6], Nb [17], Co [18], V [19], Ni [20], Zn [21], W [22], Mo [23], Ir, and rare earths ions including La, Ce, Er, Pr, etc. [24].

1.3 Why TiO_2?

TiO_2 is the abundant material which is present in the form of three different crystal structures: (i) anatase (ii) rutile, and (iii) brookite. Amongst those, rutile is thermodynamically stable form of TiO_2, which is highly reactive with water and chemically stable when immersed in water. Since the pioneering experiment of Fujishima and Honda [25], showing the potential use of TiO_2 in water splitting, numerous studies have been performed to develop efficient TiO_2-based semiconductors that can be used for solar-to-chemical energy conversion [26-30], dye-sensitized solar cells [31, 32], gas sensors [33-36], air purification [37-39], and self-cleaning [40-42].

1.4 Aims

The present study aims to develop a new TiO_2-based photosensitive material for solar-to-chemical energy conversion. The current work, which is a part of the PhD

research program at the Western Sydney University, Solar Energy Technologies, investigates the electronic structure, surface vs. bulk composition and photocatalytic performance of TiO_2 and its solid solutions considering defect chemistry as an underlying framework. The aim of the present thesis is to understand the effect of iron on several defect-related properties of TiO_2, including photocatalytic activity in partial water oxidation.

References

1. Bak, T., et al., *Effect of Crystal Imperfections on Reactivity and Photoreactivity of TiO_2 (Rutile) with Oxygen, Water, and Bacteria.* The Journal of Physical Chemistry C, 2011. **115**(32): p. 15711-15738.

2. Nowotny, J., et al., *Defect chemistry and defect engineering of TiO_2-based semiconductors for solar energy conversion.* Chemical Society Reviews, 2015. **44**: p. 8424-8442.

3. Bak, T., et al., *Photocatalytic Properties of TiO_2: Evidence of the Key Role of Surface Active Sites in Water Oxidation.* The Journal of Physical Chemistry A, 2015. **119**(36): p. 9465-9473.

4. Nowotny, M., et al., *Defect chemistry of titanium dioxide. Application of defect engineering in processing of TiO_2-based photocatalysts.* The Journal of Physical Chemistry C, 2008. **112**(14): p. 5275-5300.

5. Rahman, K.A., et al., *Toward sustainable energy: photocatalysis of Cr-doped TiO_2: 1. electronic structure.* Ionics, 2017: p. 309-325.

6. Alim, M.A., et al., *Photocatalytic properties of Ta-doped TiO_2.* Ionics, 2017. **23**(12): p. 3517–3531.

7. Schneider, J., et al., *Understanding TiO_2 Photocatalysis: Mechanisms and Materials.* Chemical Reviews, 2014. **114**(19): p. 9919-9986.

8. Linsebigler, A.L., G. Lu, and J.T. Yates Jr, *Photocatalysis on TiO_2 surfaces: principles, mechanisms, and selected results.* Chemical reviews, 1995. **95**(3): p. 735-758.

9. Ashokkumar, M. and P. Maruthamuthu, *Preparation and characterization of doped WO_3 photocatalyst powders.* Journal of materials science, 1989. **24**(6): p. 2135-2139.

10. Li, D. and H. Haneda, *Morphologies of zinc oxide particles and their effects on photocatalysis.* Chemosphere, 2003. **51**(2): p. 129-137.

11. Jang, J.S., et al., *Rapid screening of effective dopants for Fe_2O_3 photocatalysts with scanning electrochemical microscopy and investigation of their photoelectrochemical properties.* The Journal of Physical Chemistry C, 2009. **113**(16): p. 6719-6724.

12. Kim, D.H., et al., *Photocatalytic behaviors and structural characterization of nanocrystalline Fe-doped TiO_2 synthesized by mechanical alloying.* Journal of Alloys and Compounds, 2004. **375**(1–2): p. 259-264.

13. Wan, L., et al., *Phase selection and visible light photo-catalytic activity of Fe-doped TiO_2 prepared by the hydrothermal method.* Materials Research Bulletin, 2011. **46**(3): p. 442-446.

14. Ould‐Chikh, S., et al., *Photocatalysis with Chromium‐Doped TiO_2: Bulk and Surface Doping.* ChemSusChem, 2014. **7**(5): p. 1361-1371.

15. Lu, L., et al., *Mn-doped TiO_2 thin films with significantly improved optical and electrical properties.* Journal of Physics D: Applied Physics, 2012. **45**(48): p. 485102.

16. Chauhan, R., A. Kumar, and R.P. Chaudhary, *Structural and photocatalytic studies of Mn doped TiO_2 nanoparticles.* Spectrochimica Acta Part A: Molecular and Biomolecular Spectroscopy, 2012. **98**: p. 256-264.

17. Li, W., et al., *Photocatalytic Properties of TiO_2: Effect of Niobium and Oxygen Activity on Partial Water Oxidation.* Applied Catalysis B: Environmental, 2016. **198**: p. 243-253.

18. Iwasaki, M., et al., *Cobalt ion-doped TiO_2 photocatalyst response to visible light.* Journal of Colloid and Interface Science, 2000. **224**(1): p. 202-204.

19. Klosek, S. and D. Raftery, *Visible light driven V-doped TiO_2 photocatalyst and its photooxidation of ethanol.* The Journal of Physical Chemistry B, 2001. **105**(14): p. 2815-2819.

20. Tseng, H.-H., et al., *Degradation of xylene vapor over Ni-doped TiO_2 photocatalysts prepared by polyol-mediated synthesis.* Chemical Engineering Journal, 2009. **150**(1): p. 160-167.

21. Zhao, Y., et al., *Zn-doped TiO_2 nanoparticles with high photocatalytic activity synthesized by hydrogen–oxygen diffusion flame.* Applied Catalysis B: Environmental, 2008. **79**(3): p. 208-215.

22. Sangkhun, W., et al., *Photocatalytic degradation of BTEX using W-doped TiO_2 immobilized on fiberglass cloth under visible light.* Superlattices and Microstructures, 2012. **52**(4): p. 632-642.

23. Devi, L.G. and B.N. Murthy, *Characterization of Mo doped TiO_2 and its enhanced photo catalytic activity under visible light.* Catalysis letters, 2008. **125**(3-4): p. 320-330.

24. Xu, A.-W., Y. Gao, and H.-Q. Liu, *The preparation, characterization, and their photocatalytic activities of rare-earth-doped TiO2 nanoparticles.* Journal of Catalysis, 2002. **207**(2): p. 151-157.

25. Fujishima, A. and K. Honda, *Electrochemical Photolysis of Water at a Semiconductor Electrode.* Nature, 1972. **238**: p. 37.

26. Adán, C., et al., *Solar light assisted photodegradation of ethidium bromide over titania-based catalysts.* Catalysis Today, 2007. **129**(1–2): p. 79-85.

27. Asahi, R., et al., *Visible-light photocatalysis in nitrogen-doped titanium oxides.* science, 2001. **293**(5528): p. 269-271.

28. Diebold, U., *The surface science of titanium dioxide.* Surface science reports, 2003. **48**(5): p. 53-229.

29. Karakitsou, K.E. and X.E. Verykios, *Effects of altervalent cation doping of titania on its performance as a photocatalyst for water cleavage.* The Journal of Physical Chemistry, 1993. **97**(6): p. 1184-1189.

30. Kesselman, J.M., et al., *Electrochemical production of hydroxyl radical at polycrystalline Nb-doped TiO_2 electrodes and estimation of the partitioning between hydroxyl radical and direct hole oxidation pathways.* The Journal of Physical Chemistry B, 1997. **101**(14): p. 2637-2643.

31. Kay, A. and M. Grätzel, *Low cost photovoltaic modules based on dye sensitized nanocrystalline titanium dioxide and carbon powder.* Solar Energy Materials and Solar Cells, 1996. **44**(1): p. 99-117.

32. Ferber, J. and J. Luther, *Modeling of photovoltage and photocurrent in dye-sensitized titanium dioxide solar cells.* The Journal of Physical Chemistry B, 2001. **105**(21): p. 4895-4903.

33. Carotta, M.C., et al., *Vanadium and tantalum-doped titanium oxide (TiTaV): a novel material for gas sensing.* Sensors and Actuators B: Chemical, 2005. **108**(1–2): p. 89-96.

34. Zhu, Y., et al., *Development of a gas sensor utilizing chemiluminescence on nanosized titanium dioxide.* Analytical Chemistry, 2002. **74**(1): p. 120-124.

35. Yamazoe, N., Y. Kurokawa, and T. Seiyama, *Effects of additives on semiconductor gas sensors.* Sensors and Actuators, 1983. **4**: p. 283-289.

36. Savage, N.O., S.A. Akbar, and P.K. Dutta, *Titanium dioxide based high temperature carbon monoxide selective sensor.* Sensors and Actuators B: Chemical, 2001. **72**(3): p. 239-248.

37. Hager, S. and R. Bauer, *Heterogeneous photocatalytic oxidation of organics for air purification by near UV irradiated titanium dioxide.* Chemosphere, 1999. **38**(7): p. 1549-1559.

38. Nonami, T., H. Hase, and K. Funakoshi, *Apatite-coated titanium dioxide photocatalyst for air purification.* Catalysis Today, 2004. **96**(3): p. 113-118.

39. Ramirez, A.M., et al., *Titanium dioxide coated cementitious materials for air purifying purposes: preparation, characterization and toluene removal potential.* Building and Environment, 2010. **45**(4): p. 832-838.

40. Paz, Y., et al., *Photooxidative self-cleaning transparent titanium dioxide films on glass.* Journal of Materials Research, 1995. **10**(11): p. 2842-2848.

41. Benedix, R., et al., *Application of titanium dioxide photocatalysis to create self-cleaning building materials.* Lacer, 2000. **5**: p. 157-168.

42. Watanabe, T., et al., *Photocatalytic activity and photoinduced hydrophilicity of titanium dioxide coated glass.* Thin solid films, 1999. **351**(1): p. 260-263.

CHAPTER TWO

2 Definition of terms

The present chapter provides the definition of basic terms used in the present thesis, including defect disorder of pure and Fe-doped TiO_2 and several defect-related properties, such as electronic structure, segregation and photocatalytic activity in partial water oxidation.

2.1 Defect chemistry

All crystals, including oxide crystals, are defected. The point defects are responsible for nonstoichiometric of metal oxides. These intrinsic defects, which are formed by interactions between the oxide lattice and gaseous oxygen, include oxygen vacancies, cation vacancies, and cation interstitials. Extrinsic defects refer to the presence of unintentional dopants (impurities) or intentional dopants, such as iron, chromium, and tantalum. It has been reported that defect engineering can be applied in processing an efficient photocatalyst with enhanced solar-to-chemical energy conversion [1-3].

2.1.1 Defect disorder of TiO_2

Nonstoichiometric compounds, such as TiO_2, exhibit a wide range of ionic defects, including oxygen vacancies, titanium vacancies, and titanium interstitials as well as electronic defects, such as quasi-free electrons and electron holes [4-7]. The notation for point defects and their meanings are presented in **Table 2-1** using the symbols

proposed by Kröger and Vink [8]. The defect reactions must satisfy the balances of mass, site ratio and charge.

Table 2-1: Intrinsic lattice defects in TiO_2 with Kröger-Vink notation [8].

Defect equilibria		Kröger-Vink notation	Descriptions
$O_O^x \leftrightarrow V_O^{\bullet\bullet} + 2e' + \frac{1}{2}O_2$	**(2-1)**	O_O^X	O^{2-} ion in oxygen sub-lattice of TiO_2
		$V_O^{\bullet\bullet}$	Doubly ionized oxygen vacancy
		Ti_{Ti}^x	Ti^{4+} ion in the titanium sub-lattice
$Ti_{Ti}^x + 2O_O^x \leftrightarrow Ti_i^{\bullet\bullet\bullet} + 3e' + O_2$	**(2-2)**	$Ti_i^{\bullet\bullet\bullet}$	Ti^{3+} ion located in interstitial site
		$Ti_i^{\bullet\bullet\bullet\bullet}$	Ti^{4+} ion located in interstitial site
$Ti_{Ti}^x + 2O_O^x \leftrightarrow Ti_i^{\bullet\bullet\bullet\bullet} + 4e' + O_2$	**(2-3)**	V_{Ti}''''	Fully ionized titanium vacancy
$O_2 \leftrightarrow V_{Ti}'''' + 4h^{\bullet} + 2O_O^x$	**(2-4)**	e'	Quasi-free electron located on the Ti^{3+} ion in the titanium sub-lattice
$nil \leftrightarrow e' + h^{\bullet}$	**(2-5)**	$h^{\bullet}$	Quasi-free electron hole located on the O^- ion in the oxygen sub-lattice

Defect disorder is described by equilibrium constants and the charge neutrality. The equilibrium constants for the reactions **(2-1)** - **(2-5)** are defined in equations **(2-6)** to **(2-10)** by $K_1 - K_i$, respectively [2, 9]:

$$K_1 = [V_O^{\bullet\bullet}]n^2 p(O_2)^{1/2} \quad \textbf{(2-6)}$$

$$K_2 = [Ti_i^{\bullet\bullet\bullet}]n^3 p(O_2) \quad \textbf{(2-7)}$$

$$K_3 = [Ti_i^{\bullet\bullet\bullet\bullet}]n^4 p(O_2) \quad \textbf{(2-8)}$$

$$K_4 = [V_{Ti}'''']p^4 p(O_2)^{-1} \quad \textbf{(2-9)}$$

$$K_i = np \quad \textbf{(2-10)}$$

The square brackets denote the concentration of ionic defects, the concentration of electrons and electron holes are denoted by n and p, respectively and $p(O_2)$ represents the oxygen activity. The charge neutrality for pure TiO_2 and its solid solutions with singly ionised donors, $D^{\bullet}$, and acceptors, A', is represented by equations **(2-11)** and **(2-12)**, respectively:

$$2[V_O^{\bullet\bullet}] + 3[Ti_i^{\bullet\bullet\bullet}] + 4[Ti_i^{\bullet\bullet\bullet\bullet}] + p = n + 4[V_{Ti}^{''''}] \quad \textbf{(2-11)}$$

$$2[V_O^{\bullet\bullet}] + 3[Ti_i^{\bullet\bullet\bullet}] + 4[Ti_i^{\bullet\bullet\bullet\bullet}] + [D^{\bullet}] + p = n + 4[V_{Ti}^{''''}] + [A'] \quad \textbf{(2-12)}$$

Using the expressions **(2-6) - (2-10)** and the condition **(2-12),** the effect of oxygen activity on the concentration of electrons can be described as follows:

$$4K_4K_i^{-4}p(O_2)n^8 + n^5 - ([D^{\bullet}] - (A'])n^4 - K_i n^3 - 2K_1 p(O_2)^{-1/2} n^2 - 3K_2 p(O_2)^{-1} n - 4K_3 p(O_2)^{-1} = 0 \quad \textbf{(2-13)}$$

Equation **(2-13)** can be used for the derivation of defect disorder diagram, shown in **Figure 2-1a.** As seen from the above equation **(2-13),** the concentration of electrons depends on oxygen activity and the equilibrium constants for all defect reactions.

As seen in **Figure 2-1a**, TiO_2 at 1273 K in the oxygen activity of $p(O_2)$ = 14 kPa is an amphoteric semiconductor that exhibits comparable concentrations of electrons and holes. Consequently, TiO_2 equilibrated at 1273 K with oxygen activity $p(O_2)$ > 14 kPa and $p(O_2)$ < 14 kPa is a p- and n-type semiconductor, respectively.

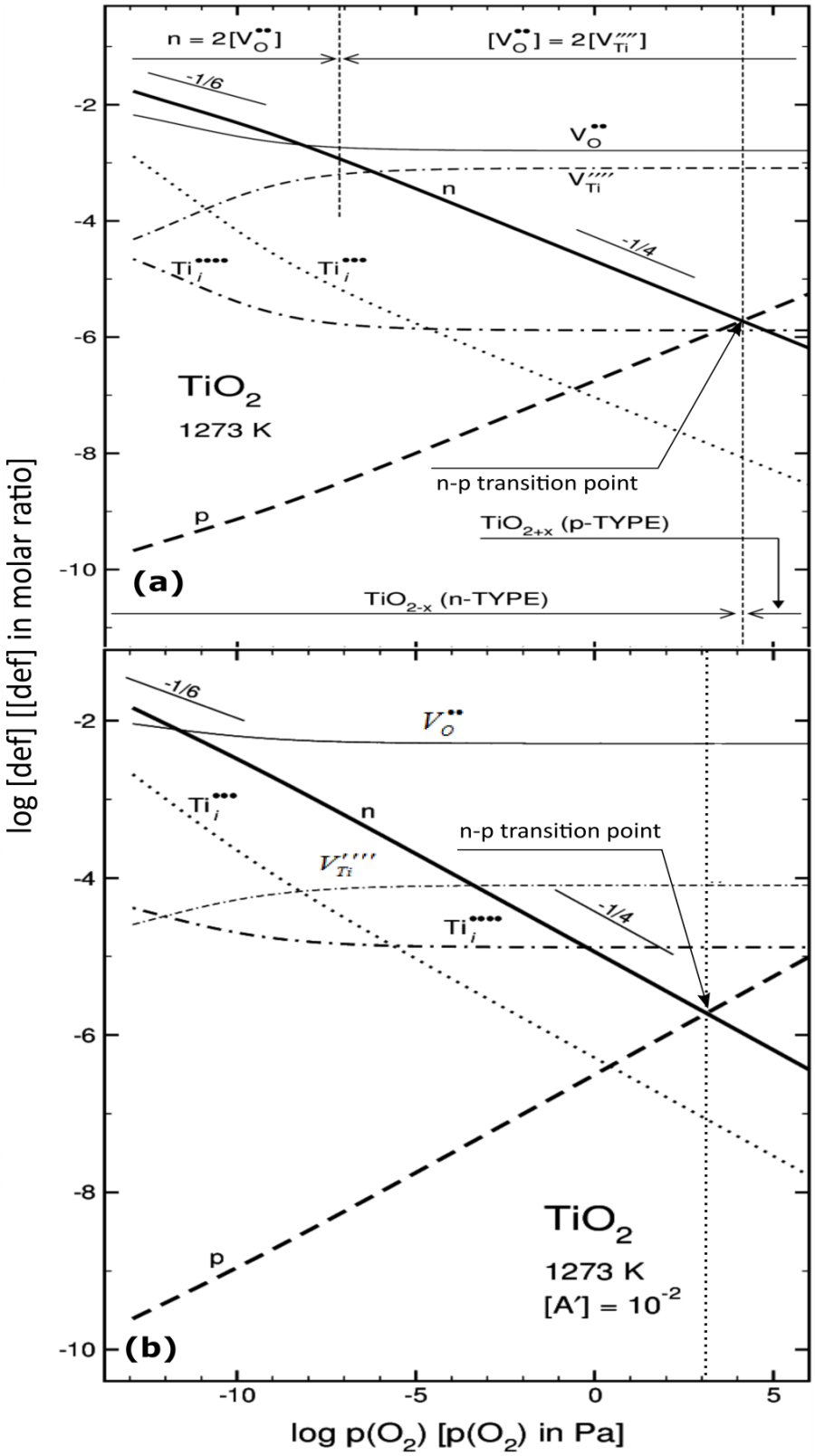

Figure 2-1: The effect of oxygen activity on the concentration of electronic and ionic defects in (a) pure TiO_2, and (b) TiO_2 doped with 1 at% of singly ionised acceptor at 1273 K.

The effect of singly ionized substitutional acceptor species, which are negatively charged, is shown in **Figure 2-1b**, assuming $[D^{\bullet}]$ = 0 at% and $[A']$ = 1 at%. As depicted, the incorporation of acceptor-type ions into TiO_2 results in the following changes of defect disorder:

(i) Shift of the n-p transition point towards lower $p(O_2)$.

(ii) Lowering the concentration of titanium vacancies.

2.1.2 Defect disorder of Fe-doped TiO_2

Iron can be incorporated into TiO_2 lattice according to a range of mechanisms. Iron ions can enter into host lattice through substitutional or interstitial mechanisms and form the associated defects that are needed to satisfy the charge neutrality condition. The commonly reported mechanism consists in the incorporation of tri-valent iron ions into titanium sites [10]:

$$Fe_2O_3 \leftrightarrow 2Fe'_{Ti} + V_O^{\bullet\bullet} + 3O_O^x \qquad \textbf{(2-14)}$$

This defect disorder is governed by the ionic charge compensation:

$$[Fe'_{Ti}] = 2[V_O^{\bullet\bullet}] \qquad \textbf{(2-15)}$$

At high oxygen activity, tri-valent iron ions may also be incorporated into TiO_2 by the following mechanism:

$$Fe_2O_3 + \frac{1}{2}O_2 \leftrightarrow 2Fe'_{Ti} + 2h^{\bullet} + 4O_O^x \qquad \textbf{(2-16)}$$

In this case the defect disorder is governed by the following electronic charge compensation:

$$p = [Fe'_{Ti}] \qquad \textbf{(2-17)}$$

The incorporation of di-valent iron into TiO_2 may proceed by similar reactions:

$$FeO \leftrightarrow Fe''_{Ti} + V_O^{\bullet\bullet} + O_O^x \quad \textbf{(2-18)}$$

$$FeO + \frac{1}{2}O_2 \leftrightarrow Fe''_{Ti} + 2h^{\bullet} + 2O_O^x \quad \textbf{(2-19)}$$

These disorders are governed by the following charge neutrality conditions, respectively:

$$[Fe''_{Ti}] = [V_O^{\bullet\bullet}] \quad \textbf{(2-20)}$$

$$p = 2[Fe''_{Ti}] \quad \textbf{(2-21)}$$

The incorporation of tri-valent iron into TiO_2 may also occur into interstitial sites:

$$Fe_2O_3 + \frac{1}{2}O_2 \leftrightarrow 2Fe_i^{\bullet\bullet\bullet} + 2V''''_{Ti} + 2h^{\bullet} + 4O_O^x \quad \textbf{(2-22)}$$

$$2Fe_2O_3 \leftrightarrow 4Fe_i^{\bullet\bullet\bullet} + 3V''''_{Ti} + 6O_o^x \quad \textbf{(2-23)}$$

$$Fe_2O_3 \leftrightarrow 2Fe_i^{\bullet\bullet\bullet} + 6e' + \frac{3}{2}O_2 \quad \textbf{(2-24)}$$

These mechanisms are governed by the following charge compensations, respectively:

$$p + 3[Fe_i^{\bullet\bullet\bullet}] = 4[V''''_{Ti}] \quad \textbf{(2-25)}$$

$$3[Fe_i^{\bullet\bullet\bullet}] = 4[V''''_{Ti}] \quad \textbf{(2-26)}$$

$$n = 3[Fe_i^{\bullet\bullet\bullet}] \quad \textbf{(2-27)}$$

Analogously, incorporation of di-valent iron into TiO_2 can be considered by the following reaction:

$$FeO + \frac{1}{2}O_2 \leftrightarrow Fe_i^{\bullet\bullet} + V''''_{Ti} + 2O_O^x + 2h^{\bullet} \quad \textbf{(2-28)}$$

This defect disorder is governed by the ionic charge compensation:

$$p + 2[Fe_i^{\bullet\bullet}] = 4[V''''_{Ti}] \quad \textbf{(2-29)}$$

Equations **(2-14)** – **(2-29)** represent the effect of iron on bulk properties of TiO_2. However, the surface properties of Fe-doped TiO_2 are essentially different from the bulk owing to iron segregation [10].

Knowledge of the effect of processing conditions on the iron incorporation mechanism into TiO_2 lattice allows its properties to be modified in a controlled manner. For instance, the reaction mechanisms shown in equations **2-16**, **2-19**, **2-22**, and **2-28** result in shifting the Fermi level towards the valence band of TiO_2, which leads to an increase of anodic behaviour. The incorporation mechanism of iron into TiO_2 determines a range of its properties, such as electronic structure, surface vs. bulk composition, and photocatalytic activity, as described in **Results** and **Discussions** chapter.

2.2 Electronic structure

Band theory can be used to explain the electronic structure of the materials which are generally considered as conductors, semiconductors and insulators based on their energy gap or band gap, as schematically shown in **Figure 2-2**. The valence band and conduction band overlap in conductors. In semiconductors, the electrons from the valence band can move to the conduction band as a result of thermal, optical or electrical excitation.

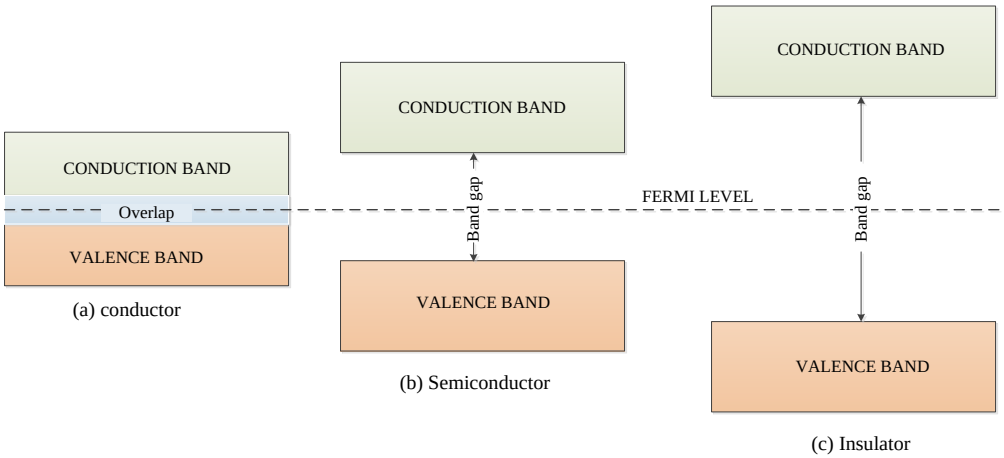

Figure 2-2: The schematic representation of the electronic structure of a conductor (a), semiconductor (b), and insulator (c).

Band gap

The smallest energy difference between the top of the valence band and bottom of the conduction band is termed band gap. When semiconductor is exposed to the light of photon energy larger than the band gap and it is absorbed, the excess of lattice energy results in a transition of electrons over the band gap. Subsequently, the photo-generated quasi-free electrons and electron holes can drive photocatalytic reactions at the solid surface. The band gap of TiO_2 (rutile) is 3.0 eV. This makes the photocatalyst efficient only under UV light. The reported band gap values for anatase and rutile is represented in **Table 2-2**.

Table 2-2: The literature data on the band gap of anatase and rutile.

References	Temp. [K], h	Phase	Transition	Approach	Band gap, E_g [eV]	Average value [eV]
Tang et al., 1994 [11]	673, 2	Anatase	Indirect	UV-Vis reflectance	3.20	3.3
Jagadale et al., 2008[12]	573, 6		---		3.44	
Wang et al., 2009 [13]	773, 1		Indirect	UV-Vis transmittance	3.29	
Lin et al., 2014 [14]	773, 1			UV-Vis transmittance	3.44	
Chen et al., 2015 [15]	773, 3			UV-Vis reflectance	3.13	
Yan et al., 2015 [16]	773, 4	Rutile	Indirect	UV-Vis absorbance	2.9	3.0
Cronomeyer et al., 1959[17]	623-1123		---	Electrical conductivity	3.05	
Gupta and Ravindra, 1980 [18]	---		----	Optical	3.03	
Rahman et al., 2018 [19]	1373, 1		Direct	UV-Vis reflectance	3.04	

Mid-gap energy levels

The reported energy levels of intrinsic defects as well as the iron energy level within the band gap are shown in **Figure 2-3**. The energy levels of the intrinsic defects were calculated theoretically [20]. As reported, oxygen vacancy forms a donor level which is around 1.18 eV below the conduction band of TiO_2 and the titanium interstitial level is approximately 1.47-1.56 eV below the conduction band. On the other hand, titanium vacancy induces an acceptor level located about 1.15 eV above the valence band of TiO_2.

Wang et al., 2010 [21] reported that Fe doping leads to the reduction of band gap of TiO_2 with the introduction of a new intermediate energy level (iron in Ti position) which is located around 0.1 eV above the valence band of TiO_2. Umebayashi et al.,

2002 [22] determined, by theoretical calculations, that the iron energy level lies 0.2 eV above the valence band of TiO_2.

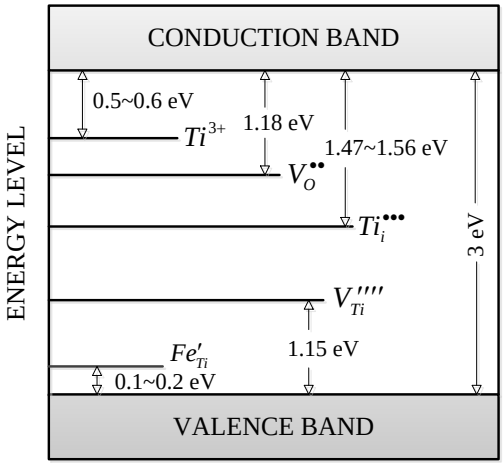

Figure 2-3: Band model of TiO_2 with intrinsic and extrinsic defects energy levels [20-22].

Valence band

The energy band, which is formed by grouping the range of energy levels of the valence electrons or outermost orbital electrons, is called the valence band.

Conduction band

The collection of energy levels associated with the free electrons (if the electrons in the valence band gain sufficient energy, they can become free electrons) is called the conduction band.

Fermi level

From the solid state chemistry perspective, charge transfer at solid/liquid interface during chemical reaction is determined by the difference between the chemical potential of electrons in solid (Fermi level) and the electron affinity of the molecule

involved in the reaction. According to the Fermi-Dirac statistics (expressed by equation 2-30), Fermi level, E_F, is the energy at which electron occupancy is 1/2:

$$f(E) = \frac{1}{1 + \exp \frac{E - E_F}{k_B T}} \qquad \textbf{(2-30)}$$

where, *f(E)* is the probability of an electron to be in energy state *E*, k_B is the Boltzmann constant, E_F is the Fermi level, and *T* is the absolute temperature.

2.3 Optical transition models

Two types of optical transitions, direct and indirect, can be considered and they are shown in **Figure 2-4.** If an electron transfers from the valence band to the conduction band without a change of its wave vector, the transition is termed as direct. When a change of the wave vector is required, the transition is termed as indirect. In this process, the absorption of both photon and phonon take place.

The light absorption coefficient is much higher for indirect transition than in direct transition as it is proportional to the square and square root of photon energy *(hν)*, respectively [23]. That clearly indicates; light of certain wavelength can penetrate more into a semiconductor before being absorbed for an indirect transition than direct transition.

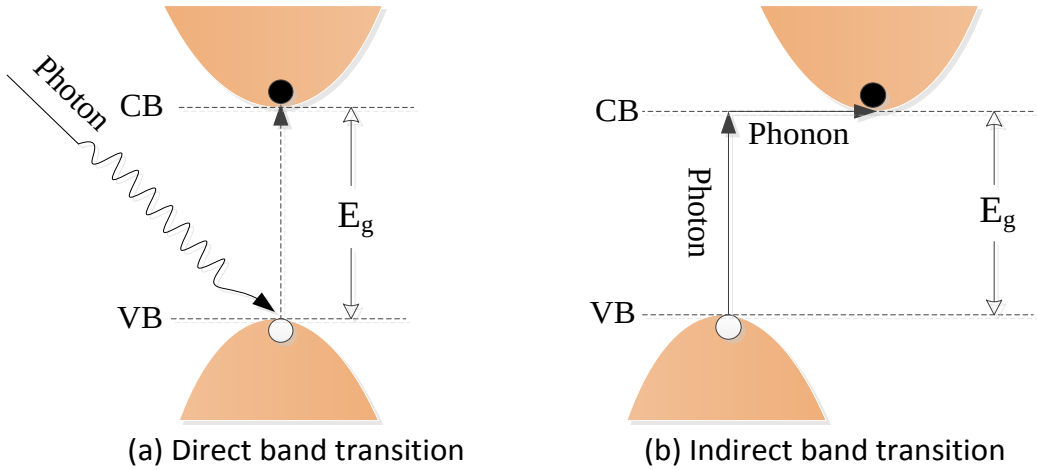

Figure 2-4: The schematic representation of optical transitions in semiconductors. VB and CB represent the valence band and conduction band, respectively. Empty circle and filled circle (black) represents the electron hole and electron, respectively.

2.4 Photocatalytic reaction mechanism of TiO_2

This section focuses on the reaction mechanism of TiO_2-based semiconductors with water, although the basic concepts are applicable for other oxide-based semiconductors as well. TiO_2 is extensively used in solar-to-chemical energy conversion systems via partial or total water oxidation. In both cases, TiO_2 is submerged into an aqueous solution and exposed to light. The reactivity of TiO_2 is influenced by several factors, such as the light energy, the composition of aqueous electrolyte in contact with the semiconductor and the properties of the semiconducting materials acting as the photocatalysts or photoelectrodes.

2.4.1 Partial water oxidation (water purification)

The concept of partial water oxidation refers to the reactivity between the adsorbed water molecules and the surface of oxide semiconductors, such as TiO_2 [24]. In the

initial step, the light-induced ionisation over the band gap of TiO_2 leads to the formation of electron-hole pair. **Figure 2-5** represents a simple model of this process.

$$h\upsilon \xrightarrow{TiO_2} h^{\bullet} + e' \qquad \textbf{(2-31)}$$

The electrons and holes then migrate to cathodic and anodic sites, respectively as subsequent reactions occur at both sites of the catalyst. At the anodic sites, water reacts with the electron holes forming hydroxyl radicals. The hydroxyl radicals have a strong ability to react with the organic contaminants present in water and decompose them into harmless products. That results in water purification. The anodic process may be represented as:

$$H_2O + h^{\bullet} \leftrightarrow H^{+} + OH^{*} \qquad \textbf{(2-32)}$$

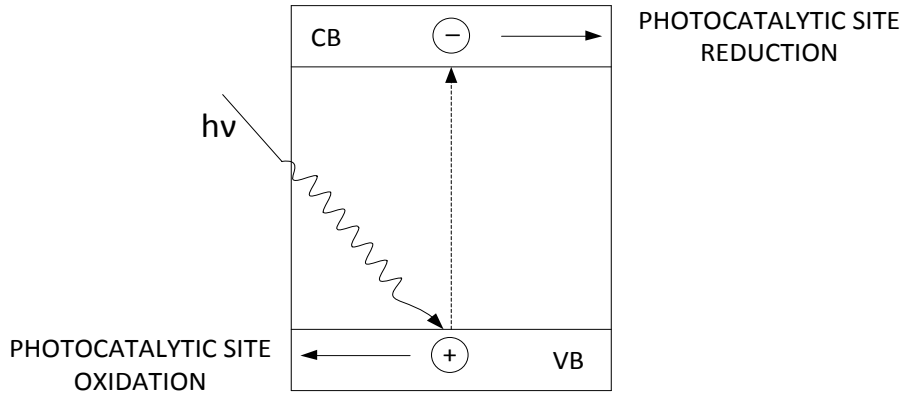

Figure 2-5: Model representing the formation of an electron-hole pairs within the surface layers of TiO_2 and their subsequent involvement in reduction and oxidation reactions.

At the cathodic sites, the reaction **(2-33)** is associated with the removal of electrons from the surface and their transfer to the surface adsorbed oxygen molecules. This process creates superoxide species which can decompose organic pollutants in water as well:

$$O_2 + e' \leftrightarrow O_2^- \quad \textbf{(2-33)}$$

2.4.2 Total water oxidation (hydrogen fuel)

In total water oxidation, the reactivity between the adsorbed molecules and the oxide semiconductor is associated with the multi-electron charge transfer [24]. **Figure 2-6** shows the schematic representation of a photo-electrochemical (PEC) cell where TiO_2 acts as a photo-anode. The incident photon of sufficient energy on absorption in TiO_2 photo-anode forms electron-hole pairs. These electrons and electron holes are separated from each other due to the presence of an electric field which forms at the interface of TiO_2 and H_2O. The photogenerated electrons in the conduction band are transported to the cathode via an external wire. The photogenerated holes are swept toward the semiconductor/electrolyte interface, where they oxidize water to form oxygen gas and hydrogen ions (H^+). At the cathode, the electrons and hydrogen ions form hydrogen gas. No additional energy sources except sunlight are used for photoelectrochemical water splitting. In practice, however, additional bias voltage may be applied to oxidise water.

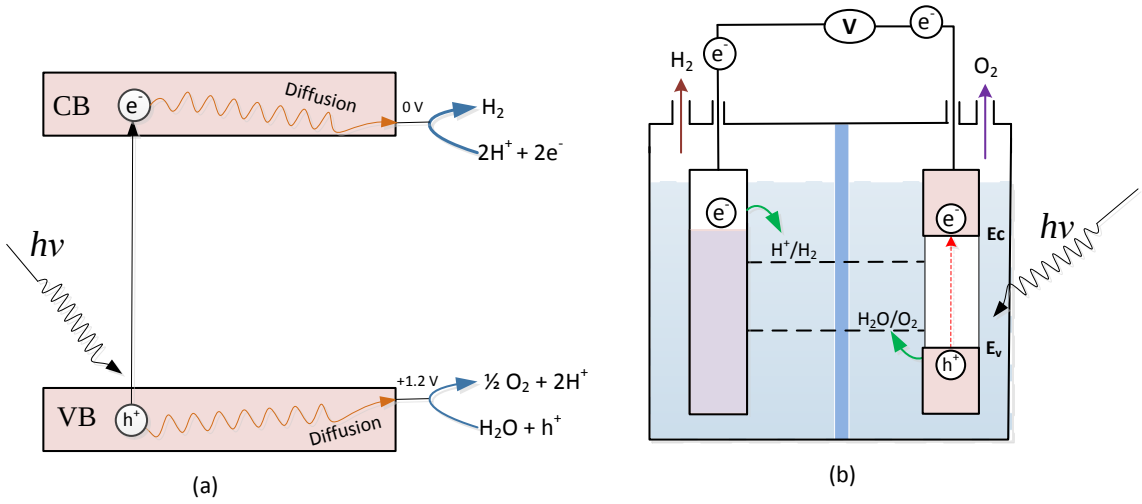

Figure 2-6: The schematic representation of water-splitting by a semiconductor where (a) oxygen and hydrogen generation reaction take place and (b) the basic principle of the hydrogen-evolving photoelectrochemical cell. Where, *hv* represents the photon energy, VB and CB represents the valence and conduction band, respectively.

2.5 Effect of key performance-related properties (KPPs) on photocatalytic performance

Photocatalytic partial water oxidation by TiO_2 is determined by the light-induced of TiO_2 with water. Overview of the literature reported data indicate that the reactivity depends on rate of properties, including:

- Band gap
- Concentration of surface active sites
- Fermi level
- Charge transport
- Band edge alignment

2.5.1 ***Band gap (KPP-1).***

The photocatalytic activity of oxide semiconductors in water oxidation is commonly reported as determined by the band gap. The effect of the band gap on the performance is considered in terms of the amount of light absorbed, which is determined by the band gap. Another word, the band gap is critical for light absorption. This is the reason why most commonly studied performance-related properties is band gap [14, 16, 25-36]. The band gap of pure TiO_2 is approximately 3 eV for rutile. On the other hand, the band gap required for maximum photocatalytic performance of TiO_2 is 1.5 eV. Therefore, there is a need to reduce the band gap of TiO_2 that can be achieved by incorporation of extrinsic ions of donor or acceptors or modification of the lattice oxygen activity. While the band gap on performance is clear, the photocatalytic activity also depends on many other properties.

2.5.2 Concentration of surface active sites (KPP-2).

The reactivity of TiO_2 and its solid solutions with water depends on the concentration of specific surface active sites. The most effective active surface active sites in water oxidation are titanium vacancies, which can provide electron holes for the anodic reactions (this sites can also remove electron from water). The concentration of these active sites can be increased by imposition of enhanced oxygen active of gas phase during processing.

2.5.3 Fermi level (KPP-3).

Fermi level is reflective of the ability of the semiconductors to accept or donate electrons, consequently, the elevation of the Fermi level results in enhanced charge

transfer during reduction reactions. Alternatively, lowering the Fermi level results in enhanced anodic reactions.

2.5.4 Charge transport (KPP-4).

The light induced electronic charge carers, which are formed beneath the surface, must be transported to the reaction sites at the surface. This process is determined by charge transport. Therefore, the charge transport has a profound effect on the photocatalytic performance.

2.5.5 Band edge alignment (KPP-5).

Band edge alignment is critical for charge transfer between the semiconductor and the redox couple in the liquid phase. **Figure 2-7** represents the charge transfer between the semiconductor (derived in terms of the flat band model) and the redox couple in water electrolyte, which allows charge transfer for both reduction and oxidation.

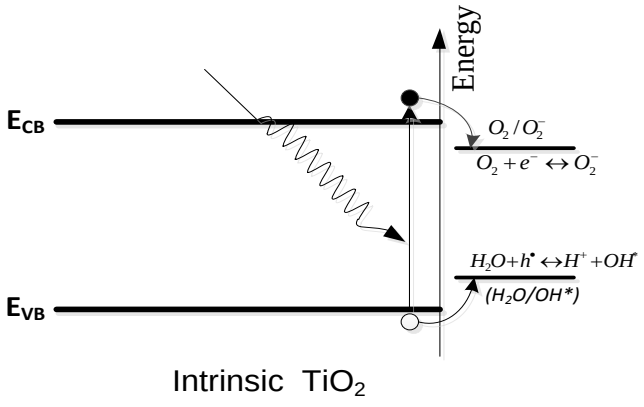

Figure 2-7: The schematic representation of the band model of intrinsic TiO_2 in water and associated redox reactions for photocatalytic water purification.

2.6 Segregation

Segregation refers to the transport of ionic species (i.e. native defects or extrinsic defects related to doping) from the bulk to the surface leading to enrichment of the surface layer in these species. The main driving forces that can influence segregation are electrostatic attraction (positive- and negative-type defect) and strain energy (lattice mismatch). As a consequence of segregation, surface properties of the catalyst differ from the bulk properties in terms of chemical composition and structure, which are affected by the following factors:

(i) ***Oxygen activity.*** It has been attested that segregation of lattice species in TiO_2 strongly depends on oxygen activity [10].

(ii) ***Annealing temperature.*** The segregation equilibrium depends on temperature. Consequently, the segregation-induced enrichment factor depends on the applied annealing temperature [37].

(iii) ***Distance from the surface.*** Segregation results in the formation of surface vs. bulk concentration gradient [10].

(iv) ***Composition.*** The enrichment factor has a tendency to increase with the decrease of the concentration of species in the bulk.

2.7 Experimental facilities for the determination of iron concentration

The present work uses a range of analytical techniques which exhibit different depth resolution and sensitivity to determine the iron concentration in Fe-doped TiO_2: SIMS, XPS and PIXE.

(a) SIMS allows to determine depth profiles of selected lattice species.

(b) XPS can be used to determine the average elemental composition within the surface layer of approximately 4-6 nm thickness.

(c) PIXE can be used to determine the bulk concentration of the selected elements.

References

1. Bak, T., et al., *Photocatalytic water disinfection on oxide semiconductors: Part 1 – basic concepts of TiO_2 photocatalysis.* Advances in Applied Ceramics, 2012. **111**(1-2): p. 4-15.

2. Bak, T., et al., *Photocatalytic Properties of TiO_2: Evidence of the Key Role of Surface Active Sites in Water Oxidation.* The Journal of Physical Chemistry A, 2015. **119**(36): p. 9465-9473.

3. Alim, M.A. and T. Bak. *Basic Concepts of Solar-to-Chemical Energy Conversion by Oxide Semiconductors*. in *Solid State Phenomena*. 2016. Trans Tech Publ.

4. Kofstad, P., *Nonstoichiometry, diffusion, and electrical conductivity in binary metal oxides*. Vol. 155. 1972: Wiley-Interscience New York.

5. Nowotny, M., et al., *Defect chemistry of titanium dioxide. Application of defect engineering in processing of TiO_2-based photocatalysts.* The Journal of Physical Chemistry C, 2008. **112**(14): p. 5275-5300.

6. Khan, S.U., M. Al-Shahry, and W.B. Ingler, *Efficient photochemical water splitting by a chemically modified n-TiO_2.* science, 2002. **297**(5590): p. 2243-2245.

7. Wang, G., Y. Ling, and Y. Li, *Oxygen-deficient metal oxide nanostructures for photoelectrochemical water oxidation and other applications.* Nanoscale, 2012. **4**(21): p. 6682-6691.

8. Kröger, F. and H. Vink, *Relations between the concentrations of imperfections in crystalline solids.* Solid state physics, 1956. **3**: p. 307-435.

9. Bak, T., et al., *Effect of Prolonged Oxidation on Semiconducting Properties of Titanium Dioxide.* The Journal of Physical Chemistry C, 2008. **112**(34): p. 13248-13257.

10. Bernasik, A., et al., *Electrical surface versus bulk properties of Fe-doped TiO_2 single crystals.* Solid State Ionics, 1994. **72**: p. 12-18.

11. Tang, H., et al., *Electrical and optical properties of TiO_2 anatase thin films.* Journal of applied physics, 1994. **75**(4): p. 2042-2047.

12. Jagadale, T.C., et al., *N-Doped TiO_2 Nanoparticle Based Visible Light Photocatalyst by Modified Peroxide Sol−Gel Method.* The Journal of Physical Chemistry C, 2008. **112**(37): p. 14595-14602.

13. Wang, M.C., H.J. Lin, and T.S. Yang, *Characteristics and optical properties of iron ion (Fe^{3+})-doped titanium oxide thin films prepared by a sol–gel spin coating.* Journal of Alloys and Compounds, 2009. **473**(1–2): p. 394-400.

14. Lin, H.-J., et al., *Optical and photocatalytic properties of Fe^{3+}-doped TiO_2 thin films prepared by a sol–gel spin coating.* Ceramics International, 2014. **40**(7, Part B): p. 10633-10640.

15. Chen, C.-C., S.-H. Hu, and Y.-P. Fu, *Effects of surface hydroxyl group density on the photocatalytic activity of Fe^{3+}-doped TiO_2.* Journal of Alloys and Compounds, 2015. **632**: p. 326-334.

16. Yan, J., et al., *Facile synthesis of an iron doped rutile TiO_2 photocatalyst for enhanced visible-light-driven water oxidation.* Journal of Materials Chemistry A, 2015.

17. Cronemeyer, D., *Infrared absorption of reduced rutile TiO_2 single crystals.* Physical Review, 1959. **113**(5): p. 1222.

18. Gupta, V.P. and N.M. Ravindra, *Optoelectronic properties of rutile (TiO_2).* Journal of Physics and Chemistry of Solids, 1980. **41**(6): p. 591-594.

19. Rahman, K.A., et al., *Toward sustainable energy: photocatalysis of Cr-doped TiO_2: 1. electronic structure.* Ionics, 2018. **24**(2): p. 309-325.

20. Nowotny, M.K., et al., *Defect chemistry of titanium dioxide. Application of defect engineering in processing of TiO_2-based photocatalysts.* The Journal of Physical Chemistry C, 2008. **112**(14): p. 5275-5300.

21. Wang, C.-C., K.-W. Wang, and T.-P. Perng, *Electron field emission from Fe-doped TiO_2 nanotubes.* Applied Physics Letters, 2010. **96**(14): p. 143102.

22. Umebayashi, T., et al., *Analysis of electronic structures of 3d transition metal-doped TiO_2 based on band calculations.* Journal of Physics and Chemistry of Solids, 2002. **63**(10): p. 1909-1920.

23. López, R. and R. Gómez, *Band-gap energy estimation from diffuse reflectance measurements on sol–gel and commercial TiO_2: a comparative study.* Journal of sol-gel science and technology, 2012. **61**(1): p. 1-7.

24. Bak, T., et al., *Effect of Crystal Imperfections on Reactivity and Photoreactivity of TiO_2 (Rutile) with Oxygen, Water, and Bacteria.* The Journal of Physical Chemistry C, 2011. **115**(32): p. 15711-15738.

25. George, S., et al., *Role of Fe Doping in Tuning the Band Gap of TiO_2 for the Photo-Oxidation-Induced Cytotoxicity Paradigm.* Journal of the American Chemical Society, 2011. **133**(29): p. 11270-11278.

26. Delekar, S.D., et al., *Structural refinement and photocatalytic activity of Fe-doped anatase TiO_2 nanoparticles.* Applied Surface Science, 2012. **263**: p. 536-545.

27. Zhu, J., et al., *Characterization of Fe–TiO_2 photocatalysts synthesized by hydrothermal method and their photocatalytic reactivity for photodegradation of XRG dye diluted in water.* Journal of Molecular Catalysis A: Chemical, 2004. **216**(1): p. 35-43.

28. Nahar, M.S., K. Hasegawa, and S. Kagaya, *Photocatalytic degradation of phenol by visible light-responsive iron-doped TiO_2 and spontaneous sedimentation of the TiO_2 particles.* Chemosphere, 2006. **65**(11): p. 1976-1982.

29. Wang, X., et al., *Wavelength-sensitive photocatalytic degradation of methyl orange in aqueous suspension over iron (III)-doped TiO_2 nanopowders under UV and visible light irradiation.* The Journal of Physical Chemistry B, 2006. **110**(13): p. 6804-6809.

30. Zhou, M., J. Yu, and B. Cheng, *Effects of Fe-doping on the photocatalytic activity of mesoporous TiO_2 powders prepared by an ultrasonic method.* Journal of Hazardous Materials, 2006. **137**(3): p. 1838-1847.

31. Teoh, W.Y., et al., *Flame sprayed visible light-active Fe-TiO_2 for photomineralisation of oxalic acid.* Catalysis Today, 2007. **120**(2): p. 203-213.

32. Garza-Arévalo, J.I., et al., *Fe doped TiO_2 photocatalyst for the removal of As(III) under visible radiation and its potential application on the treatment of As-contaminated groundwater.* Materials Research Bulletin, 2016. **73**: p. 145-152.

33. Molea, A., et al., *Correlation of Physicochemical Properties with the Catalytic Performance of Fe-Doped Titanium Dioxide Powders.* Industrial & Engineering Chemistry Research, 2015. **54**(30): p. 7346-7351.

34. Ma, J., H. He, and F. Liu, *Effect of Fe on the photocatalytic removal of NOx over visible light responsive Fe/TiO_2 catalysts.* Applied Catalysis B: Environmental, 2015. **179**: p. 21-28.

35. Tang, W., et al., *Preparation of an Fe-doped visible-light-response TiO_2 film electrode and its photoelectrocatalytic activity.* Materials Science and Engineering: B, 2014. **187**: p. 39-45.

36. Deng, F., et al., *The effect of vinyl-containing ionic liquid on the photocatalytic activity of iron-doped TiO_2.* Journal of Molecular Catalysis A: Chemical, 2013. **366**: p. 222-227.

37. Bickley, R.I., et al., *Characterisation of iron/titanium oxide photocatalysts. Part 2.—Surface studies.* Journal of the Chemical Society, Faraday Transactions, 1994. **90**(15): p. 2257-2264.

CHAPTER THREE

3 Literature overview

The available reports on the mechanism of iron incorporation into the TiO_2 lattice and photocatalytic activity of Fe-doped TiO_2 in partial water oxidation are full of conflicting results. The aim of this literature overview is to collect the reported data and identify unresolved problems. It is shown that the observed discrepancies in many instances are related to the effect of oxygen activity on mechanism of iron incorporation and the related electronic structure. The later effect has been ignored so far. The present chapter presents a brief overview on the properties of TiO_2, including solubility of iron in the TiO_2 lattice, electrical conductivity, electronic structure, effect of iron concentration on band gap, effect of segregation on surface vs. bulk composition, valence of iron ions, phase transition, and effect of iron on photocatalytic activity of TiO_2. This chapter also formulates the key questions for this PhD project.

3.1 Iron solubility limit in TiO_2

Solubility limit of solids in solids can be defined as maximum quantity of the substance (the solute) that can be dissolved in another substance (the solvent) and form solid solution at specific temperature and specific gas phase composition and pressure.

Solubility limit for metal oxides can be defined as maximum amount of solute oxide that is dissolved in the solvent oxide and form solid solution at specific temperature and the gas phase of specific oxygen activity.

Solubility limit of iron (solute) in TiO_2 (solvent) is the maximum amount of iron that can be dissolved in TiO_2 and form solid solution of Fe-doped TiO_2 at specific temperature and gas phase of specific oxygen activity.

The properties of solid solutions are well-defined within the solubility limit when the studied specimen is homogeneous in terms of its structure and chemical composition. Incorporation of the amount of solute beyond the solubility limit results in the formation of a heterogeneous system, which is more awkward for characterization. The reported data on the effect of temperature on the solubility of iron in TiO_2 is represented in **Figure 3-1.**

As seen, the solubility limit of iron in TiO_2 strongly depends on the annealing condition, such as temperature and time. According to Li et al., [1] and Wittke et al., [2], the iron solubility limit in TiO_2 is around 1 at% when specimen is annealed at 1073 K, and increases with annealing temperature, assuming the level of 3 at% Fe at 1673 K [2]. As seen from the data of Li et al., [1] and Wittke et al.,[2], the effect of oxygen activity on the solubility limit is negligible. So far, the effect of oxygen activity on iron solubility limit has not been reported.

According to Busiakiewicz et al., [3], the iron solubility limit in TiO_2 single crystal is substantially below the level established for polycrystalline specimens of TiO_2. As seen, the iron solubility limit according to Pownchevy et al., [6] (0.8 at% at 1473 k), is markedly below the solubility limit. The observed discrepancy, which seems

related to the short time of annealing conditions (1 h), indicates that the solubility of iron in TiO_2 achieves the solubility limit after prolonged period of time.

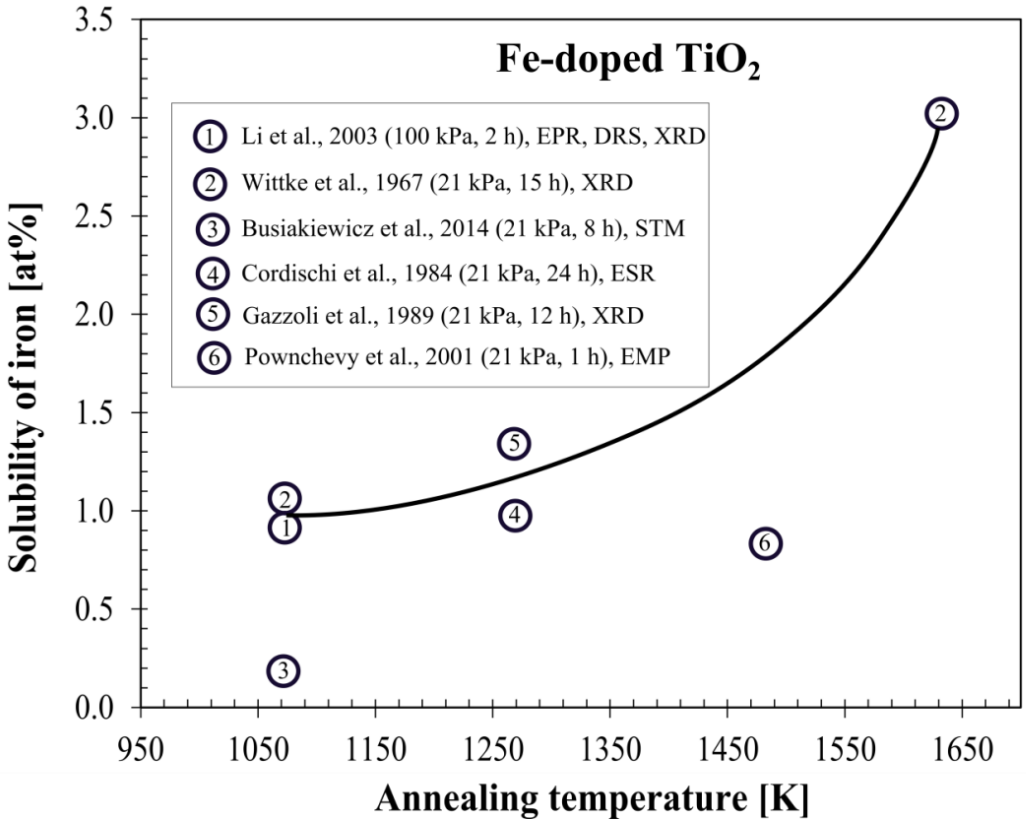

Figure 3-1: Solubility limit of iron in TiO_2 as a function of annealing temperature for polycrystalline specimens annealed in air [2-6] except the data of Li et al.,[1]. The applied approaches include: EPR (electron paramagnetic resonance), DRS (differential reflectance spectroscopy), XRD (x-ray diffraction), STM (scanning tunnelling microscope), ESR (electron spin resonance) and EMP (electron microprobe).

3.2 Electrical conductivity

Figure 3-2 represents the reported effect of oxygen activity on electrical conductivity of undoped and Fe-doped TiO_2. As seen in **Figure 3-2**, iron incorporated in the TiO_2 lattice results in a shift of the minimum of the electrical conductivity (corresponding

approximately n-p transition) to lower oxygen activity [7]. The results in **Figure 3-2** show that TiO_2 can be converted into p-type TiO_2 by annealing the specimen in high oxygen activity and incorporation of acceptor type ions, such as iron. This effect can be applied to impose the desired properties which correspond to enhanced performance of TiO_2 in solar-to-chemical energy conversion.

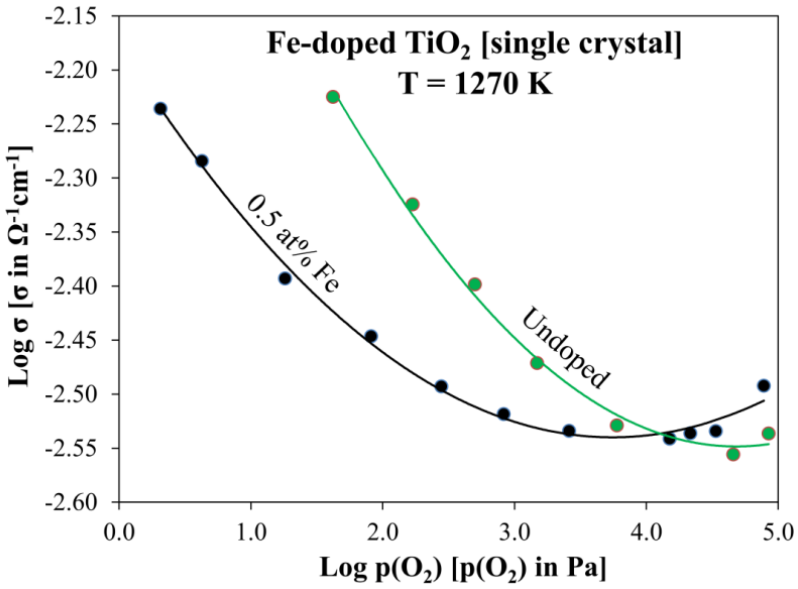

Figure 3-2: The effect of oxygen activity on electrical conductivity of undoped and Fe-doped TiO_2 [7].

3.3 Effect of iron on the band gap of TiO_2

The effect of iron on the band gap of TiO_2 is represented in **Figure 3-3,** showing the dependence on iron concentrations for specimens of different morphologies, including thin films [8-12], nanotubes [13-15], and nanoparticles [16-22].

Thin Films. As seen, the reported data of Sobczyk et al., 2015 [11], and Tang et al., 2014 [12] indicate that iron doping up to 2 at% results in a decrease of the band gap of thin films. The remaining authors [8-10] reported an insignificant effect even at the concentration of iron up to 20 at%. The latter data suggest that iron is not effectively incorporated into TiO_2 lattice.

Nanotubes. The reported data of all cited authors [13-15] indicate that increased iron concentration leads to a reduction of the band gap within the whole studied range. The observed change of the band gap was from approximately 3.2 eV for pure TiO_2 to about 2.8 eV for Fe-doped TiO_2 at 7 at% of iron.

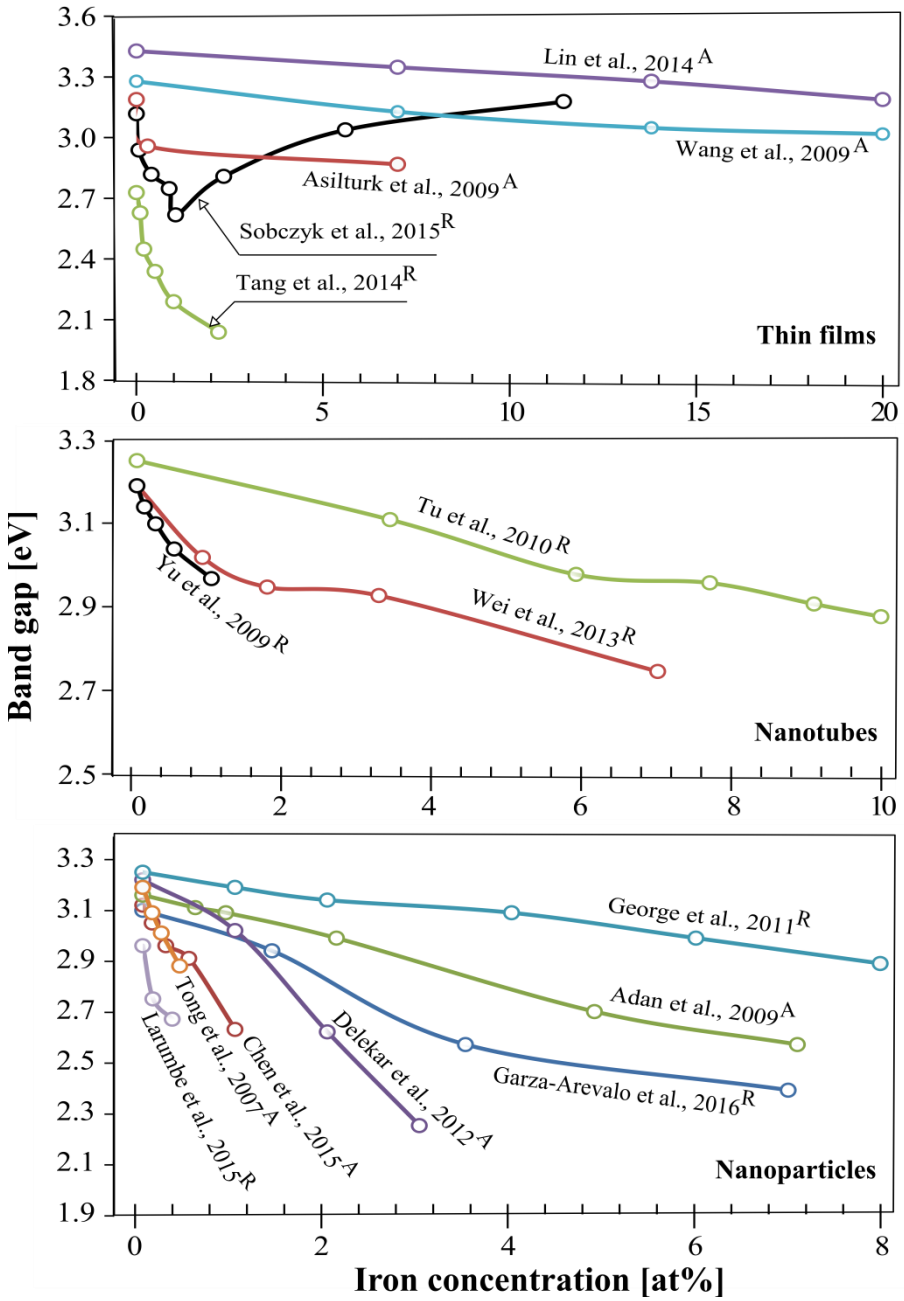

Figure 3-3: The reported band gap of TiO_2 as a function of iron concentration for samples of different morphologies, such as thin films [8-12], nanotubes [13-15], and nanoparticles [16-22]. Subscripts A and R represents the anatase and the mixture of anatase and rutile, respectively.

***Nanoparticles*.** The scatter of reported data in this case is substantial. The most substantial effect reported by Delekar et al., 2012 [19], indicates that introduction of iron at the level of 3 at% results in a reduction of the band gap from 3.2 eV for pure TiO_2 to 2.3 eV for Fe-doped TiO_2. The effects reported by the remaining authors [16-18, 20-22] essentially confirm that iron incorporation decreases the band gap. However, the related data differ in their absolute values. This scatter is likely to be related to different assumed electronic transition mechanisms and the differences in particle sizes, which were not reported. However, it is known that the band gap decreases with the increase of particle size, and particle size increases with the annealing temperature [23].

3.4 Surface vs. bulk composition of iron in Fe-doped TiO_2

The surface composition of a solid is entirely different from that of the bulk phase as a result of segregation [24]. The difference between the surface and bulk composition is influenced by both kinetic and the thermodynamic factors. The kinetic factor, which is related to the diffusion kinetics of segregating species, depends on the annealing temperature. However, the annealing temperature should be high enough to impose gas/solid equilibrium that is required to convert anatase to rutile as well as to reach segregation equilibrium; the segregation-induced surface concentration is determined by the thermodynamic factor. For a two component system, the surface vs. bulk composition of the solute and the solvent may be expressed as:

$$\frac{X_2^s}{X_1^s} = \frac{X_2^b}{X_1^b} \exp\left(\frac{-\Delta H_{seg}}{k_B T}\right) \qquad (3\text{-}1)$$

Where X_1^s and X_1^b denote the surface and bulk molar fraction of the solute at the surface and in the bulk, respectively, X_2^s and X_2^b represent the surface and bulk

molar fraction of the solvent, ΔH_{seg} is the enthalpy of segregation, k_B is the Boltzmann constant and T is the absolute temperature. Hirschwald et al. 1989 [25] have shown that the enthalpy of segregation for Cr-doped NiO within the solubility range is independent of the chromium concentration.

Knowledge of the effect of segregation on surface composition is essential in the interpretation of the mechanism of catalytic and photocatalytic reactions, which are determined by surface rather than bulk composition. The effect of segregation on surface properties of oxide materials has been reported for solid solutions, such as Cr-doped NiO [25] and Cr-doped CoO [25].

The segregation of specific species in oxide-based semiconductors, such as TiO_2, is more complex than that in metals and alloys. The segregation of species in oxide semiconductors are substantially influenced by the oxygen activity [24].
The main driving forces of the segregation in metal oxides, such as TiO_2, can be summarized as follows:

(a) The electrostatic potential difference between the surface and bulk defects.
(b) The strain energy induced by the lattice mismatch.

The reported data on iron segregation in Fe-doped TiO_2 is presented in **Table 3-1**, including the effect of annealing conditions, such as temperature and oxygen activity, surface and bulk concentrations of iron, and the related enrichment factor of iron [15, 24, 26-34].

Table 3-1: The reported data on iron segregation in Fe-doped TiO_2 [15, 24, 26-34].

#	References	Processing method	Annealing conditions			Fe concentration [at%]		Enrichment factor
			T [K]	p(O_2) [kPa]	t [h]	Surface	Bulk	
1	Bickley et al., 1994[26]	Precipitation	1273	21	24	5.1 5.2 6.2 8.2	0.5[a] 1.0[a] 2.0[a] 5.0[a]	f_{XPS} = 10.2 f_{XPS} = 5.20 f_{XPS} = 3.10 f_{XPS} = 1.65
2	Bernasik et al., 1994[24]	Verneuille	1400	100	20	---	0.5[a]	f_{SIMS} = 38
				0.02		---	0.5[a]	f_{SIMS} = 2.5
3	Pecchi et al., 2002[27]	Sol-gel	873	21	4	10.1	7.5[a]	f_{XPS} = 1.34
4	Ambrus et al. 2008[28]	Precipitation	1273	21	1	8.4 18.8	1.29[b] 10.4[b]	f_{XPS} = 6.51 f_{XPS} = 1.80
5	Cristina Adan et al., 2009[29]	Sol-gel	723	21	2	0.095 4.2	1.0[c] 5.0[c]	f_{XPS} = 0.95 f_{XPS} = 0.84
		Precipitation	873			2.2 4.2 8.0	1.0[c] 2.0[c] 5.2[c]	f_{XPS} = 2.2 f_{XPS} = 2.1 f_{XPS} = 1.5
6	Yu et al., 2009[15]	Thermal	773	21	1.5	1.82	0.5[a]	f_{XPS} = 3.64
7	Deng et al., 2009[30]	Sol-gel	773	21	3	3.3	0.4[d]	f_{XPS} = 8.25
8	Li et al., 2009[31]	Thermal	733	21	3	0.5 1.4 2.5 2.9	0.1[a] 0.5[a] 1.0[a] 2.0[a]	f_{XPS} = 5.0 f_{XPS} = 2.8 f_{XPS} = 2.5 f_{XPS} = 1.45
9	Bajnóczi et al., 2011[32]	Sol-gel	1273	21	1	8.4	0.89[e]	f_{XPS} = 9.43
		Thermal				9.5 8.7	0.78[e] 0.80[e]	f_{XPS} = 12.17 f_{XPS} = 10.87
10	Mangham et al., 2011[33]	Precipitation	1273	21	8	2.4	2[a]	f_{XPS} = 1.2
11	Liu et al., 2013[34]	Thermal	673	21	2	3.4	0.35[a]	f_{XPS} = 9.71

a = Nominal; b = Energy dispersive X-ray spectroscopy (EDX); c = Inductively coupled plasma-optical emission spectrometry (ICP-OES); d = Inductively coupled plasma (ICP); e = Atomic absorption spectrometry; SIMS = Secondary ion mass spectrometry; XPS = X-ray photoelectron spectroscopy

The data in **Table 3-1** related to annealing in air is represented graphically in **Figure 3-4** [26, 28, 29, 31].

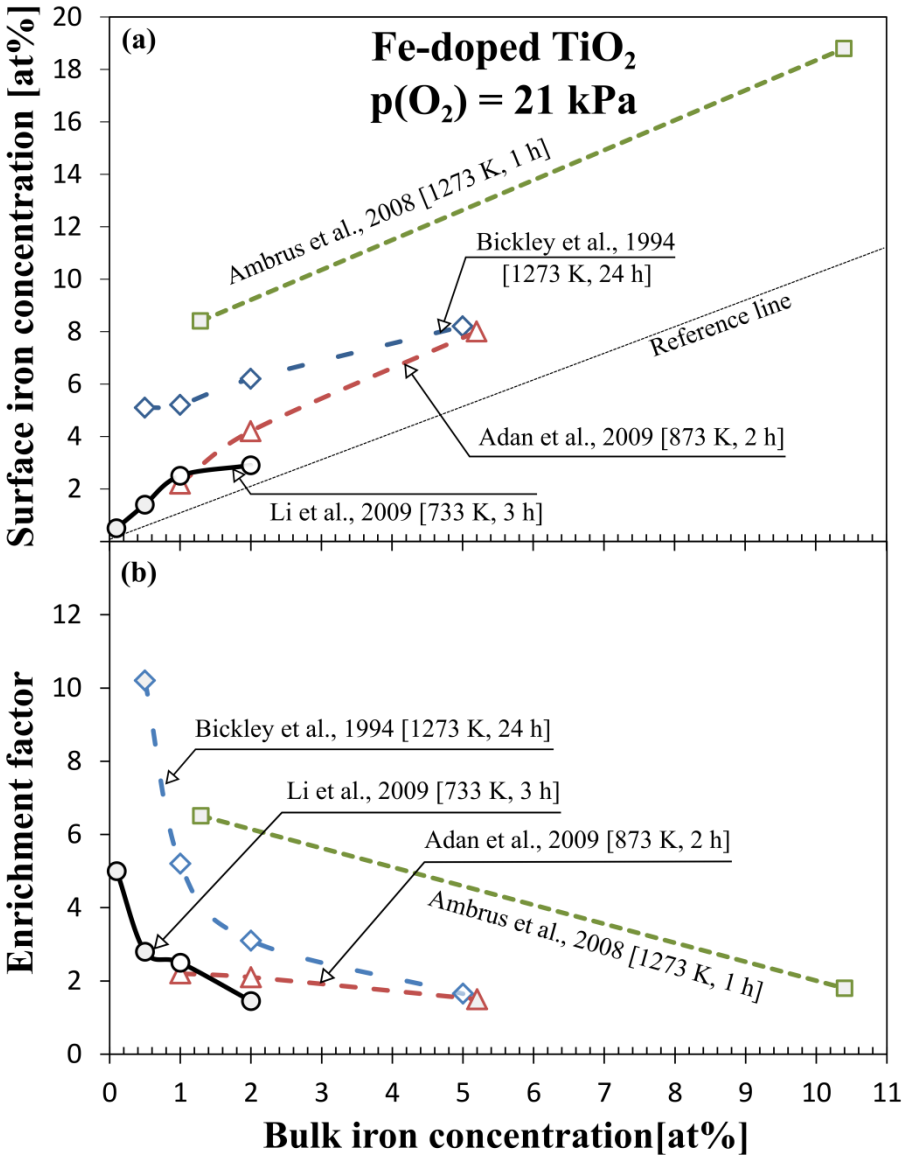

Figure 3-4: The reported segregation data for Fe-doped TiO_2 after annealing in air, including segregation-induced surface vs. bulk concentration of iron (a), and the related enrichment factor of iron (b).

As seen, there is a clear tendency for the iron enrichment factor to increase with the decrease of bulk iron concentration. However, the reported results exhibit a substantial scatter in both absolute concentration data and the related enrichment values. The observed discrepancies are related to different processing conditions, including the temperature, and the time of annealing as well as the gas phase composition. While in most cases the specimens were annealed in air, different

humidity level in the surrounding environment seems to have had an effect on the concentration of protons incorporated during the annealing. Therefore, in present work a care will be taken to minimize the related effects by using the following processing conditions:

- The temperature of annealing will be high enough to allow segregation to reach equilibrium.
- The time of annealing will be long enough to reach segregation equilibrium.
- The gas phase composition will be well-defined. Although annealing in air assures the desired oxygen activity of $p(O_2)$ = 21 kPa, elimination of humidity factor requires the use of dry air or an artificial air composed of dry gases.

In considering the effect of segregation, it is important to know the location of the solute incorporated into TiO_2 lattice. The size and charge of solute ions have an impact on segregation in general, and iron in particular, as described later (**section 5.2.3**). The reported positions of iron incorporated into TiO_2 lattice and incorporation mechanisms are shown in **Table 3-2**.

According to **Table 3-2**, three different iron species have been indentified for Fe-doped TiO_2:

- Tri-valent iron incorporated into titanium sites leading to the formation of effectively singly ionised acceptor-type defects.
- Di-valent iron incorporated into cation sublattice leading to the formation of doubly ionised acceptor-type defects.
- Tri-valent iron incorporated into interstitial sites and acting as donor-type defects.

Table 3-2: The reported data on iron incorporation mechanism into TiO_2.

Authors	**Approach**	**Outcomes**	**Plausible incorporation sites**
Andersson et al., 1974 [35]	EPR	Iron incorporates into TiO_2 through substitutional mechanism.	Fe'_{Ti}
Radecka et al., 1994 [7]	Electrical conductivity	The electrical conductivity of Fe-doped TiO_2 is greater than that for pure TiO_2 in oxidising condition owing to the increased hole concentrations, which indicates that iron acts as an acceptor-type dopant.	
Bally et al., 1998 [36]			
Bernasik et al., 1994 [24]	SIMS	Iron segregation in Fe-doped TiO_2 is significant in oxidising condition (100 kPa).	
Sasaki et al., 1983 [37]	Diffusion	While diffusing interstitially into TiO_2 iron exhibits transient valency of +3.	$Fe_i^{\bullet\bullet\bullet}$
Janes et al., 2004 [38]	ESR	Iron preferentially enters into TiO_2 through interstitial mechanism.	
Fan et al., 2009 [39]	Mossbauer	Iron exists as Fe^{2+} and Fe^{3+} in Fe-doped TiO_2 when the specimens were annealed in lower and higher oxygen activity, respectively.	Fe''_{Ti}, Fe'_{Ti}
SIMS = Secondary ion mass spectrometry, EPR = Electron paramagnetic resonance, ESR = Electron spin resonance			

Since the mechanism of iron incorporation is profoundly influenced by the experimental conditions, the specimens need to be prepared through well-defined experimental procedure assuring reproducible properties. The key approaches included:

- Formation of Fe-doped TiO_2 by sol-gel technique following the individual steps in reproducible manner.
- Selection of the processing parameters leading to the incorporation of iron into TiO_2 lattice and the formation of solid solution.
- Analysis of the bulk chemical concentrations, including iron and the major impurities.
- Inducement of iron segregation in Fe-doped TiO_2 by annealing in the gas phase of controlled oxygen activity.

3.5 Effect of experimental conditions on the valence of iron ions in TiO_2

The effect of the applied experimental procedures and the associated high-temperature processing conditions, such as temperature and oxygen activity on the valence of iron ions in TiO_2 is shown in **Table 3-3**. The XPS data of Zhou et al., 2005 [40] and Wang et al., 2012 [41] indicate that iron ions incorporated into the surface layer of TiO_2 during annealing in air have both 2+ and 3+ states. Assuming that in both cases iron enters preferentially into titanium sites, the relative electrical charge of iron, compared to the lattice, is -2 and -1, respectively. In both cases iron ions form acceptor levels leading to a decrease of the Fermi level. The ESR data of Janes et al., 2004 [38] show that iron is incorporated into the bulk phase of TiO_2 preferentially into interstitial sites leading to the formation of donors and an increase of the Fermi level.

Table 3-3: The reported data on the valence of iron ions in Fe-doped TiO_2.

Authors	**Approach**	**Fe concentration [at%]**		**p(O_2), T (K)**	**Outcomes**	**Reasonable conclusions**
		Surface	**Bulk**			
Bickley et al., 1994 [26]	XPS	5.1 8.2	0.5 5	21 kPa, 1273	$(Fe^{3+})_s$	Secondary phase or iron oxide cluster forms at surface for higher iron concentration owing to exceeding solubility limit of iron in TiO_2.
Pecchi et al., 2002 [27]		10.1	7.5	21 kPa, 873	$(Fe^{3+})_s$	
Zhou et al., 2005 [40]		---	2.5	21 kPa, 773	35% $(Fe^{3+})_s$ 65% $(Fe^{2+})_s$	Absence of iron segregation is likely to the insufficient annealing temperature.
Ambrus et al., 2008 [28]		8.4 18.8	1.29 10.4	21 kPa, 1273	$(Fe^{3+})_s$	The increase of iron concentration decreases the segregation-induced iron enrichment factor (surface/bulk) at the surface.
Adan et al., 2009 [29]		2.2 4.2	1.0 2.0	21 kPa, 873	$(Fe^{3+})_s$	---
Deng et al., 2009 [30]		3.3	0.4	21 kPa, 773	$(Fe^{3+})_s$	Fe^{3+} ions may exist at the grain boundaries owing to the insufficient annealing temperature.

Li et al., 2009 [31]		1.4	0.5	21 kPa, 733	$(Fe^{3+})_s$	Fe^{3+} forms Fe'_{Ti}.
Yu et al., 2009 [15]		1.82	0.5	21 kPa, 773	$(Fe^{3+})_s$	
Bajnóczi et al., 2011[32]		8.4	0.89	21 kPa, 1273	$(Fe^{3+})_s$	---
Mangham et al., 2011 [33]		2.4	2	21 kPa, 1273	$(Fe^{3+})_s$	Iron oxide clusters present at the surface.
Wang et al., 2012 [41]		---	1	21 kPa, 773	91.19% $(Fe^{3+})_s$ 8.81% $(Fe^{2+})_s$	The annealing temperature was not high enough to reach equilibrium.
Liu et al., 2013 [34]		---	0.35	21 kPa, 763	$(Fe^{3+})_s$	Iron oxide cluster present at the surface.
Khan et al. 2016 [42]		5	0.5	21 kPa, 773	$(Fe^{3+})s >$ $(Fe^{2+})_s >$ $(Fe^{4+})_s$	Fe^{3+} is the predominant oxidation state at the surface, and Fe^{3+} forms Fe'_{Ti}.
Bernasik et al., 1994 [24]	SIMS	39	0.5	2 Pa, 1673 100 kPa, 1673	$(Fe^{3+})_b$	Iron segregates more in oxidising condition than in reducing condition and iron acts as acceptor- type dopant.
Janes et al. 2004 [38]	ESR	---	0.13	21 kPa, 1073	$(Fe^{3+})_b$	Iron preferentially incorporates into TiO_2 through interstitial mechanism.
Dang et al., 2010 [43]	Raman Spectra	---	0.5-2	21 kPa, 873	$(Fe^{3+})_b$	Incorporation of iron results in formation of oxygen vacancies.
Chang et al. 2014 [44]	EPR	---	0.2	21 kPa, 773	$(Fe^{3+})_b$	The increase of oxygen activity increases the concentration of Fe'_{Ti}.
XPS – X-ray photoelectron spectroscopy, SIMS – Secondary ion mass spectrometry, ESR – Electron spin resonance, EPR- Electron paramagnetic resonance, subscripts s and b represents the surface and bulk, respectively.						

3.6 Phase transformation from anatase to rutile

Titanium dioxide exists as different polymorphs of which the most common are anatase, rutile, and brookite. However, only anatase (metastable) and rutile (stable) are being studied extensively owing to their prevalent availability. The irreversible anatase to rutile phase transformation is affected by several parameters which are discussed in the following sub sections:

3.6.1 Effect of annealing temperature and iron concentration

The kinetics of phase transformation strongly depends on the annealing temperature and impurity concentration in TiO_2 [45-47]. It has been reported that the incorporation of iron into TiO_2 lattice results in an enhanced concentration of oxygen vacancies which promote the phase transformation, as shown in **Figure 3-5**.

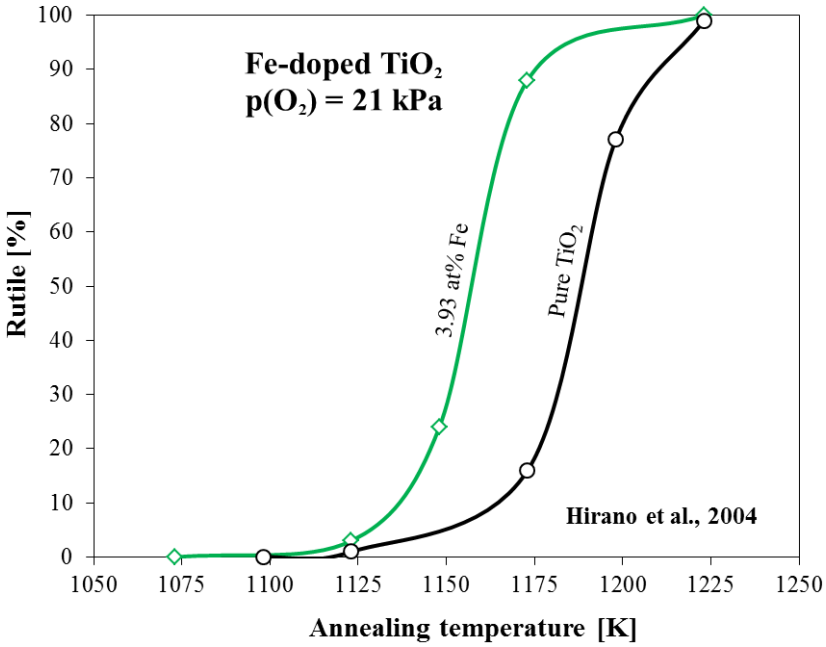

Figure 3-5: The effect of annealing temperature and iron doping on phase transformation from anatase to rutile for the specimens annealed in oxidising condition for 1 hour [45].

3.6.2 Effect of oxygen activity on phase transition

The oxygen activity has also a significant impact on phase transformation, as shown in **Figure 3-6**. When the anatase specimen is treated in different atmospheres, such as hydrogen, vacuum, air, argon, and pure oxygen, for the same time it displays a different rutile fractions [48]. The rutile fraction decreases with the increase of oxygen activity. Gennari et al., 1998 [47] proposed that the formation of more

oxygen vacancies in reducing conditions (argon) than in oxidising conditions (air) accelerate the phase transformation.

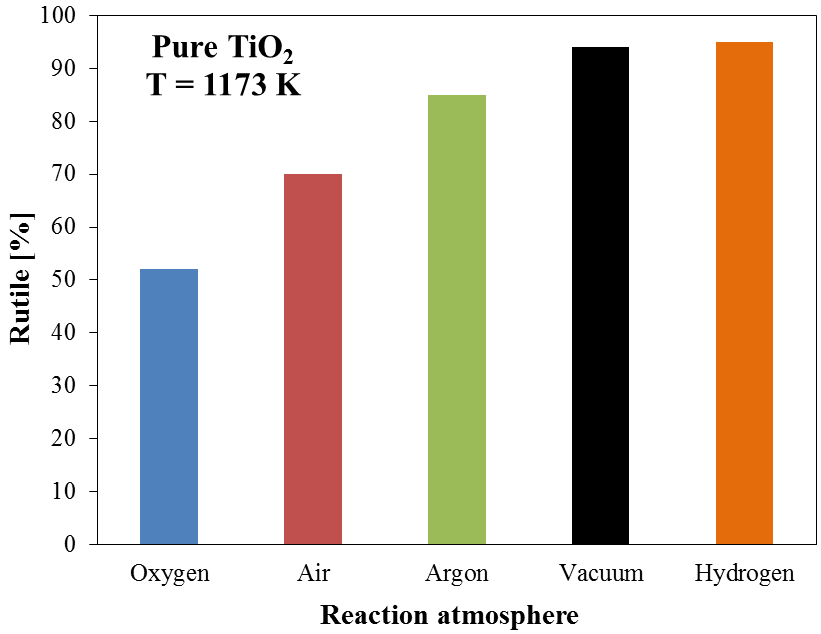

Figure 3-6: The effect of annealing atmosphere on phase transformation from anatase to rutile [48].

3.7 Effect of iron concentration on photocatalytic activity of TiO_2

Figure 3-7 and **Figure 3-8** show the effect of iron concentration on photocatalytic activity of TiO_2. These results cannot be compared directly because the respective kinetic constants were determined for the photo-oxidation reactions of different testing compounds. **Table 3-4** summarises the determined properties with the main derived conclusions.

Table 3-4: Summary of the reported data on the effect of iron concentration on photocatalytic activity of TiO_2.

Authors	Approaches	Testing compound	Determined properties	Reasonable conclusions
Zhang et al., 2003 [49]	XRD, XPS, UV-Vis spectroscopy	Methyl orange	• Iron incorporation leads to a decrease of the band gap. • Photocatalytic activity increases up to 0.58 at% Fe.	Fe^{3+} forms Fe'_{Ti}.
Nahar et al., 2006 [50]	XRD, XPS, UV-Vis spectroscopy	Phenol	• Iron incorporation results in an enhanced photocatalytic activity up to 0.5 at% Fe.	Trivalent iron forms anodic sites (Fe'_{Ti}) up to 0.5 at% Fe.
Zhou et al., 2006 [51]	DTA, XRD, XPS, UV-Vis spectroscopy	Acetone	• Iron doping results in a reduction of the band gap of TiO_2. • XPS study shows the existence of Fe^{3+} and Fe^{2+} at the surface of Fe-doped TiO_2. • Increase of the photocatalytic activity up to 0.25 at% Fe.	• Photocatalytic activity is not related to the light absorption. • Fe^{3+} and Fe^{2+} incorporate as Fe'_{Ti} and Fe''_{Ti}, respectively.
Liu et al., 2009 [52]	XRD, TEM, XPS, UV-Vis spectroscopy	Methyl orange	Fe leads to • a reduction of the band gap. • an increase of the photocatalytic activity up to 0.05 at% Fe.	Photocatalytic activity is not related to the band gap.
Deng et al., 2009 [30]	XRD, TEM, XPS	Methyl orange	• Iron leads to increase of the photocatalytic activity up to 0.8 at% Fe. • XPS study reveals the presence of both Fe^{3+} and Fe^{2+} at the surface of Fe-doped TiO_2.	Fe^{3+} and Fe^{2+} incorporate as Fe'_{Ti} and Fe''_{Ti}, respectively.
Mathews et al., 2009 [53]	XRD, XPS, UV-Vis spectroscopy	Methylene blue	Iron results in enhancement of the light absorption and photocatalytic activity.	Fe^{3+} maybe incorporated as Fe'_{Ti} leading to the formation of oxygen vacancies.
Fàbrega et al., 2010 [54]	XRD, ICP, ESR, UV-Vis spectroscopy	Methylene blue	Band gap decreases with iron doping.	Iron doping into TiO_2 results in a decreased photocatalytic activity owing to the formation of defect complexes.
Naeem et al., 2010 [55]	XRD, EDX, SEM, UV-Vis spectroscopy	Phenol	• Iron doping leads to a reduction of the band gap. • Photocatalytic activity increases up to 0.5 at% Fe.	Fe^{3+} forms Fe'_{Ti}.
Tu et al., 2010 [13]	XRD, TEM, EDS, UV-Vis spectroscopy	Methylene blue	• Iron doping leads to a reduction of the band gap and increase of the photocatalytic activity up to 5.9 at% Fe.	The photocatalytic activity is not related to the light absorption.

Wan et al., 2011 [56]	XRD, XPS, UV-Vis spectroscopy	Methylene blue	• Band gap decreases with the iron concentration. • Iron doping results in the formation of intermediate state within the band gap of TiO_2. • XPS shows the existence of both Fe^{3+} and Fe^{2+} at the surface. • Increase of photocatalytic activity up to 1.5 at% Fe.	• Fe^{3+} and Fe^{2+} incorporate as Fe'_{Ti} and Fe''_{Ti}, respectively. • Photocatalytic activity is not significant at higher iron concentration (beyond 1.5 at%) due to the formation of defect clusters.
Delekar et al., 2012 [19]	XRD, TGA, TEM, FTIR, UV-Vis spectroscopy	p-nitrobenzyl	Iron leads to • a decrease of the band gap. • an increase of the photocatalytic activity with the iron concentration.	• The photocatalytic activity is directly related to the band gap. • Fe^{3+} incorporates as Fe'_{Ti}, leading to the formation of oxygen vacancies.
Pang et al., 2012 [57]	TEM, XRD, XPS, UV-Vis spectroscopy	Rhodamine B	• Iron doping results in a reduction of the band gap. • Photocatalytic activity increases due to high surface area.	• Fe^{3+} incorporates as Fe'_{Ti} leading to formation of oxygen vacancies.
Wei et al., 2013 [14]	XRD, TEM, XPS, UV-Vis spectroscopy	Red X-3B	• Band gap and surface area decreases with the iron concentration. • XPS studies show the Fe^{3+} oxidation state at the surface of Fe-doped TiO_2.	• There is no direct relationship between band gap, surface area and photocatalytic performance. • Fe^{3+} forms Fe'_{Ti}.
Crișan et al. 2014 [58]	XRD, XPS	Nitroben zene	Fe doping results in an • increase of surface iron species (Fe^{3+}), determined by XPS analysis. • increase of the photocatalytic activity up to 0.7 at% Fe.	• Fe^{3+} incorporates as Fe'_{Ti} leading to the formation of oxygen vacancies. • Fe_2O_3 clusters forms at higher iron concentration.
Tang et al., 2014 [12]	XRD, Raman spectra, UV-Vis spectroscopy	Rhodamine B	• Iron leads to the enhancement of the light absorption. • The enhancement of light absorption increases the photocatalytic activity.	Fe^{3+} may be incorporated as Fe'_{Ti}.
Chen et al., 2015 [20]	XRD, TGA, ESR, XPS, FTIR, UV-Vis spectroscopy	Methylene blue	The incorporation of iron into TiO_2 results in: • reduction of the band gap. • increase of the photocatalytic activity up to 0.1 at% Fe. • decrease of the photocatalytic performance owing to the formation of cluster beyond 0.1 at% Fe.	• Photocatalytic activity is not related to the band gap. • Fe^{3+} forms Fe'_{Ti}. • Fe participates the following reactions: $Fe^{3+} \rightarrow Fe^{4+} + e^-$ $e^- + O_2 \rightarrow O_2^-$ $Fe^{4+} + OH^- \rightarrow OH^* + Fe^{3+}$

Bansode et al., 2015 [59]	XRD, SEM, EDX, UV-Vis spectroscopy	Methylene blue	Iron results in • a reduction of the band gap. • an increase of the photocatalytic activity up to 2 at% Fe.	Formation of defect complexes (beyond 2 at% Fe) results in a decrease of the photocatalytic activity.
XRD = X-ray diffraction , XPS = X-ray photoelectron spectroscopy, TEM = Transmission electron microscopy, DTA =Differential thermal analysis , ICP = Inductively coupled plasma , SEM = Scanning electron microscopy, EDX = Energy dispersive X-ray, ESR = Electron spin resonance, UV = Ultraviolet-Visible				

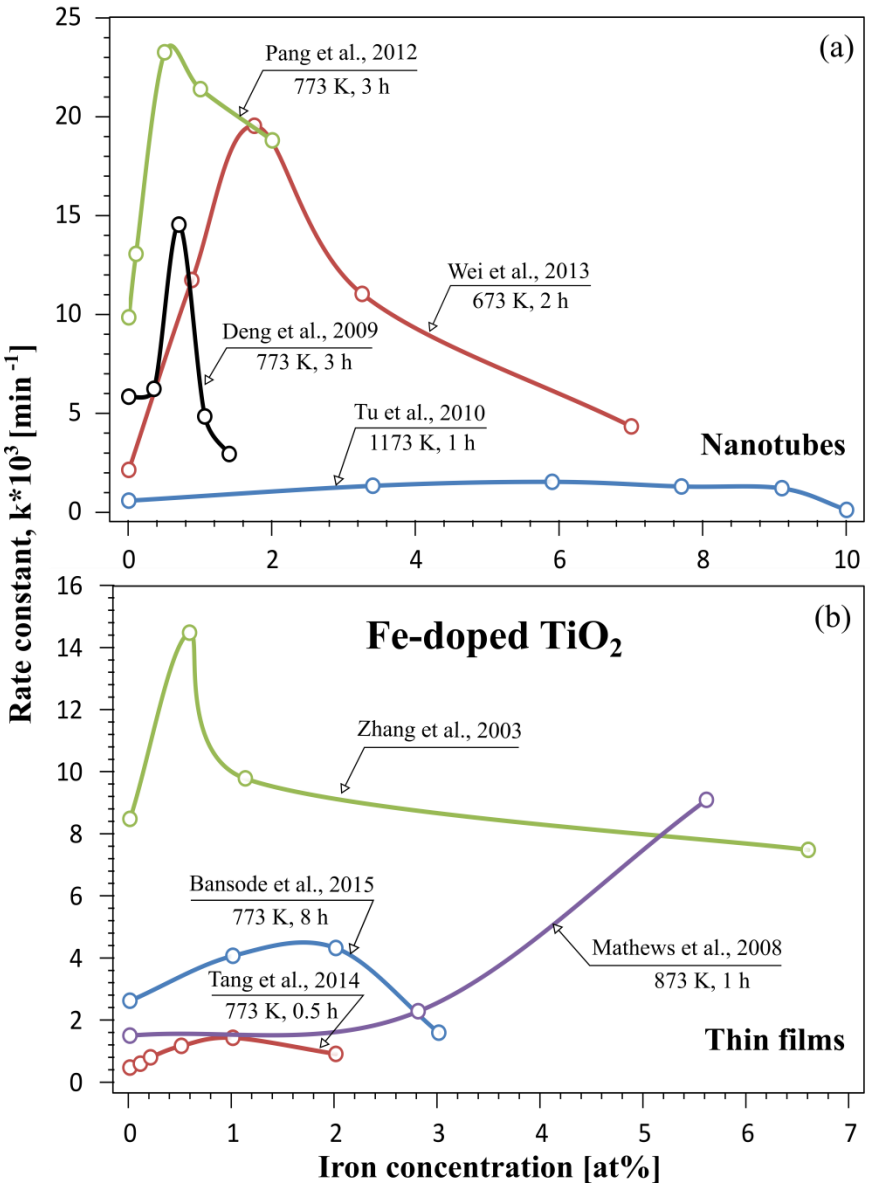

Figure 3-7: The reported data on the photocatalytic activity of TiO_2 as a function of bulk iron concentration for samples of different morphologies, such as nanotubes (a), and thin films (b).

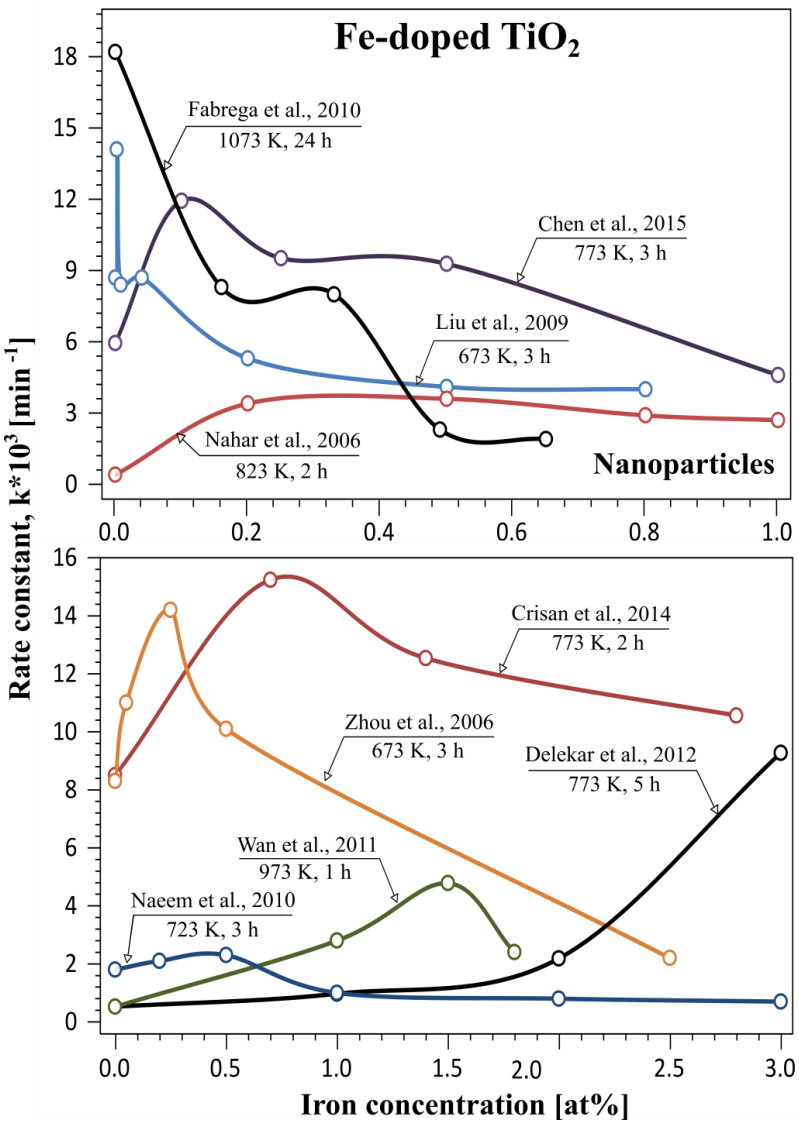

Figure 3-8: The reported data on the photocatalytic performance of TiO_2 as a function of bulk iron concentration. Both top and bottom figures are based on same morphology (nanoparticle). However, the scale of iron concentration is different.

3.8 Effect of grain size on the band gap of pure and Fe-doped TiO_2

This section considers the effect of grain size of polycrystalline TiO_2 on the band gap. The related experimental data are collected in **Table 3-5 a** and **Table 3-5 b** for TiO_2 and Fe-doped TiO_2, respectively. The effect for undoped TiO_2 is represented graphically in **Figure 3-9.**

Table 3-5 a: The reported data on the band gap of TiO_2, including single crystal and polycrystalline specimens.

References	Phase	Transition	Approach	Band gap, E_g [eV]	Grain size [nm]
				Single crystal TiO_2	
Cronomeyer et al., 1959 [60]	Rutile	---	Electrical conductivity	3.05	---
Gupta and Ravindra, 1980 [61]			Optical	3.03	
Nowotny et al., 2006 [62]			Electrical conductivity	3.1	---
Average value				3.06 eV	
				Polycrystalline TiO_2	
Fox et al., 2010 [63]	Rutile	Direct	Theoretical	2.46	---
Zhang et al., 2014 [64]	Rutile Anatase	Direct Indirect		1.86 2.13	--- ---
Tang et al., 1994 [65]	Anatase	Indirect	UV-Vis absorbance	3.20	30
Jagadale et al., 2008 [66]		---	UV-Vis reflectance	3.44	30
Fabrega et al., 2010 [54]			UV-Vis absorbance	3.2	22.8
Carneiro et al., 2014 [67]		Indirect		3.14	14.94
Khan et al., 2016 [42]		---	UV-Vis reflectance	3.17	---
Sood et al., 2015 [68]	Mixed	---	UV-Vis absorbance	3.2	25
Yan et al., 2015 [69]	Rutile	Indirect		2.9	10

As seen in in **Figure 3-9**, the linear dependence represents the effect of grain size on the band gap for TiO_2 (anatase). The data reported by Tang et al., requires verification owing to the substantial deviation from the band gap value for anatase.

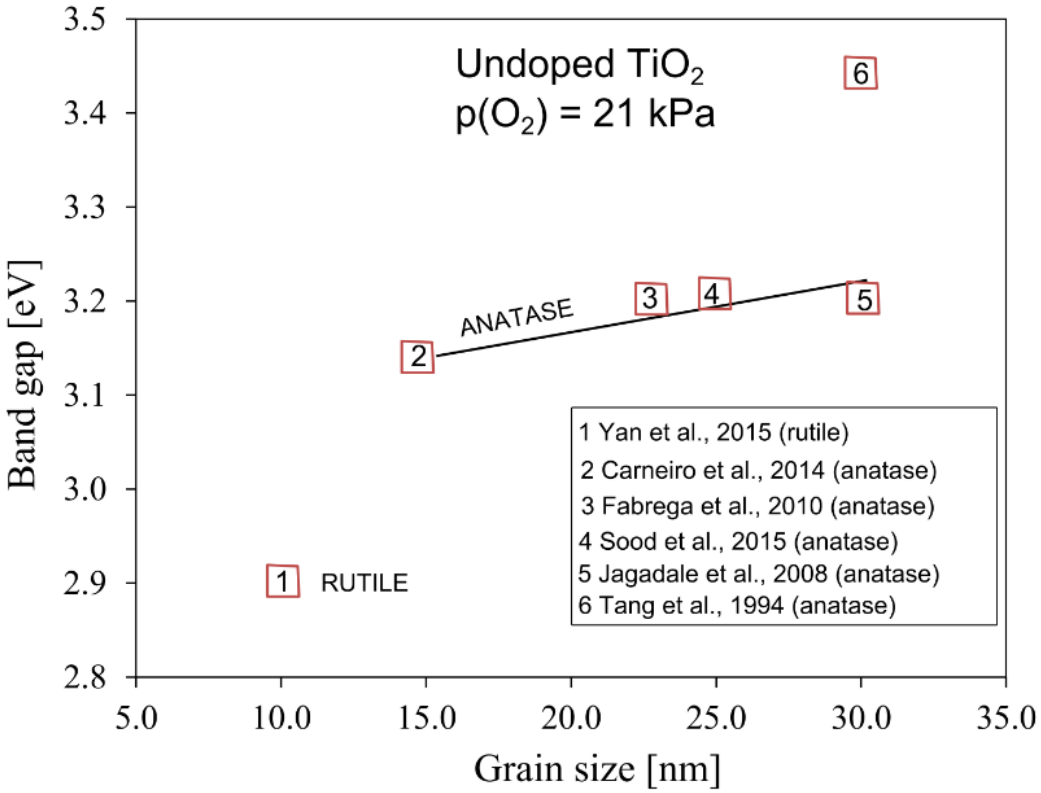

Figure 3-9: The effect of grain size on band gap for undoped TiO_2 (anatase) in air [1, 2, 3, 4, 5 and 6 indicates reference 69, 67, 54, 68, 66, and 65, respectively].

The reported experimental data on the band gap for Fe-doped TiO_2 (**Table 3-5 b**) is not appropriate for the determination of the effect of grain size on the band gap since the data correspond to different iron content. Therefore, the reported data are affected by two variables.

Table 3-5 b: The reported data on the band gap of Fe-doped TiO_2.

References	Phase	Transition	Approach	Band gap, E_g [eV]			
				Pure TiO_2		Fe-doped TiO_2	
				Eg [eV]	Size [nm]	Eg [eV], (at%)	Size [nm]
Wang et al., 2009 [9]	Anatase	Indirect	UV-Vis transmittance	3.29	11.1	3.03 (20)	8.8
Yu et al., 2009 [15]	Mixed	Direct	UV-Vis reflectance	3.19	14.9	2.97 (1)	11.4
Tu et al., 2010 [13]		---	UV-Vis absorbance	3.25	---	2.88 (10)	---
George et al., 2011 [16]		Indirect		3.26	6~12	2.9 (8)	---
Lin et al., 2014 [70]	Anatase		UV-Vis transmittance	3.44	9.8	3.2 (20)	6.28
Tang et al., 2014 [12]	Mixed	---	UV-Vis reflectance	2.74	22.6	2.05 (2.2)	9.7
Sobczyk-Guzenda et al. 2015 [11]		Direct	UV-Vis absorbance	3.13	---	3.19 (11.45)	---
Chen et al., 2015 [20]	Anatase	Indirect	UV-Vis reflectance	3.13	18	2.64 (1)	16.94
Larumbe et al., 2015 [22]	Mixed			2.96	---	2.68 (0.32)	---
Garza-Arévalo et al., 2016 [17]				3.11	16.3	2.4 (7)	7.3

3.9 Research questions

To obtain well-defined experimental data, the processing procedure applied in this work involved annealing in the gas phase of controlled oxygen activity. The effect of iron was examined at concentrations within the solubility limit. The techniques that allow atomic level control mixture include: the procedures which allow to mix the reagents either in liquid phase such as sol-gel or gas phase such as chemical vapour deposition. In order to assure iron distribution at the atomic level, specimens were processed using the sol-gel technique. Generally, the present work addresses the following questions:

1. What is the effect of acceptor-type dopants, such as iron, on the electronic structure of TiO_2, especially the band gap?

2. What is the effect of oxygen activity on the electronic structure of pure and Fe-doped TiO_2?
3. What is the effect of iron surface segregation on surface vs. bulk iron concentration in Fe-doped TiO_2?
4. What is the effect of oxygen activity on surface vs. bulk composition of Fe-doped TiO_2?
5. What is the effect of iron concentration on photocatalytic activity of TiO_2?
6. What is the effect of oxygen activity on photocatalytic activity of pure and Fe-doped TiO_2?
7. What are the optimal processing conditions, in terms of iron concentration and oxygen activity, to obtain the desired photocatalytic activity of Fe-doped TiO_2?
8. Based on the well-defined experimental data, what theoretical model can be developed which explains the effect of iron concentration on the electronic structure of TiO_2, segregation in TiO_2, and photocatalytic activity of TiO_2?

References

1. Li, X., P.-L. Yue, and C. Kutal, *Synthesis and photocatalytic oxidation properties of iron doped titanium dioxide nanosemiconductor particles.* New Journal of Chemistry, 2003. **27**(8): p. 1264-1269.
2. Wittke, J.P., *Solubility of Iron in TiO_2 (Rutile).* Journal of the American Ceramic Society, 1967. **50**(11): p. 586-588.
3. Busiakiewicz, A., *Solubility and precipitation of Fe on reduced TiO_2(001).* Thin Solid Films, 2014. **550**: p. 347-353.
4. Cordischi, D., et al., *Structural characterization of Fe/Ti oxide photocatalysts by X-ray, ESR, and Mössbauer methods.* Journal of Solid State Chemistry, 1985. **56**(2): p. 182-190.

5. Gazzoli, D., G. Minelli, and M. Valigi, *The FeO X TiO_2 system. An X-Ray diffraction, thermogravimetric and magnetic susceptibility study.* Materials chemistry and physics, 1989. **21**(1): p. 93-106.

6. Pownceby, M.I., M.J. Fisher-White, and V. Swamy, *Phase relations in the system Fe_2O_3–Cr_2O_3–TiO_2 between 1000 and 1300 C and the stability of (Cr, Fe) $2Ti_{n-2}O_{2n-1}$ crystallographic shear structure compounds.* Journal of Solid State Chemistry, 2001. **161**(1): p. 45-56.

7. Radecka, M., M. Rekas, and K. Zakrzewska. *Electrical and optical properties of undoped and Fe-doped TiO_2 single crystals*. in *Solid State Phenomena*. 1994. Trans Tech Publ.

8. Lin, M., et al., *Effect of single-cation doping and codoping with Mn and Fe on the photocatalytic performance of TiO_2 thin films.* international journal of hydrogen energy, 2014. **39**(36): p. 21500-21511.

9. Wang, M.C., H.J. Lin, and T.S. Yang, *Characteristics and optical properties of iron ion (Fe^{3+})-doped titanium oxide thin films prepared by a sol–gel spin coating*. Journal of Alloys and Compounds, 2009. **473**(1–2): p. 394-400.

10. Asiltürk, M., F. Sayılkan, and E. Arpaç, *Effect of Fe^{3+} ion doping to TiO_2 on the photocatalytic degradation of Malachite Green dye under UV and vis-irradiation.* Journal of Photochemistry and Photobiology A: Chemistry, 2009. **203**(1): p. 64-71.

11. Sobczyk-Guzenda, A., et al., *Plasma enhanced chemical vapor deposition of iron doped thin dioxide films, their structure and photowetting effect.* Thin Solid Films, 2015. **589**: p. 605-612.

12. Tang, W., et al., *Preparation of an Fe-doped visible-light-response TiO_2 film electrode and its photoelectrocatalytic activity.* Materials Science and Engineering: B, 2014. **187**: p. 39-45.

13. Tu, Y.-F., et al., *Preparation of Fe-doped TiO_2 nanotube arrays and their photocatalytic activities under visible light.* Materials Research Bulletin, 2010. **45**(2): p. 224-229.

14. Wei, X., et al., *Iron-doped TiO_2 nanotubes with high photocatalytic activity under visible light synthesized by an ultrasonic-assisted sol-hydrothermal method.* Ceramics International, 2013. **39**(4): p. 4009-4016.

15. Yu, J., Q. Xiang, and M. Zhou, *Preparation, characterization and visible-light-driven photocatalytic activity of Fe-doped titania nanorods and first-principles study for electronic structures.* Applied Catalysis B: Environmental, 2009. **90**(3–4): p. 595-602.

16. George, S., et al., *Role of Fe Doping in Tuning the Band Gap of TiO_2 for the Photo-Oxidation-Induced Cytotoxicity Paradigm.* Journal of the American Chemical Society, 2011. **133**(29): p. 11270-11278.

17. Garza-Arévalo, J.I., et al., *Fe doped TiO_2 photocatalyst for the removal of As(III) under visible radiation and its potential application on the treatment of As-contaminated groundwater.* Materials Research Bulletin, 2016. **73**: p. 145-152.

18. Adán, C., et al., *Phenol photodegradation with oxygen and hydrogen peroxide over TiO2 and Fe-doped TiO_2.* Catalysis Today, 2009. **143**(3–4): p. 247-252.

19. Delekar, S.D., et al., *Structural refinement and photocatalytic activity of Fe-doped anatase TiO2 nanoparticles.* Applied Surface Science, 2012. **263**: p. 536-545.

20. Chen, C.-C., S.-H. Hu, and Y.-P. Fu, *Effects of surface hydroxyl group density on the photocatalytic activity of Fe^{3+}-doped TiO_2.* Journal of Alloys and Compounds, 2015. **632**: p. 326-334.

21. Tong, T., et al., *Preparation of Fe^{3+}-doped TiO_2 catalysts by controlled hydrolysis of titanium alkoxide and study on their photocatalytic activity for methyl orange degradation.* Journal of Hazardous Materials, 2008. **155**(3): p. 572-579.

22. Larumbe, S., M. Monge, and C. Gómez-Polo, *Comparative study of (N, Fe) doped TiO_2 photocatalysts.* Applied Surface Science, 2015. **327**: p. 490-497.

23. Johan, M.R., et al., *Annealing effects on the properties of copper oxide thin films prepared by chemical deposition.* Int. J. Electrochem. Sci, 2011. **6**: p. 6094-6104.

24. Bernasik, A., et al., *Electrical surface versus bulk properties of Fe-doped TiO_2 single crystals.* Solid State Ionics, 1994. **72**: p. 12-18.

25. Hirschwald, W., et al., *Effect of temperature on chromium segregation to CoO (100) and NiO (100) surfaces.* Surface and Interface Analysis, 1989. **14**(8): p. 477-481.

26. Bickley, R.I., et al., *Characterisation of iron/titanium oxide photocatalysts. Part 2.—Surface studies.* Journal of the Chemical Society, Faraday Transactions, 1994. **90**(15): p. 2257-2264.

27. Pecchi, G., et al., *Effect of precursors on surface and catalytic properties of Fe/TiO_2 catalysts.* Journal of Chemical Technology and Biotechnology, 2002. **77**(8): p. 944-949.

28. Ambrus, Z., et al., *Synthesis, structure and photocatalytic properties of Fe(III)-doped TiO_2 prepared from TiCl3.* Applied Catalysis B: Environmental, 2008. **81**(1–2): p. 27-37.

29. Adán, C., et al., *New insights on solar photocatalytic degradation of phenol over Fe-TiO_2 catalysts: Photo-complex mechanism of iron lixiviates.* Applied Catalysis B: Environmental, 2009. **93**(1–2): p. 96-105.

30. Deng, L., et al., *Synthesis, Characterization of Fe-doped TiO_2 Nanotubes with High Photocatalytic Activity.* Catalysis Letters, 2009. **129**(3-4): p. 513-518.

31. Li, J., et al., *Direct hydro-alcohol thermal synthesis of special core–shell structured Fe-doped titania microspheres with extended visible light response and enhanced photoactivity.* Applied Catalysis B: Environmental, 2009. **85**(3): p. 162-170.

32. Bajnóczi, É.G., et al., *The influence of the local structure of Fe(III) on the photocatalytic activity of doped TiO_2 photocatalysts—An EXAFS, XPS and Mössbauer spectroscopic study.* Applied Catalysis B: Environmental, 2011. **103**(1–2): p. 232-239.

33. Mangham, A.N., et al., *Photochemical properties, composition, and structure in molecular beam epitaxy grown Fe "doped" and (Fe, N) codoped rutile TiO2 (110).* The Journal of Physical Chemistry C, 2011. **115**(31): p. 15416-15424.

34. Liu, T. and H. Zhang, *Novel Fe-doped anatase TiO_2 nanosheet hierarchical spheres with 94%{001} facets for efficient visible light photodegradation of organic dye.* RSC Advances, 2013. **3**(37): p. 16255-16258.

35. Andersson, P., E. Kollberg, and A. Jelenski, *Charge compensation in iron-doped rutile.* Journal of Physics C: Solid State Physics, 1974. **7**(10): p. 1868.

36. Bally, A., et al., *Structural and electrical properties of Fe-doped thin films.* Journal of Physics D: Applied Physics, 1998. **31**(10): p. 1149.

37. Sasaki, J., N. Peterson, and L. De Jonghe. *Fast diffusion of iron in single crystal rutile and iron doped rutile*. in *MRS Proceedings*. 1983. Cambridge Univ Press.

38. Janes, R., L.J. Knightley, and C.J. Harding, *Structural and spectroscopic studies of iron (III) doped titania powders prepared by sol-gel synthesis and hydrothermal processing.* Dyes and Pigments, 2004. **62**(3): p. 199-212.

39. Fan, L., J. Dongmei, and M. Xueming, *The effect of milling atmospheres on photocatalytic property of Fe-doped TiO2 synthesized by mechanical alloying.* Journal of Alloys and Compounds, 2009. **470**(1–2): p. 375-378.

40. Zhou, M., et al., *Preparation and photocatalytic activity of Fe-doped mesoporous titanium dioxide nanocrystalline photocatalysts.* Materials Chemistry and Physics, 2005. **93**(1): p. 159-163.

41. Wang, S., et al., *Photocatalytic property of Fe doped anatase and rutile TiO_2 nanocrystal particles prepared by sol–gel technique.* Applied Surface Science, 2012. **263**: p. 260-265.

42. Khan, H. and I.K. Swati, *Fe^{3+}-doped Anatase TiO_2 with d–d Transition, Oxygen Vacancies and Ti^{3+} Centers: Synthesis, Characterization, UV–vis*

Photocatalytic and Mechanistic Studies. Industrial & Engineering Chemistry Research, 2016.

43. Dang, T.M.D., T.M.H. Nguyen, and H.P. Nguyen, *The preparation of nano-gold catalyst supported on iron doped titanium oxide.* Advances in Natural Sciences: Nanoscience and Nanotechnology, 2010. **1**(2): p. 025011.

44. Chang, S.-m. and W.-s. Liu, *The roles of surface-doped metal ions (V, Mn, Fe, Cu, Ce, and W) in the interfacial behavior of TiO2 photocatalysts.* Applied Catalysis B: Environmental, 2014. **156–157**: p. 466-475.

45. Hirano, M., et al., *Direct Formation of Iron (III)-Doped Titanium Oxide (Anatase) by Thermal Hydrolysis and Its Structural Property.* Journal of the American Ceramic Society, 2004. **87**(1): p. 35-41.

46. Gao, Q., X. Wu, and Y. Fan, *The effect of iron ions on the anatase–rutile phase transformation of titania (TiO_2) in mica–titania pigments.* Dyes and Pigments, 2012. **95**(1): p. 96-101.

47. Gennari, F. and D. Pasquevich, *Kinetics of the anatase–rutile transformation in TiO_2 in the presence of Fe_2O_3.* Journal of Materials Science, 1998. **33**(6): p. 1571-1578.

48. Iida, Y. and S. Ozaki, *Grain growth and phase transformation of titanium oxide during calcination.* Journal of the American Ceramic Society, 1961. **44**(3): p. 120-127.

49. Zhang, W., et al., *Surface modification of TiO_2 film by iron doping using reactive magnetron sputtering.* Chemical Physics Letters, 2003. **373**(3–4): p. 333-337.

50. Nahar, M.S., K. Hasegawa, and S. Kagaya, *Photocatalytic degradation of phenol by visible light-responsive iron-doped TiO_2 and spontaneous sedimentation of the TiO_2 particles.* Chemosphere, 2006. **65**(11): p. 1976-1982.

51. Zhou, M., J. Yu, and B. Cheng, *Effects of Fe-doping on the photocatalytic activity of mesoporous TiO_2 powders prepared by an ultrasonic method.* Journal of Hazardous Materials, 2006. **137**(3): p. 1838-1847.

52. Liu, S. and Y. Chen, *Enhanced photocatalytic activity of TiO_2 powders doped by Fe unevenly.* Catalysis Communications, 2009. **10**(6): p. 894-899.

53. Mathews, N., et al., *Structural and spectroscopic study of the Fe doped TiO2 thin films for applications in photocatalysis.* physica status solidi (c), 2009. **6**(S1): p. S219-S223.

54. Fàbrega, C., et al., *Location and catalytic role of iron species in TiO_2:Fe photocatalysts: An EPR study.* Journal of Photochemistry and Photobiology A: Chemistry, 2010. **211**(2–3): p. 170-175.

55. Naeem, K. and F. Ouyang, *Preparation of Fe^{3+}-doped TiO_2 nanoparticles and its photocatalytic activity under UV light.* Physica B: Condensed Matter, 2010. **405**(1): p. 221-226.

56. Wan, L., et al., *Phase selection and visible light photo-catalytic activity of Fe-doped TiO_2 prepared by the hydrothermal method.* Materials Research Bulletin, 2011. **46**(3): p. 442-446.

57. Pang, Y.L. and A.Z. Abdullah, *Effect of low Fe^{3+} doping on characteristics, sonocatalytic activity and reusability of TiO_2 nanotubes catalysts for removal of Rhodamine B from water.* Journal of Hazardous Materials, 2012. **235–236**: p. 326-335.

58. Crişan, M., et al., *Sol–gel iron-doped TiO_2 nanopowders with photocatalytic activity.* Applied Catalysis A: General, 2014. **504**: p. 130-142.

59. Bansode, A.S., et al., *Reusable thin film photocatalyst of Fe-doped TiO_2 deposited by ECR plasma.* Surface and Interface Analysis, 2015. **47**(1): p. 22-29.

60. Cronemeyer, D., *Infrared absorption of reduced rutile TiO_2 single crystals.* Physical Review, 1959. **113**(5): p. 1222.

61. Gupta, V.P. and N.M. Ravindra, *Optoelectronic properties of rutile (TiO2).* Journal of Physics and Chemistry of Solids, 1980. **41**(6): p. 591-594.

62. Nowotny, M., T. Bak, and J. Nowotny, *Electrical properties and defect chemistry of TiO_2 single crystal. I. Electrical conductivity.* The Journal of Physical Chemistry B, 2006. **110**(33): p. 16270-16282.

63. Fox, H., et al., *Bulk and Surface Properties of Rutile TiO_2 from Self-Consistent-Charge Density Functional Tight Binding.* Journal of Chemical Theory and Computation, 2010. **6**(2): p. 499-507.

64. Zhang, J., et al., *New understanding of the difference of photocatalytic activity among anatase, rutile and brookite TiO_2.* Physical Chemistry Chemical Physics, 2014. **16**(38): p. 20382-20386.

65. Tang, H., et al., *Electrical and optical properties of TiO_2 anatase thin films.* Journal of applied physics, 1994. **75**(4): p. 2042-2047.

66. Jagadale, T.C., et al., *N-Doped TiO_2 Nanoparticle Based Visible Light Photocatalyst by Modified Peroxide Sol−Gel Method.* The Journal of Physical Chemistry C, 2008. **112**(37): p. 14595-14602.

67. Carneiro, J., et al., *Synthesis of iron-doped TiO_2 nanoparticles by ball-milling process: the influence of process parameters on the structural, optical, magnetic, and photocatalytic properties.* Journal of materials science, 2014. **49**(21): p. 7476-7488.

68. Sood, S., et al., *Highly effective Fe-doped TiO_2 nanoparticles photocatalysts for visible-light driven photocatalytic degradation of toxic organic compounds.* Journal of colloid and interface science, 2015. **450**: p. 213-223.

69. Yan, J., et al., *Facile synthesis of an iron doped rutile TiO_2 photocatalyst for enhanced visible-light-driven water oxidation.* Journal of Materials Chemistry A, 2015.

70. Lin, H.-J., et al., *Optical and photocatalytic properties of Fe^{3+}-doped TiO_2 thin films prepared by a sol–gel spin coating.* Ceramics International, 2014. **40**(7, Part B): p. 10633-10640.

CHAPTER FOUR

4 Experimental Procedures

This chapter details the preparation of the catalyst and characterization of the obtained specimens. Sol-gel technique was used for sample preparation. Proton induced X-ray emission (PIXE), X-ray photoelectron spectroscopy (XPS) and secondary ion mass spectrometry (SIMS) were employed for chemical analysis of the samples and scanning electron microscopy (SEM) was used for the determination of surface morphologies.

Band gap was determined from the UV-Vis spectrophotometry data. Photocatalytic activity of the specimens was examined by the oxidation of methylene blue (MB) as a testing compound.

4.1 Preparation of the specimen

4.1.1 Sol-gel technique

Titanium isopropoxide (TTIP), iron nitrate [$Fe(NO_3)_3.9H_2O$], acetic acid, ethanol and water were used as precursors to prepare the Fe-doped TiO_2 specimens. The ratio of acetic acid to titanium and titanium to deionized water was adjusted to 1.5:1 and 1:4, respectively for proper hydrolysis reaction [1, 2]. The amount of ethanol was adjusted to achieve a concentration of 0.8 mol/L of titanium in the final solution to produce homogeneous monolithic gel [2]. Three beakers (B1, B2 and B3) were used to prepare the solutions. For example, the amounts required to prepare 0.05 at%

Fe-doped TiO_2 specimen are titanium isoproxide = 92.68 mL, water = 26.828 mL, acetic acid = 22.55 mL and ethanol = 379.69 mL.

- $Fe(NO_3)_3.9H_2O$ powder was mixed with ethanol in B1 and stirred until fully dissolved. The selected amount of iron nitrate was added to the solution to obtain the desired iron concentration in Fe-doped TiO_2.
- TTIP was added to acetic acid in B2 under vigorous stirring.
- The remaining amount of ethanol was mixed with deionized water in B3.

Then, the solution from B1 was poured slowly into B2 while stirring continuously. After 1 hour, the B3 solution was added drop wise to the B2 under stirring. Shortly later, the gel was formed and the beaker was placed on the hot plate in a fume cabinet at 353 K for 2-3 days to dry.

4.1.2 Formation of solid solution by high temperature processing

After drying, the obtained solid product was ground into fine powder using an agate mortar. Then, the powder was placed inside a platinum-lined alumina boat for calcination at 773 K for 3 hours in an opened tube furnace with a ramp rate of 5 °C/min. The calcined powder was mixed with 1% of paraffin wax acting as a binder and formed into a pellet (1.9-2 mm thickness) by pressing uniaxially with a load of one ton. The binder was removed by heating at 873 K for 10 hours in air. Then, the pellets were sintered at 1373 K for 5 hours for densification. The specimen of pure TiO_2 was prepared in the same way without adding $Fe(NO_3)_3.9H_2O$.

4.1.3 Sample processing

The surface of the sintered polycrystalline pellet is rough; however, the characterization techniques, such as SIMS and XPS, require flat and smooth areas to

probe. Therefore, the specimens were polished on grade P240 sand paper. Two series of polycrystalline specimens were prepared:

- The specimens of Fe-doped TiO_2 (including the specimen containing 0.18 at% Fe) were re-annealed at 1273 K for 24 hours in the gas phase of oxygen activities in the range 10^{-12} Pa < $p(O_2)$ < 10^5 Pa:
  - Pure oxygen, $p(O_2)$ = 100 kPa
  - Artificial air (79% argon and 21% oxygen), $p(O_2)$ = 21 kPa
  - Argon, $p(O_2)$ = 10 Pa
  - Argon/ 1% of hydrogen, $p(O_2) = 10^{-12}$ Pa at 1273 K
- The specimens of Fe-doped TiO_2, including 0.05 – 1.4 at% Fe, were re-annealed at 1373 K in two different oxygen activities: $p(O_2)$ = 21 kPa and 10^{-10} Pa.

The single crystal of Fe-doped TiO_2, involving 0.1 at% Fe, (size = 10x10x2 mm) was provided by Shinkosha, Japan. The specimens were annealed at 1273 K for 24 hours in two different oxygen activities: 100 kPa and 10^{-12} Pa.

All specimens were cooled down to room temperature without changing the gas phase environment. The zirconia-based electrochemical oxygen probe has been applied for monitoring oxygen activity during the experiments [1]. The effects of polishing and annealing are schematically represented in **Figure 4-1** showing the surface microstructure after sintering (a), after polishing (b), and after subsequent re-annealing (c). The flow diagram of the preparation technique of polycrystalline specimen is shown in **Figure 4-2**.

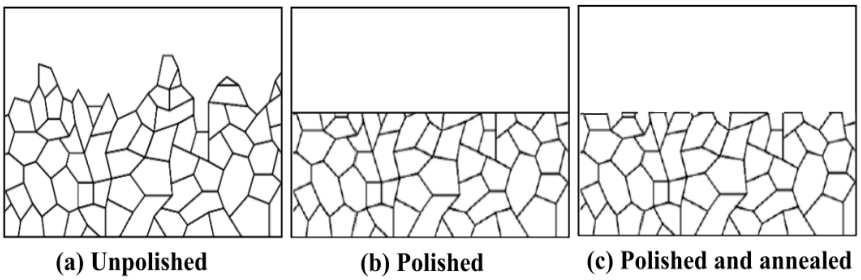

Figure 4-1: The schematic representation of the surface microstructure of the specimen.

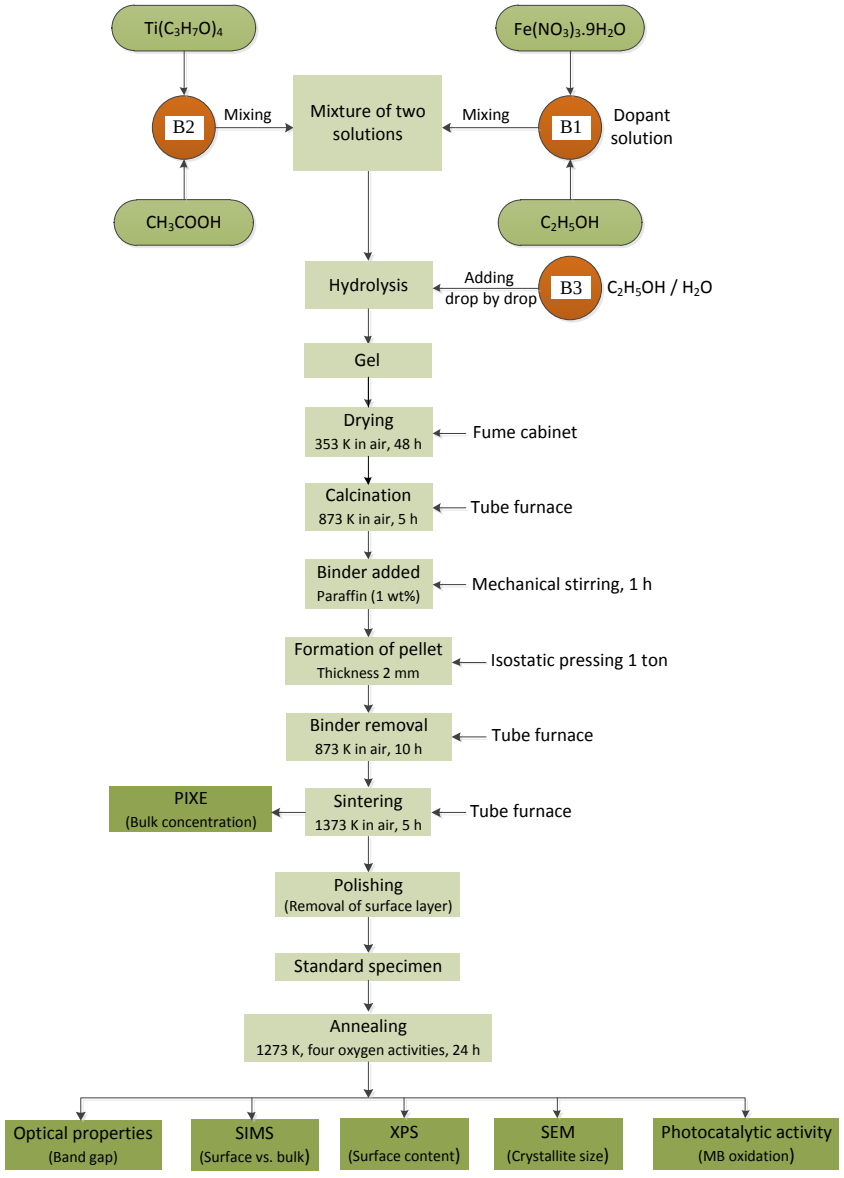

Figure 4-2: Flow diagram of the processing procedure in the formation of polycrystalline Fe-doped TiO_2 specimen with subsequent analysis. Where, B1, B2 and B3 represent the beaker 1, beaker 2 and beaker 3, respectively.

4.2 Determination of oxygen activity

The zirconia-based oxygen sensor, which is shown in **Figure 4-3,** was used to determine the oxygen activity. The zirconia probe is made of YSZ (yttria-stabilised zirconia) pellet with deposited porous platinum electrodes on both sides, and supported inside an alumina tube. The Nernst-Einstein equation was used to determine the oxygen activity:

$$E = \frac{k_B T}{4} \ln \frac{p(O_2)_X}{p(O_2)_{air}} \qquad \textbf{(4-1)}$$

where, E is the voltage (mV), k_B is the Boltzman constant, T is the absolute temperature (K), $p(O_2)_x$ is the studied oxygen activity and $p(O_2)_{air}$ is the reference oxygen activity. The gas flow rate was maintained at 100 ml/min by mass-flow controllers (Mass-trak, Sierra instruments Inc.)

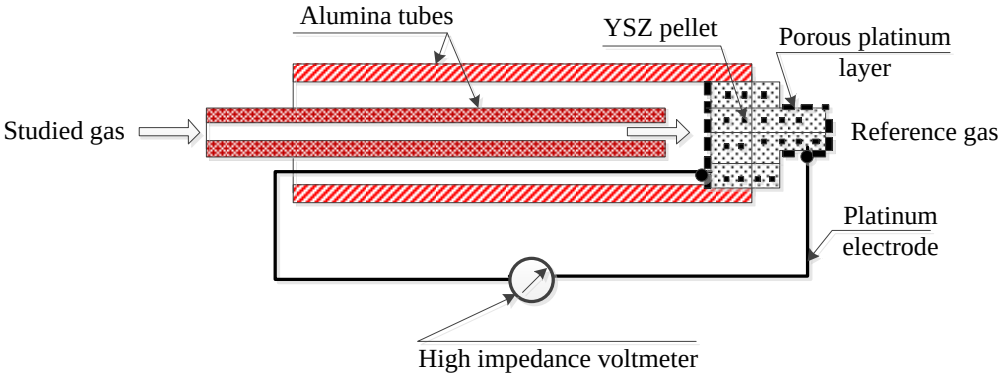

Figure 4-3: The schematic illustration of an yttria-stabilised zirconia (YSZ) electrochemical oxygen sensor.

4.3 Characterization of the specimens

4.3.1 Bulk analysis using proton induced X-ray emission (PIXE)

The bulk chemical analysis was performed using the proton-induced X-ray emission, PIXE (on the 2MV STAR tandem accelerator) at Australian Nuclear Science and Technology Organisation (ANSTO). As shown in **Figure 4-4**, the incident ion from

the accelerator hits the inner-shell electron and produces a vacancy. This vacancy is filled up by an electron from the outer-shell; an X-ray of characteristic energy related to that particular atom is then emitted and detected. A 2.6 MeV proton beam of 10-15 nA beam current, collimated to 3 mm, was directed to the specimen at a normal angle. The generated X-rays were detected using a Si(Li) detector with an attached 25 µm thick Be window. However, due to the thick specimens and high X-ray yields, the Si(Li) detector could easily be overloaded. Therefore, an additional pinhole filter (1700-µm thick acrylic with 2% hole area) fitted with 4-µm thick mylar film was applied to decrease the intensity of the low energy X-rays excited with the high cross sections. The elemental bulk concentrations were determined from the obtained X-ray spectra using the GUPIXWIN software package (Version 2.1.4, University of Guelph, Canada). The PIXE spectra obtained for as-sintered Fe-doped TiO_2 specimens are shown in **Figure 4-5**.

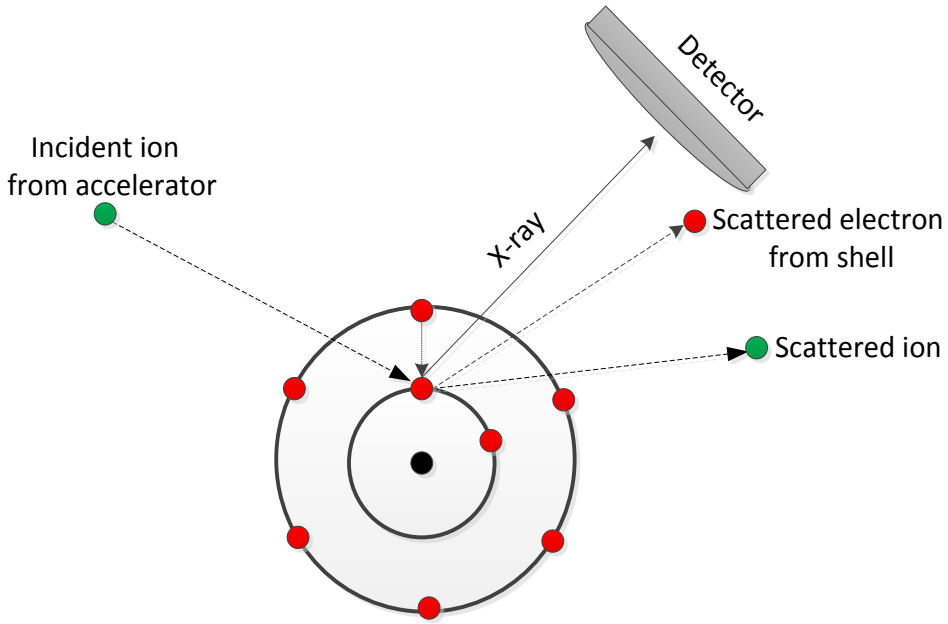

Figure 4-4: The schematic representation of the inner-shell vacancy creation due to high energy particle interaction and subsequent X-ray emission.

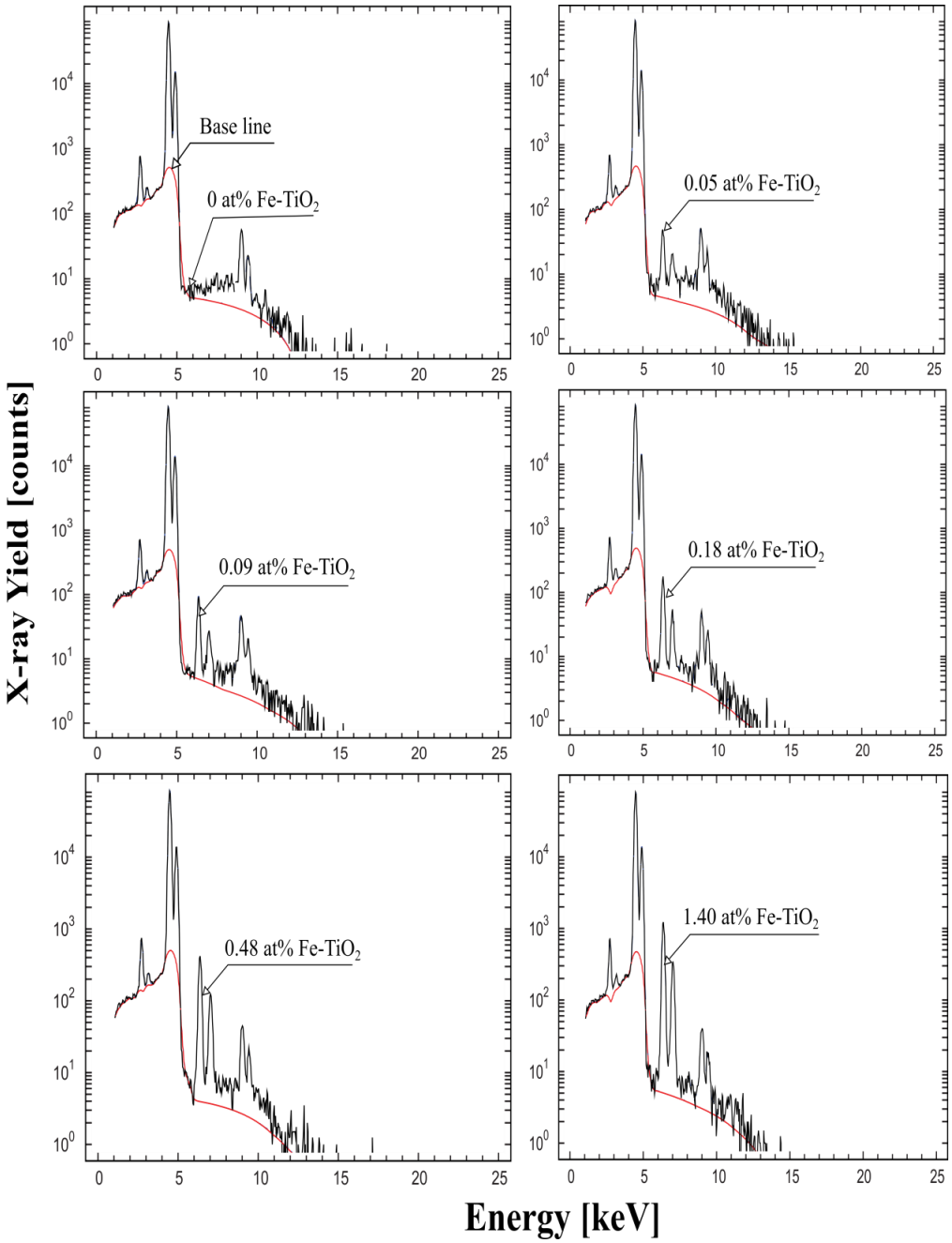

Figure 4-5: The PIXE analysis results for Fe-doped TiO_2 polycrystalline specimens.

The bulk concentration of iron and other extrinsic elements was determined from the surface area of the related peaks. The results of the PIXE analysis, including the concentration of iron and main impurities, are included in **Table 4-1**.

Table 4-1: The results of elemental bulk concentrations of Fe-doped TiO_2 specimen obtained from PIXE technique.

Theoretical amount of Fe [at%]	Actual concentrations in specimen [at%]						
	Fe	Ti	K	Cl	Ni	Zn	Ta
0.00	**0.000523**	99.78532	0.009018	0.190912	0.003604	0.002773	0.003145
0.05	**0.052197**	99.74146	0.013127	0.177369	0.003343	0.003386	0.004115
0.10	**0.093243**	99.73886	0.000258	0.156173	0.002582	0.002704	0.003182
0.20	**0.182628**	99.58811	0.007688	0.210530	0.001679	0.002110	0.002260
0.50	**0.487143**	99.35311	0.010537	0.150471	0.002621	0.00296	0.003154
1.50	**1.402419**	98.36783	0.012755	0.210522	0.002774	0.000778	0.002924

As seen in **Table 4-1**, the bulk concentration of iron in all the specimens differs slightly from the intentional amount imposed during chemical processing. As also seen, the specimens include minor concentrations of aliovalent impurities, such as potassium, nickel, zinc and tantalum. The amount of chlorine present in the specimen was substantial, however, the effect of chlorine on the properties of TiO_2 can be ignored if the specimens are annealed at 573 K and beyond [3].

4.3.2 Microstructure

The surface morphology of the ceramic samples was examined using a scanning electron microscopy. A thin carbon layer was deposited on the surface of the specimens in order to prevent the development of a surface charge. The carbon deposition procedure was done in a vacuum. The Zeiss Ultra Plus with Oxford instrument X-ray microanalysis system at ANSTO was used to obtain the SEM micrographs. The image of each specimen was captured in-lens of secondary electron detectors. The effect of iron concentration and oxygen activity on surface morphology of TiO_2 is shown in **Figure 4-6 a** and **4-6 b**, respectively.

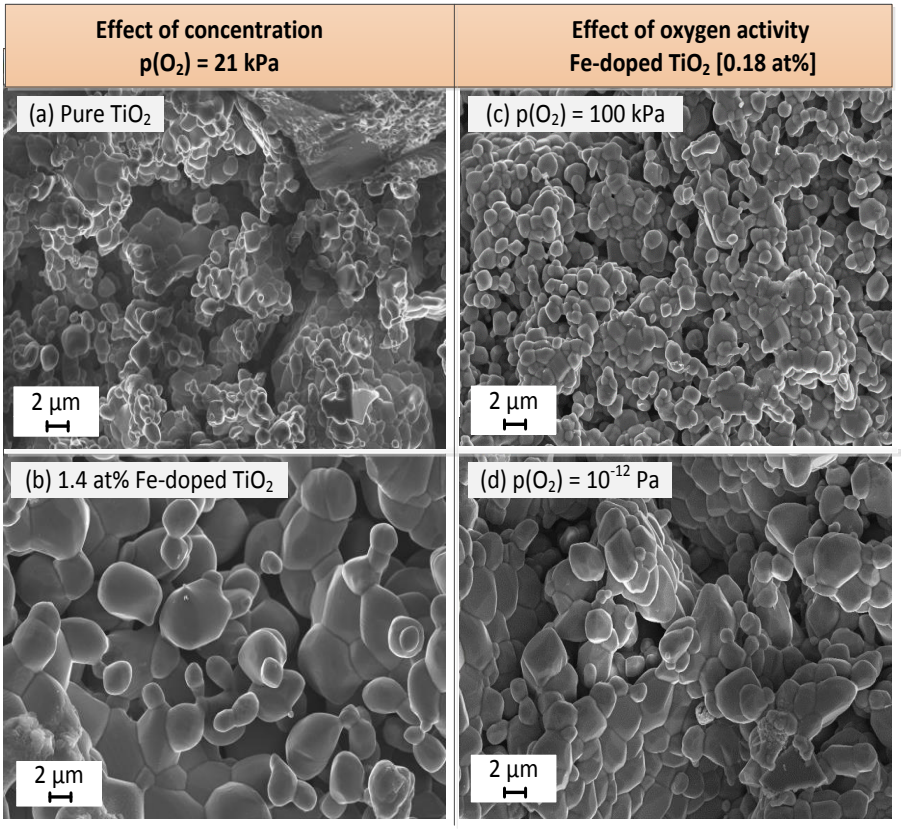

Figure 4-6 a: The SEM micrographs for pure TiO_2 (a) and 1.4 at% Fe-doped TiO_2 (b), both a and b were annealed at 1373 K for 24 h in artificial air, and Fe-doped TiO_2, containing 0.18 at% Fe, annealed at 1273 K for 24 hours in oxygen activities corresponding to 100 kPa (c), and 10^{-12} Pa (d).

As seen in **Figure 4-6** a, the grain size increases due to the incorporation of iron into TiO_2 lattice, and the average grain size for pure TiO_2 and 1.4 at% Fe-doped TiO_2 is 1.3 µm and 3.1 µm, respectively. On the other hand, the average grain size of 0.18 at% Fe-doped TiO_2 is larger (2.56 µm) in reducing condition compared to the specimen annealed in oxidising condition (1.8 µm). As seen in **Figure 4-6 b**, the changes of grain size is insignificant.

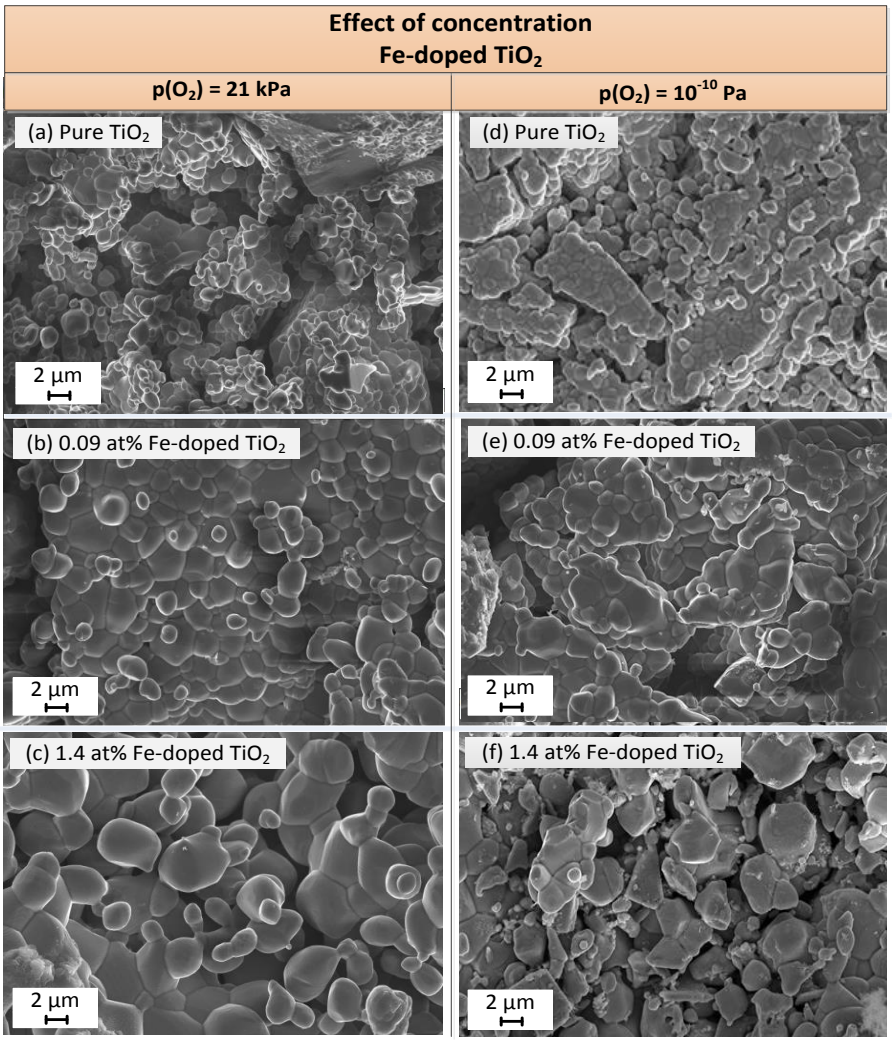

Figure 4-6 b: The SEM images showing the effect of iron doping on grain size of Fe-doped TiO_2, involving iron concentration from 0.05 to 1.4 at%, annealed at 1373 K for 24 hours in two different oxygen activities: 21 kPa (a, b, c) and 10^{-10} Pa (d, e, f).

4.3.3 Depth profile analysis by secondary ion mass spectrometry (SIMS)

The concentration-depth profiles of the chemical elements of interest were determined by secondary ion mass spectrometry, SIMS (Cameca IMS 5f). The principle of the method is shown in **Figure 4-7**. Prior to the measurement, the surface of the studied specimens was covered with a 15 nm thick gold layer in order

to avoid the charging effect. The solid samples were then sputtered by primary ions, such as oxygen, with 7.5 keV net impact energy and 30 nA beam current, and rastered over the area of approximately 180 μm x 180 μm. Ejected secondary ions were analysed by the mass spectrometer that provides information about elemental chemical composition of the sputtered layer.

The average sputtering rate (the crater depth/the sputtering time) was calculated using the crater depth, as measured by a stylus profilometer (Alpha-Step IQ, KLA-Tencor). To avoid the effect of crater edge, the analysis was performed on a smaller area within the specified rastered zone. The intensity ratio of ^{56}Fe to ^{47}Ti was used to determine the enrichment factor, *f*, of iron in Fe-doped TiO_2, which is defined as:

$$f = \frac{(C_{Fe})_{surface}}{(C_{Fe})_{Bulk}} = \frac{(I_{Fe} / I_{Ti})_{surface}}{(I_{Fe} / I_{Ti})_{bulk}} \quad \textbf{(4-2)}$$

where, $(C_{Fe})_{surface}$ *and* $(C_{Fe})_{bulk}$ represents the concentration of iron at the surface and in the bulk, respectively, I_{Fe} and I_{Ti} represents the intensity count of iron and titanium, respectively.

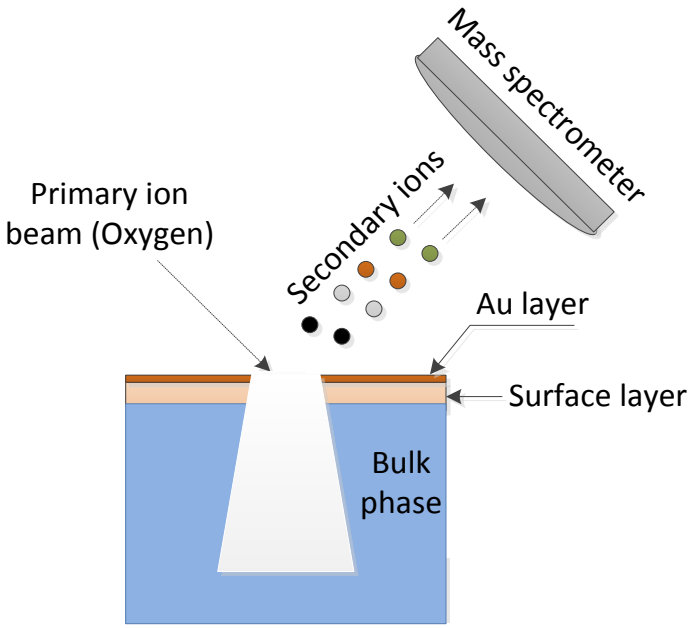

Figure 4-7: The schematic representation of performance principle of the SIMS analysis.

4.3.4 Surface analysis using X-ray photoelectron spectroscopy (XPS)

The elemental concentration and oxidation state of the selected species at the surface of the specimen were determined using XPS (ESCALAB 250xi). Before performing the XPS experiment, the sample surface was sputtered with argon ion beam (3 keV) to remove the unwanted impurities, such as carbon, introduced due to polishing. The 150 W (13 kV×12 mA) power source of monochromatic X-rays [Al Kα (1486.68 eV)] was used to eject electrons from the solid sample. A photoelectron take-off angle was set to 90° relative to the surface plane to examine the concentration of iron within the surface layer of approximately 6 nm. A pass energy filter of 100 eV for survey scans and 20 eV for regions of interest was used. An electron energy analyser was used to provide information about the energy of the emitted electrons. The

identity, chemical state, and quantity of the detected element were determined from the binding energy and the intensity of photoelectron peaks.

4.3.5 Determination of the band gap

An UV−Vis−NIR spectrophotometer (Agilent Cary 5000) with an integrating sphere attachment (DRA-2500) was used in a reflectance mode to determine the band gap. The instrument was calibrated by placing a polytetrafluoroethylene (PTFE) standard plate on the reference port (100% reflectance). The reflectance of each sample was measured in the wavelength range of 200−800 nm with a scan rate of 600 nm/min. The band gap of Fe-doped TiO_2 was determined by plotting $(F(R)\times h\nu)^2$ as a function of energy, hν (Tauc plot [4, 5]), and then extrapolating the linear portion of the graph to intersect with the energy axis.

$$(F(R)\times h\nu)^2 = 0 \qquad \textbf{(4-3)}$$

The direct transition model was used here to determine the band gap as theoretical studies show that rutile is a direct band gap semiconductor [6, 7].

The Kubelka –Munk function, *F(R),* was calculated using the equation [8]:

$$F(R) = \frac{(1-R)^2}{2R} = \alpha/s \qquad \textbf{(4-4)}$$

where, *R* is reflectance, *α* is the light absorption coefficient, and *s* is the light scattering coefficient. When the size of grains in a polycrystalline specimen is large comparing to the wavelength of the incident light beam, then the scattering coefficient is assumed to be constant. Consequently, for such a case, *F(R)* is proportional to the absorption coefficient, *α,* and can be used in a construction of the Tauc plot.

4.3.6 Photocatalytic activity

The testing of photocatalytic performance of the photocatalysts was conducted by the mineralization of aqueous methylene blue (MB) solution under simulated solar light (Oriel Sol3A solar simulator, model 94043A). **Figure 4-8** shows the schematic representation of the photo-reactor for the light-induced oxidation of MB.

The working distance between the lens of the solar simulator and the surface of the ceramic sample was 10 cm. The light irradiance used in these experiments was set to 1000 W/m^2 (1 sun). The sample was placed inside a 10 mL beaker filled with MB solution on a Teflon support. A magnetic stirring bar under the support kept the solution homogeneous. At the initial stage, the whole device was kept in the dark for 2 hours to check the absorption of MB, starting from the initial concentration of 10^{-5} mol/L.

The set-up was then exposed to light to start the experiment and a small amount of the solution was drawn from the beaker every 15 minutes and its absorbance spectra was measured by the spectrophotometer (Agilent Cary 5000 UV-Vis-NIR). The tested solution was poured back into the beaker each time after measuring the absorbance, so the total volume of the solution remained unchanged. The change in the MB concentration was determined from the height of the absorbance peak at ~665 nm for all samples.

The rate constant (k) of the decomposition reaction was determined from the following equation, assuming first-order kinetics [9, 10] because *ln* (C_o/C_t) vs. reaction time, *t* yields a straight line:

$$\ln\left(\frac{C_o}{C_t}\right) = kt \qquad \textbf{(4-5)}$$

where, C_o and C_t represent the concentration of MB at the beginning of the experiment and after time, t, respectively.

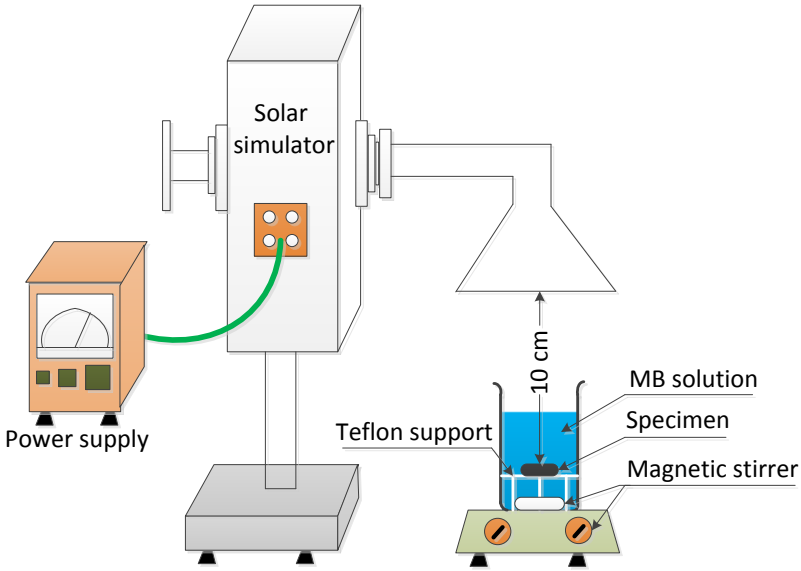

Figure 4-8: The schematic representation of the photo-reactor for the light-induced oxidation of MB. A 450-W xenon lamp was used as the light source in the Oriel solar simulator (model 94043A).

References

1. Atanacio, A.J., T. Bak, and J. Nowotny, *Effect of Indium Segregation on the Surface versus Bulk Chemistry for Indium-Doped TiO_2.* ACS applied materials & interfaces, 2012. **4**(12): p. 6626-6634.

2. Doeuff, S., et al., *Hydrolysis of titanium alkoxides: modification of the molecular precursor by acetic acid.* Journal of Non-crystalline solids, 1987. **89**(1-2): p. 206-216.

3. Long, M., et al., *Preparation, characterization and photocatalytic activity of visible light driven chlorine-doped TiO_2.* Frontiers of chemistry in China, 2007. **2**(3): p. 278-282.

4. López, R. and R. Gómez, *Band-gap energy estimation from diffuse reflectance measurements on sol–gel and commercial TiO_2: a comparative study.* Journal of sol-gel science and technology, 2012. **61**(1): p. 1-7.

5. Tauc, J., R. Grigorovici, and A. Vancu, *Optical properties and electronic structure of amorphous germanium.* physica status solidi (b), 1966. **15**(2): p. 627-637.

6. Fox, H., et al., *Bulk and Surface Properties of Rutile TiO_2 from Self-Consistent-Charge Density Functional Tight Binding.* Journal of Chemical Theory and Computation, 2010. **6**(2): p. 499-507.

7. Zhang, J., et al., *New understanding of the difference of photocatalytic activity among anatase, rutile and brookite TiO_2.* Physical Chemistry Chemical Physics, 2014. **16**(38): p. 20382-20386.

8. Frei, R.W. and H. Zeitlin, *Diffuse reflectance spectroscopy*. Wiley Online Library, 1971.

9. Castro, A.L., et al., *Doped titanium dioxide nanocrystalline powders with high photocatalytic activity*. Journal of Solid State Chemistry, 2009. **182**(7): p. 1838-1845.

10. Crişan, M., et al., *Sol–gel iron-doped TiO_2 nanopowders with photocatalytic activity.* Applied Catalysis A: General, 2014. **504**: p. 130-142.

CHAPTER FIVE

5 Results and discussions

5.1 Electronic structure of Fe-doped TiO_2

5.1.1 Effect of iron concentration

Figure 5-1 shows the effect of iron concentration on the reflectance spectra of Fe-doped TiO_2. As seen, the incorporation of iron results in modification of the absorption edge.

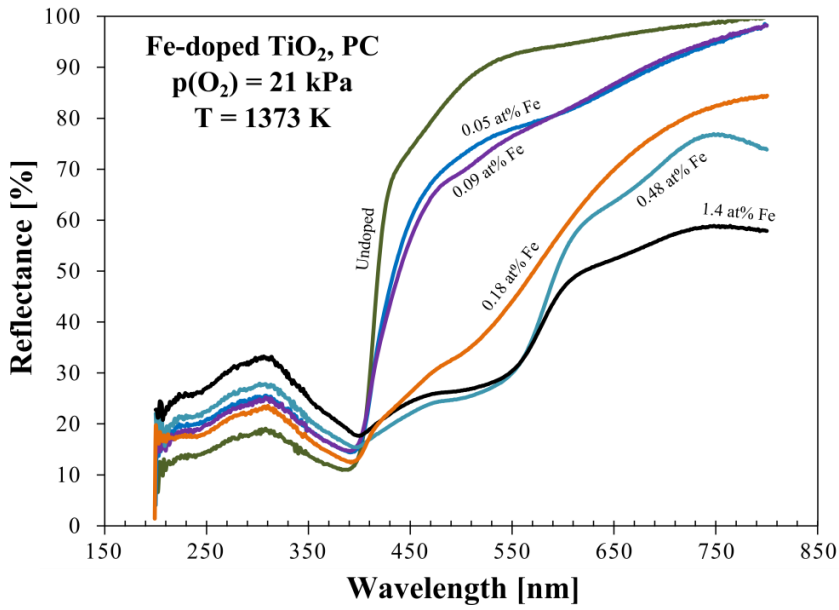

Figure 5-1: The reflectance spectra for Fe-doped TiO_2, involving iron concentration from 0.05 to 1.4 at%, all specimens annealed at 1373 K in artificial air [$p(O_2)$ = 21 kPa].

The Tauc plots for Fe-doped TiO_2 were drawn using Kubelka-Munk function and these are shown in **Figure 5-2.** The fundamental absorption edge moves towards the lower energy value with increased iron concentration**.** The secondary absorption edge was observed for the concentration of iron 0.18 at% and beyond. The band gap, E_g, was determined from the value of the abscissa corresponding to the point of intersection with the extrapolated linear part of the graph. The photon energy, $h\nu$ (eV) was calculated from the relation, $h\nu = (1239.8/\lambda)$, where, λ is the wavelength of the incident light in nanometres.

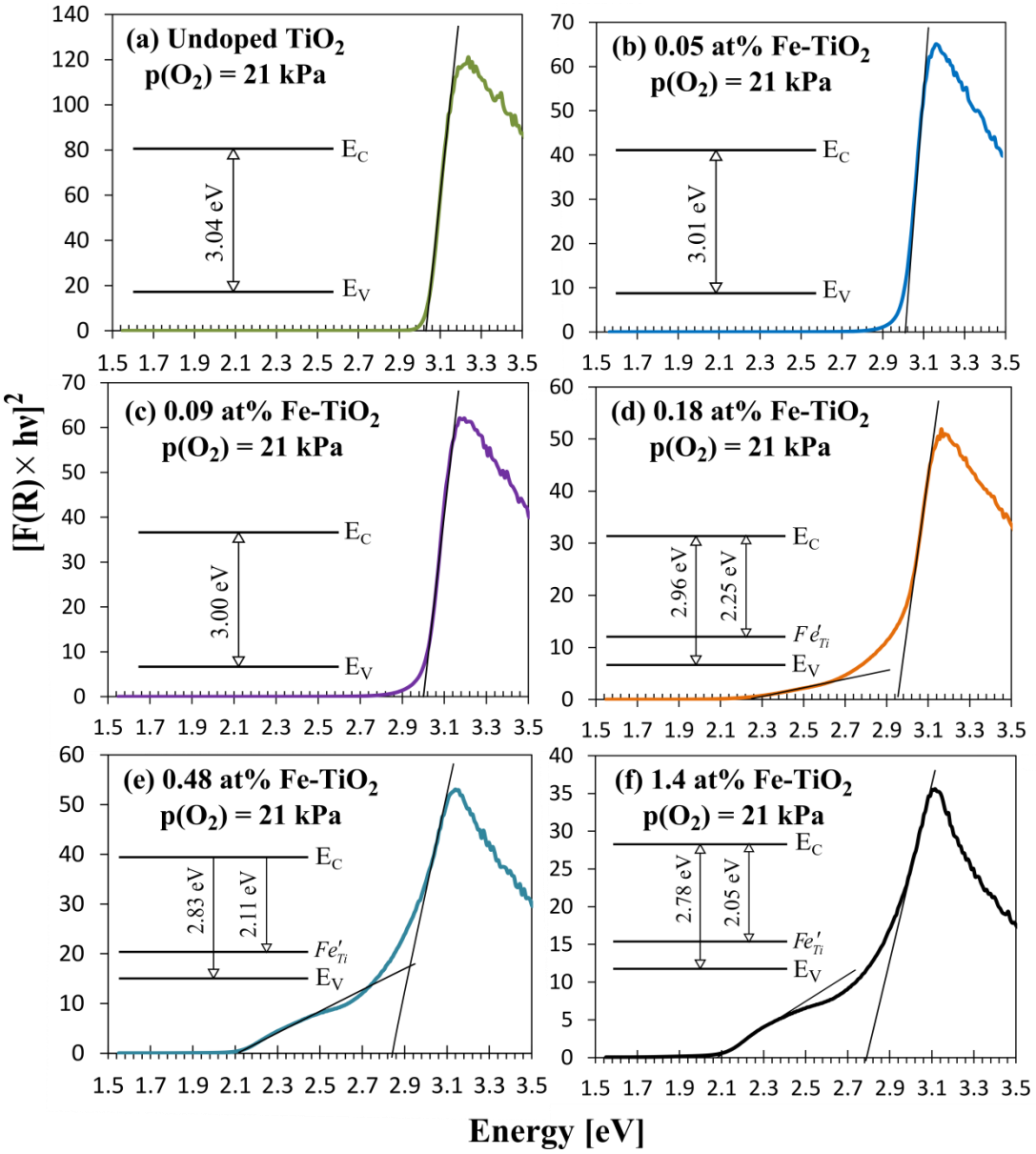

Figure 5-2: Plots of $[F(R)\times hv]^2$ *vs.* hv for the direct optical transition for Fe-doped TiO_2, involving iron concentration from 0.05 to 1.4 at%, annealed at 1373 K in artificial air [$p(O_2)$ = 21 kPa].

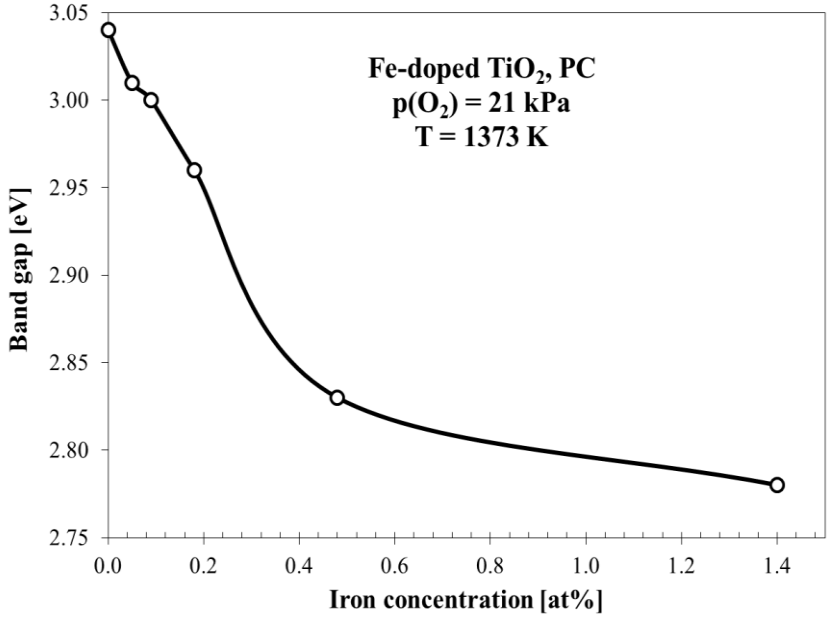

Figure 5-3: The effect of bulk iron concentration on the band gap of TiO_2, annealed at 1373 K for 24 hours in artificial air, $p(O_2)$ = 21 kPa.

The following points can be made based on the results in **Figure 5-2** and **Figure 5-3**.

- **Undoped TiO_2.** The band gap of TiO_2 was determined to be 3.04 eV which is very close to the reported data. The Tauc plot for undoped TiO_2 is shown in **Figure 5-2a**.
- **0.05 at% Fe-doped TiO_2**. As seen in **Figure 5-2b**, the absorption edge shifts towards the lower energy value and that results in the band gap of 3.01 eV.
- **0.09 at% Fe-doped TiO_2**. The reduction of the band gap was insignificant due to the small increase of iron concentration. As seen in **Figure 5-2c**, the absorption edge slightly shifted towards the lower energy level which corresponds to E_g = 3.0 eV.
- **0.18 at% Fe-doped TiO_2**. The absorption edge shifted towards the lower energy value and the band gap is 2.96 eV. As seen in **Figure 5-2d**, the new

energy level was formed as well which corresponds to Fe^{3+} in titanium sites, Fe'_{Ti}. The energy level, Fe'_{Ti} is 0.71 eV above the valence band of TiO_2.

- **0.48 at% Fe-doped TiO_2**. As seen in **Figure 5-2e**, the increase of iron concentration results in a reduction of the band gap to 2.83 eV.
- **1.40 at% Fe-doped TiO_2**. **Figure 5-2f** confirms the continuous band gap width decrease with the increasing iron concentration. The intermediate energy level, Fe'_{Ti} is 0.73 eV above the valence band of TiO_2. The band gap was determined to be 2.78 eV for Fe-doped TiO_2, containing 1.4 at% Fe.

5.1.2 Effect of oxygen activity

Figure 5-4 shows the reflectance spectra of pure and 0.18 at% Fe-doped TiO_2, annealed at 1273 K in different oxygen activities. The spectra obtained in pure oxygen [$p(O_2)$ = 100 kPa], argon [$p(O_2)$ = 10 Pa], and artificial air [$p(O_2)$ = 21 kPa] are very similar except the reflectance spectra for the specimen annealed in reducing condition [$p(O_2) = 10^{-12}$ Pa]. The annealing gas phase involves the argon-hydrogen mixture 99% and 1 %, respectively. The exact value of oxygen activity was imposed by temperature.

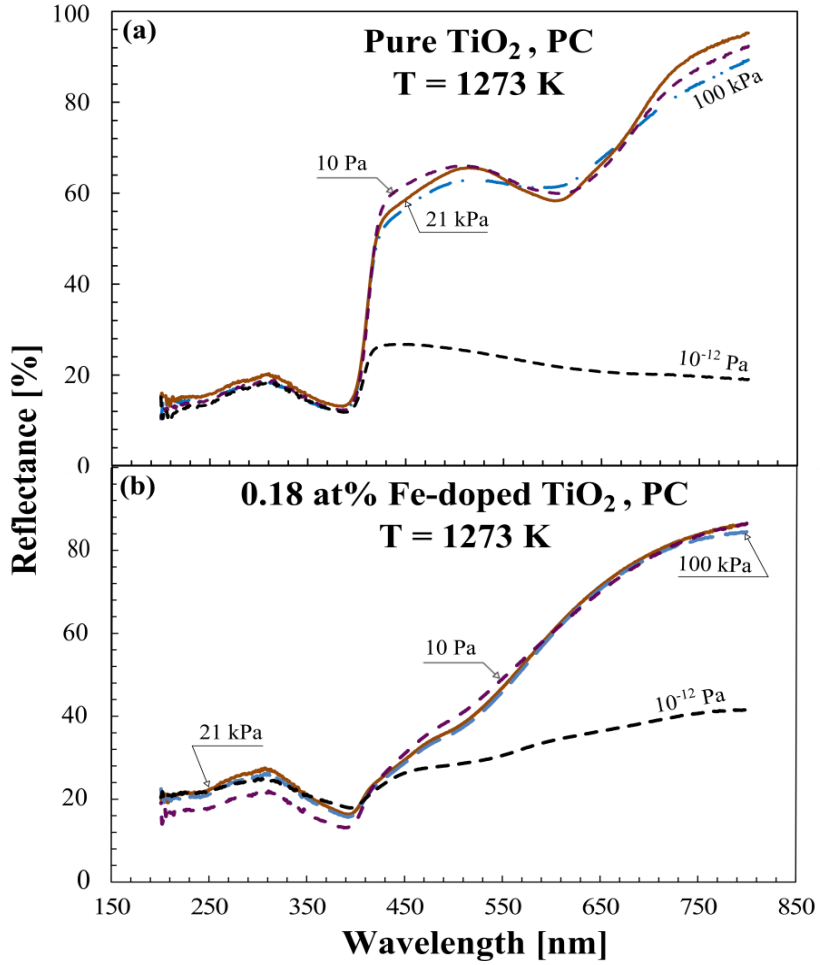

Figure 5-4: The reflectance spectra of pure (a) and 0.18 at% Fe-doped TiO_2 (b) annealed at 1273 K in different oxygen activities: pure O_2 (100 kPa), artificial air (21 kPa), Ar (10 Pa), and Ar/H_2 (1%) mixture (10^{-12} Pa).

The derived Tauc plots for pure and Fe-doped TiO_2 were drawn using the Kubelka-Munk function and are shown in **Figure 5-5**.

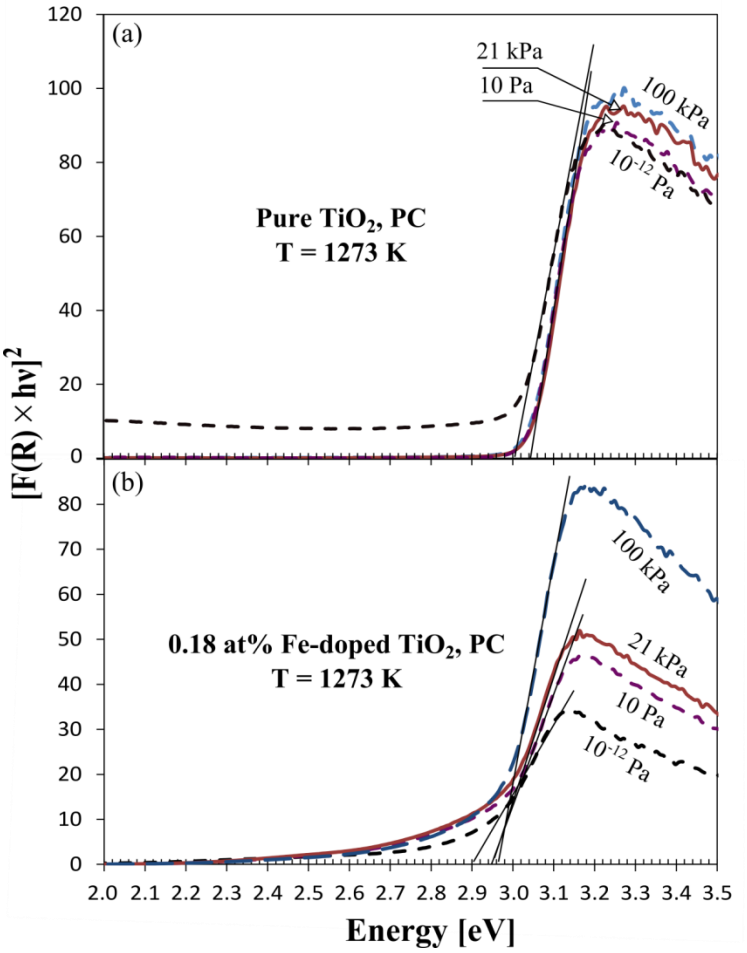

Figure 5-5: Plots of $[F(R)\times hv]^2$ vs. hv for the direct band gap transitions for pure TiO_2 (a) and 0.18 at% Fe-doped TiO_2 (b) annealed at 1273 K in different oxygen activities.

Figure 5-6 represents the effect of oxygen activity on the band gap of pure and Fe-doped TiO_2. As seen, altering oxygen activity had a minor effect on the band gap. The following points can be made based on these experimental results**:**

- **Pure TiO_2.** The band gap of 3.0 eV and 3.04 eV was determined after processing in reducing (10^{-12} Pa) and oxidising conditions (100 kPa), respectively. The decrease of the band gap in lower oxygen activity was due to the formation of oxygen vacancies. The recent study by Albetran et al., 2016 [1] also concluded that specimen annealed in reducing condition

exhibits a reduction of the band gap owing to the increased concentration of oxygen vacancies.

- **Fe-doped TiO_2 (0.18 at%).** The band gap value was determined to be 2.90 and 2.96 eV for the specimen annealed in reducing (10^{-12} Pa) and oxidising (100 kPa) conditions, respectively. The band gap difference of around 0.06 eV which is due to the increased concentration of oxygen vacancies.

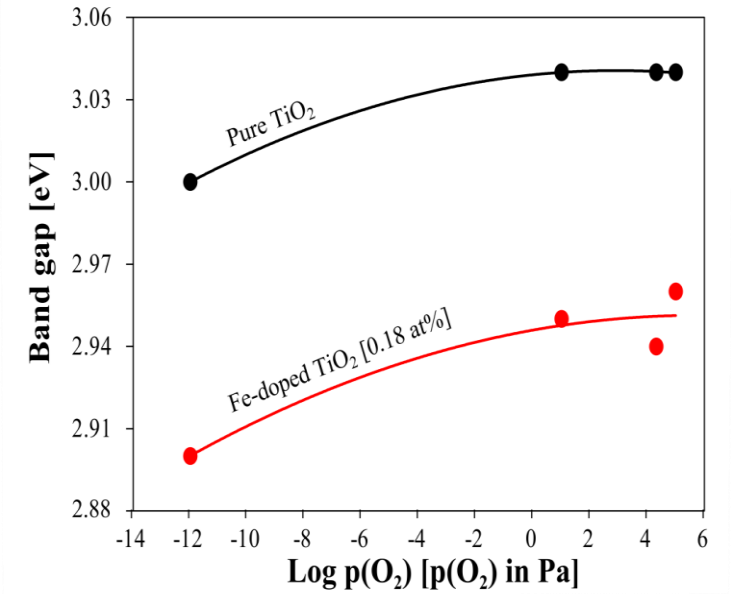

Figure 5-6: The effect of annealing at 1273 K in the gas phase of controlled oxygen activity on the band gap for pure and Fe-doped TiO_2, involving 0.18 at% Fe.

5.1.3 Theoretical model

The theoretical model, representing the effect of iron concentration on the electronic structure of TiO_2, is shown in **Figure 5-7.** The model is based on the experimental results (**Figure 5-2**) obtained in this study. As seen in **Figure 5-7**, the iron energy level splits into many (very closely spaced) energy levels with the increase of iron concentration, and ultimately, forms a narrow sub-band. Fe'_{Ti} level is around 0.79 eV and 0.73 eV above the valence band of TiO_2 for 0.18 at% and 1.4 at% Fe-doped

TiO_2, respectively. The edge of the valence band remains unchanged as the band is mostly composed of oxygen 2p orbitals and doping with iron does not change the position of its edge. On the other hand, mixing Ti 3d states with iron 3d and 4s states can, potentially, lower the edge of the conduction band.

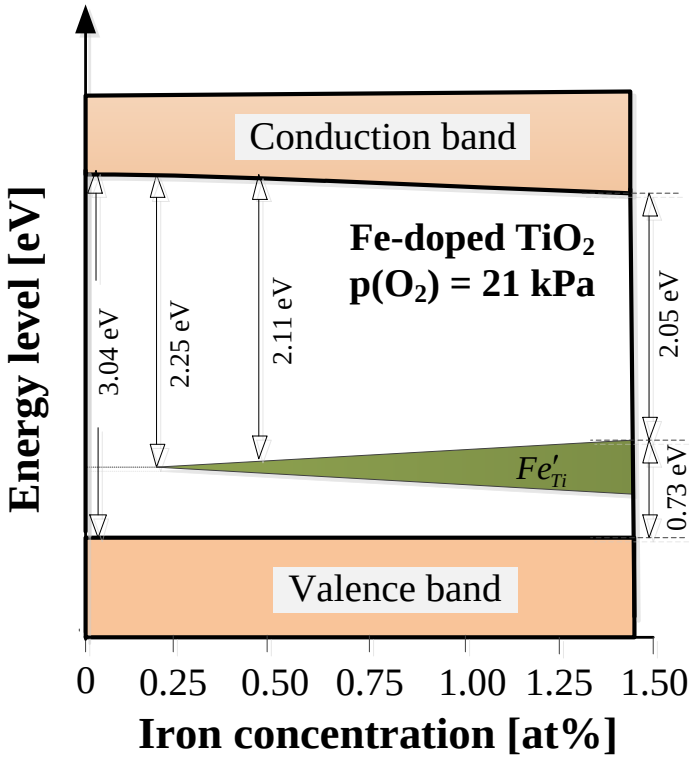

Figure 5-7: The schematic representation of the effect of bulk iron concentration on the electronic structure of TiO_2.

5.2 Effect of segregation on surface vs. bulk composition

5.2.1 Effect of iron concentration

5.2.1.1 X-ray photoelectron spectroscopy

The XPS spectra of the studied polycrystalline specimens of Fe-doped TiO_2 after annealing at 1373 K in artificial air are shown in **Figure 5-8.** Deconvolution of the spectra using casaXPS software [2] reveals that both Fe^{2+} and Fe^{3+} exist at the surface of Fe-doped TiO_2. However, Fe^{3+} is the predominant oxidation state.

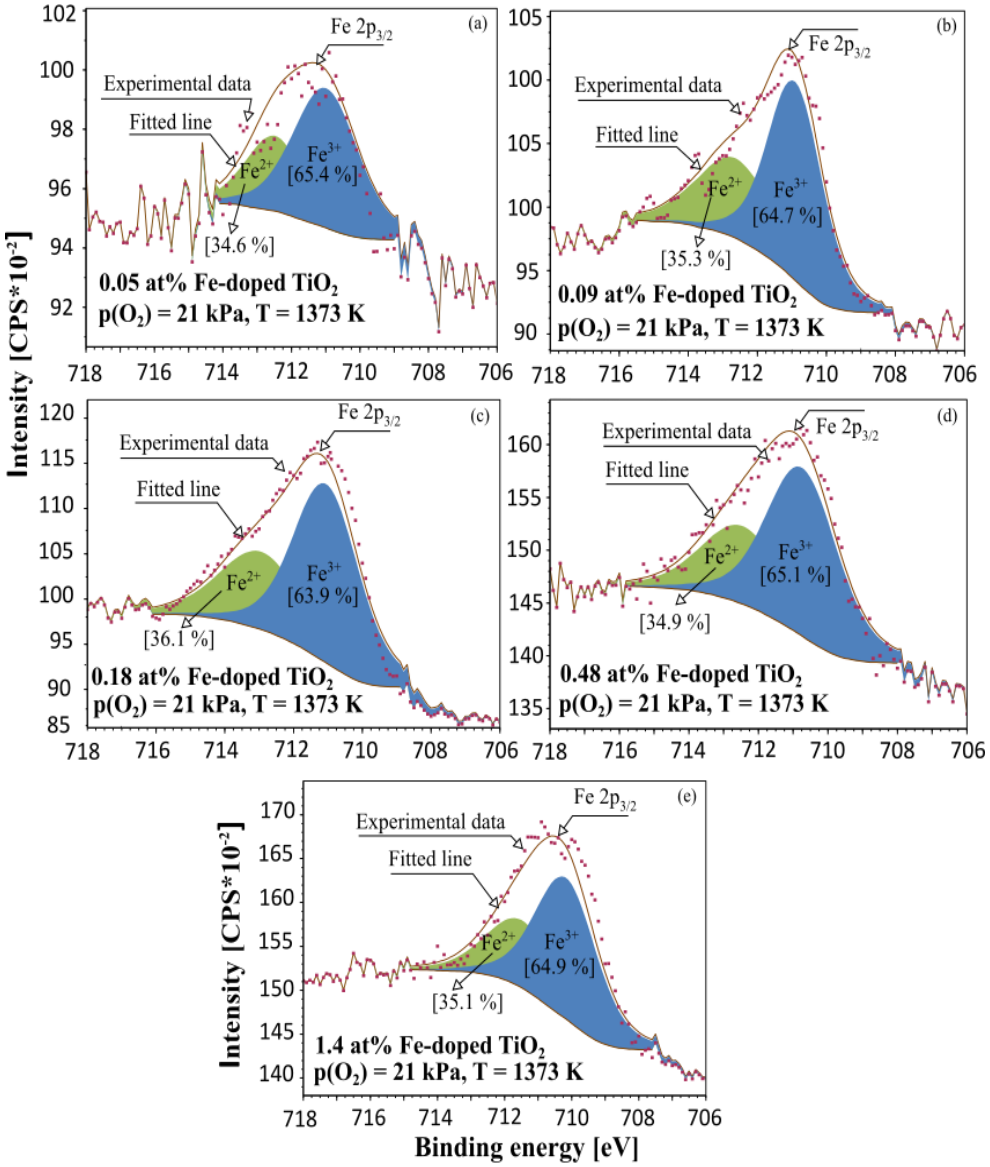

Figure 5-8: Fe2p-related spectra (intensity count per second vs. binding energy) for Fe-doped TiO_2, containing iron content from 0.05 to 1.4 at%, annealed at 1373 K in artificial air, $p(O_2)$ = 21 kPa. The de-convoluted spectra for both Fe^{2+} and Fe^{3+} species are marked by different shading intensity.

5.2.1.2 Secondary ion mass spectrometry

The results obtained from the SIMS analysis, which are shown in **Figure 5-9**, represent the depth profile of the intensity (counts/seconds) ratio of ^{56}Fe to ^{47}Ti for Fe-doped TiO_2, involving iron concentration from 0.05 at% to 1.4 at%. To avoid

surface charging, the samples were covered with a thin layer of gold. Therefore, the data obtained for the outermost surface layer of 12 nm thick are affected by gold. Consequently, the initial part of segregation-induced data for Fe-doped TiO_2, which corresponds to the gold layer and its immediate vicinity, was removed from further interpretations.

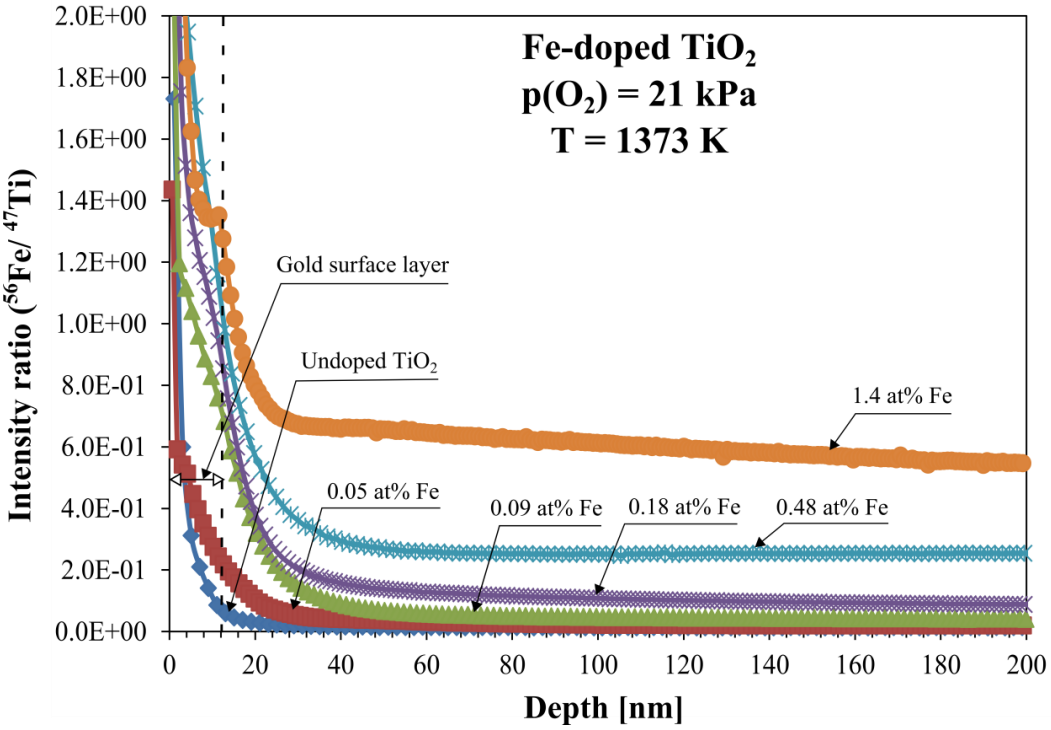

Figure 5-9: The SIMS spectra representing the effect of iron concentration in the bulk on its depth profile for Fe-doped TiO_2 (polycrystalline) annealed in artificial air at 1373 K for 24 hours.

5.2.1.3 Comparison of XPS and SIMS data

One of the aims of this thesis is the determination of the effect of annealing on iron segregation in Fe-doped TiO_2, including both single crystal and polycrystalline specimens. The annealing procedure was carried out in the gas phase of well-defined oxygen activity. The surface analysis of the specimens was performed using both secondary ion mass spectrometry, SIMS, as well as X-ray photoelectron spectroscopy, XPS.

The advantage of the SIMS technique is its high sensitivity and resolution, allowing analysis of the outermost layer approximately 1 nm thick, as represented in **Figure 5-10**.

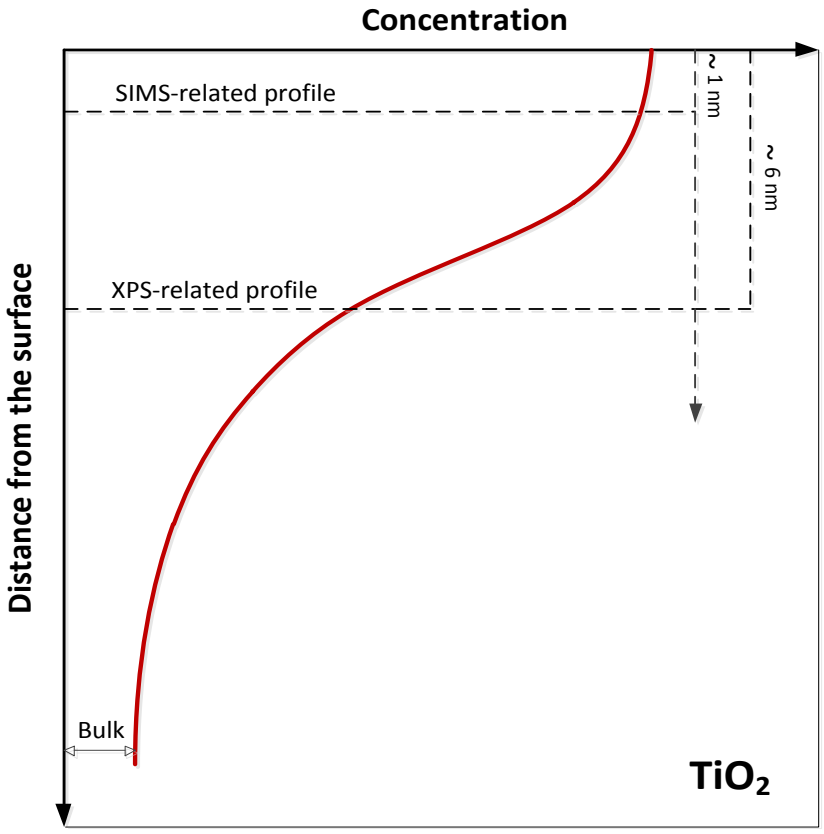

Figure 5-10: The schematic representation of the segregation-induced enrichment in selected lattice species showing the depths of surface analysis by SIMS and XPS methods.

Moreover, SIMS allows depth profiling, i.e. the determination of the chemical composition for the inner layers as well. The main disadvantage of SIMS is a complication in the quantitative chemical analysis that requires calibrations of the intensity profiles. In contrast, XPS can determine only the average composition of the surface layer. Its thickness depends on the applied incident angle, which is about 6 nm and 4 nm at the angles 90^{o} and 12^{o}, respectively [3]**.** However, it is possible to

obtain absolute concentrations of elements from the XPS data and the oxidation state of species present in the surface layer.

The data on the segregation of iron for polycrystalline Fe-doped TiO_2 are shown in **Figure 5-11**, including surface iron concentration (a), and iron enrichment factor (b). The surface analysis of Fe-doped TiO_2 indicates that the segregation-induced enrichment factor of Fe increases with the decrease of bulk Fe concentration. This effect indicates that the surface has a tendency to achieve a constant value of Fe, independently of the bulk Fe concentration.

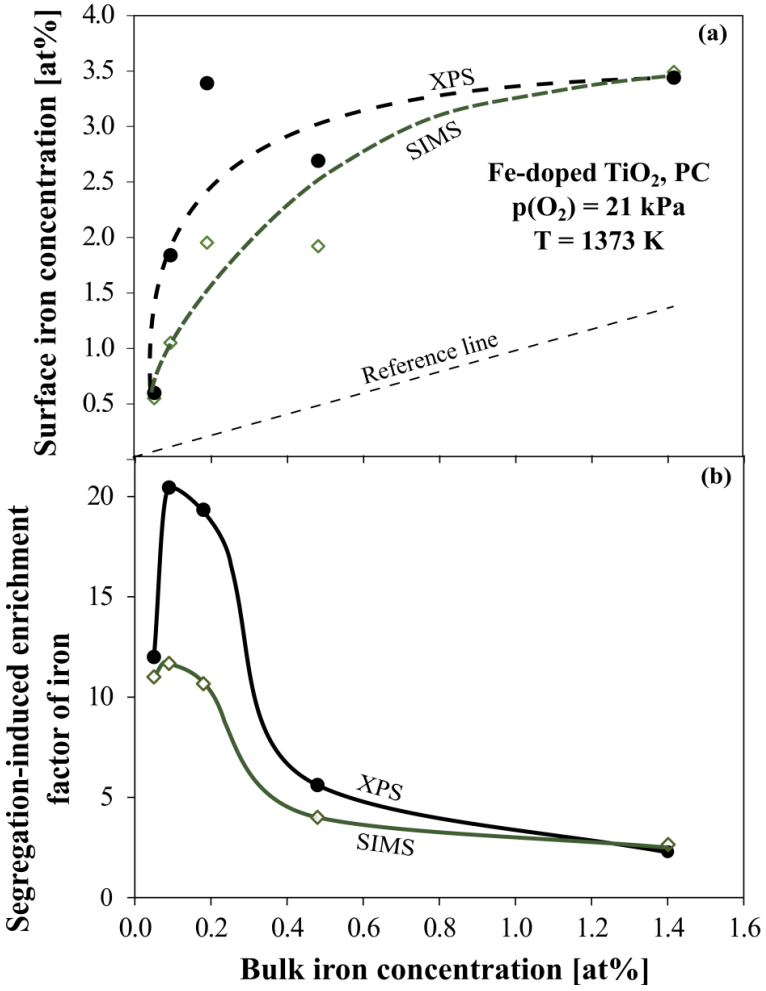

Figure 5-11: The segregation of iron for Fe-doped TiO_2 showing the surface vs. bulk concentration of iron (a), and the segregation-induced enrichment factor of iron (b) for polycrystalline specimens annealed at 1373 K for 24 hours in artificial air, $p(O_2)$ = 21 kPa, according to both SIMS and XPS surface analysis.

As seen, both XPS and SIMS attest iron segregation, however, the enrichment factor derived from the XPS measurements is slightly larger than that obtained from SIMS. The difference between these two results was strongly affected by the dissimilar resolution of both methods and by neglecting the outermost surface layer (12 nm) in the SIMS data. As a consequence, the first layer accounted by SIMS was 12 nm beneath the initial surface layer. The procedure of obtaining the absolute surface concentration of iron from the SIMS data is described later (**section 5.2.2.2 -** single crystal vs. polycrystal).

5.2.2 Effect of oxygen activity on the valence of iron

5.2.2.1 X-ray photoelectron spectroscopy

Figure 5-12 represents the effect of oxygen activity on oxidation state of iron at the surface of polycrystalline Fe-doped TiO_2 (0.18 at%). The XPS spectra were deconvoluted using casaXPS software [2]. As seen, the relative amount of surface iron species (Fe^{2+} and Fe^{3+}) changes with oxygen activity.

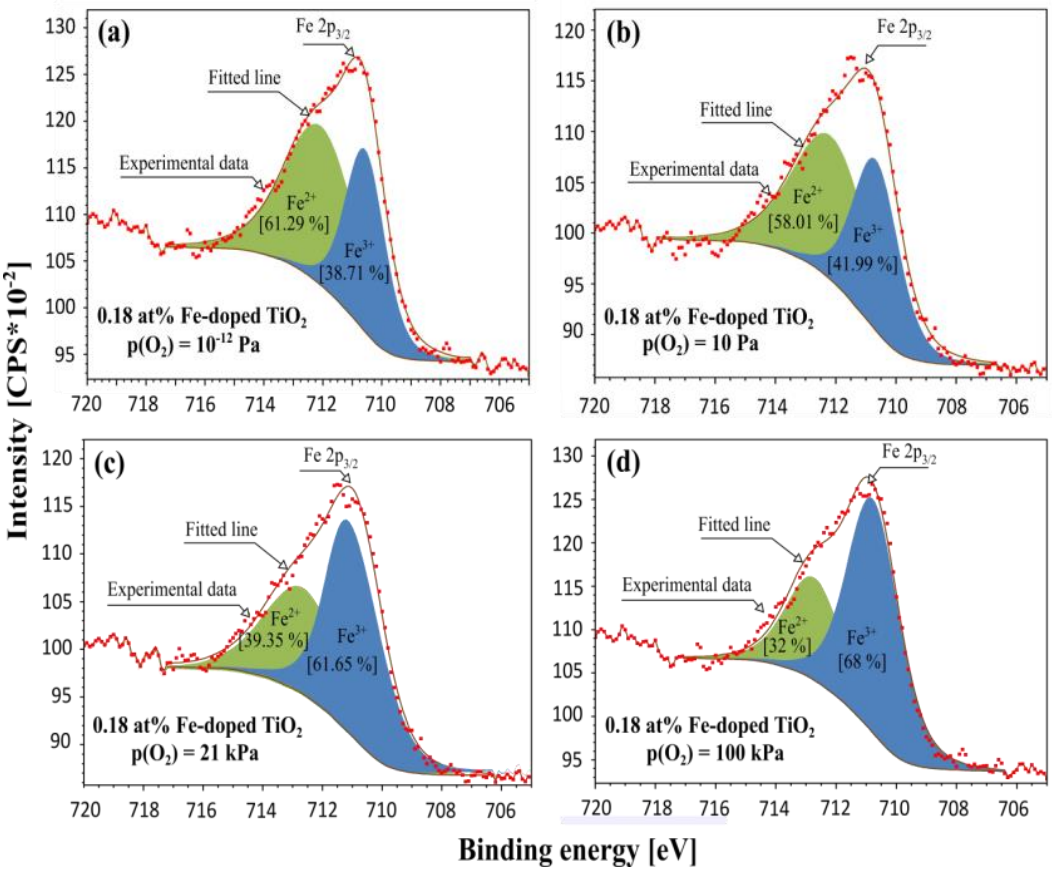

Figure 5-12: The effect of oxygen activity on Fe2p-related spectra (intensity count per second vs. binding energy) for 0.18 at% Fe-doped TiO_2 annealed at 1273 K. The de-convoluted spectra for both Fe^{2+} and Fe^{3+} species are marked by different shading intensity.

The effect of oxygen activity on the relative amount of surface iron ions of two different valences in Fe-doped TiO_2 is represented in **Figure 5-13**. As seen, the predominant oxidation state in reducing conditions is Fe^{2+}. The number of these species sharply decreases in oxidising conditions at $p(O_2)>10^2$ Pa. As also seen, the amount of tri-valent iron species in reducing conditions is approximately 37% and this quantity sharply increases to 65% at $p(O_2)>10^2$ Pa. The reason of the observed decrease in the concentration of Fe^{2+} ions consists in the resulting surface charge, namely the increase of $p(O_2)$ results in increased concentration of titanium vacancies leading to enhanced negative charge and, consequently, enhanced segregation of Fe^{3+} species.

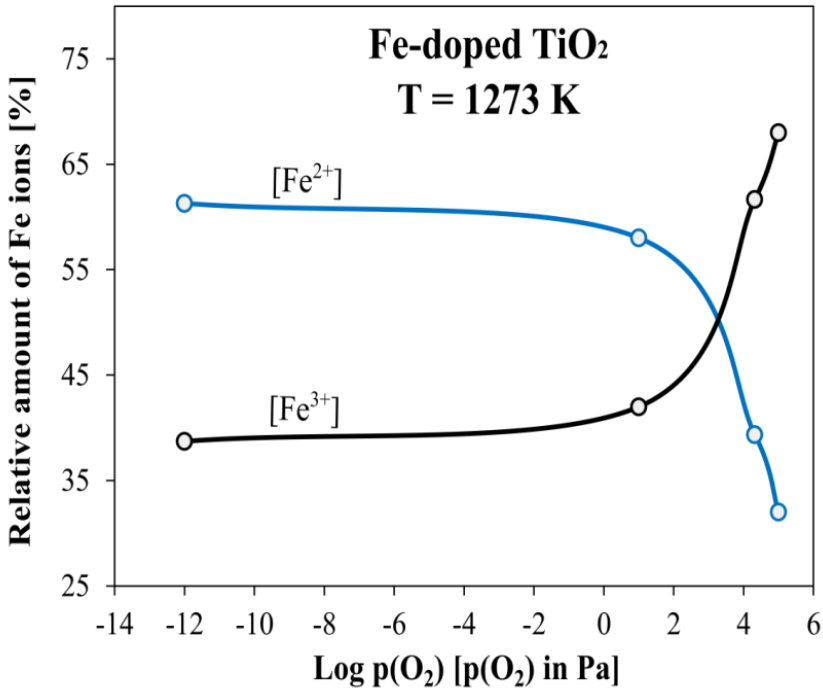

Figure 5-13: The effect of oxygen activity on the percentage of surface iron species in Fe-doped TiO_2 annealed at 1273 K for 24 hours in different oxygen activities.

5.2.2.2 Secondary Ion Mass Spectrometry

- ***Polycrystalline specimen***

The effect of oxygen activity on the segregation-induced depth profile of iron in polycrystalline Fe-doped TiO_2 is shown in **Figure 5-14**. The as-polished specimen is used here as the reference. As seen, the iron concentration at the surface increases with the decrease of oxygen activity. The data in **Figure 5-14** can be used for the calculation of segregation-related enrichment factor.

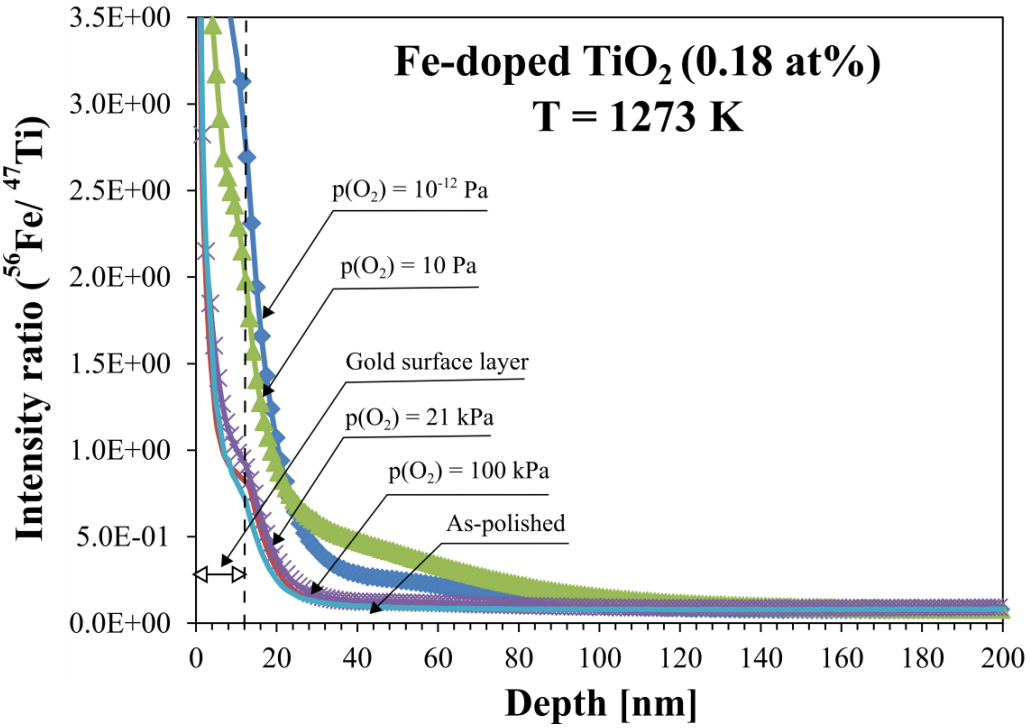

Figure 5-14: The SIMS spectra representing the effect of oxygen activity on depth profiles of Fe-doped TiO_2 (0.18 at%) annealed at 1273 K for 24 hours in different oxygen activities.

➢ *Single crystal specimen*

The effect of oxygen activity on the segregation-induced depth profile of iron in Fe-doped TiO_2 single crystal is shown in **Figure 5-15.** It is interesting to note that the surface concentration of iron for the as-polished specimen, which can be used here as a reference, is larger than that for the specimen annealed in pure oxygen [$p(O_2)$ = 100 kPa].

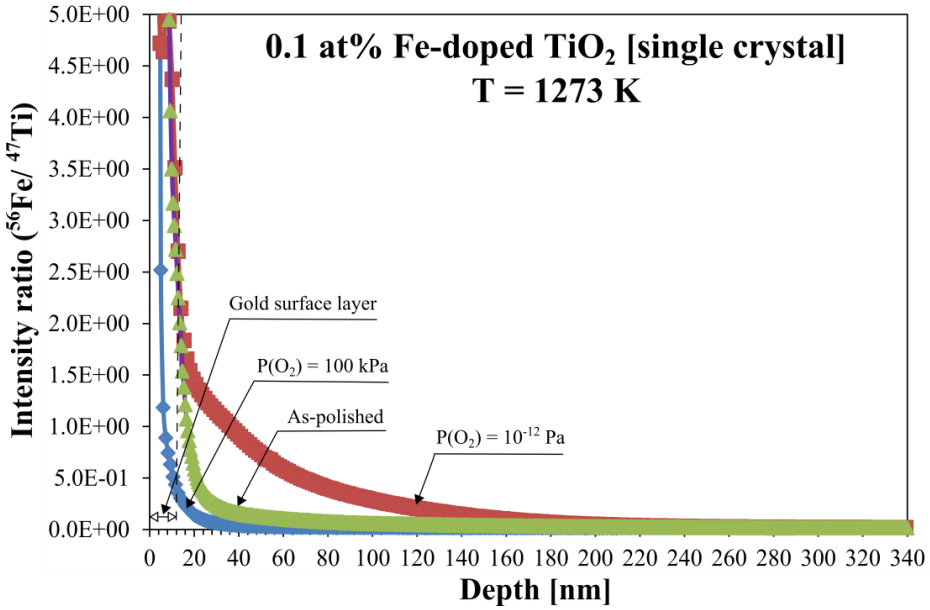

Figure 5-15: The SIMS spectra showing the effect of oxygen activity on segregation-induced depth profile of 0.1 at% Fe-doped TiO_2 annealed in the gas phase of different oxygen activities at 1273 K for 24 hours.

➢ *Single crystal vs. polycrystalline*

The combined results of surface vs. bulk concentration of iron for single crystal and the polycrystalline specimen of Fe-doped TiO_2 are shown in **Figure 5-16.** The figure was drawn based on the following:

- The first 12 nm thick layer is considered the gold affected layer and, therefore, the data measured for this layer was removed from any further interpretation.
- The enrichment factor (f = surface/bulk iron concentration) was determined by dividing the intensity ratio at the surface by that in the bulk. Iron bulk concentrations in polycrystalline specimens were determined by PIXE, as shown in **Table 4-1**. Using the obtained enrichment factors, surface iron concentrations were then calculated and they are represented by dot points on the graph.

- The dash lines represent the gradients of iron concentration along the distance (0 to 190 nm for polycrystalline specimen and 0 to 340 nm for single crystal specimen) and the solid lines below the dash lines represent the bulk iron concentrations.

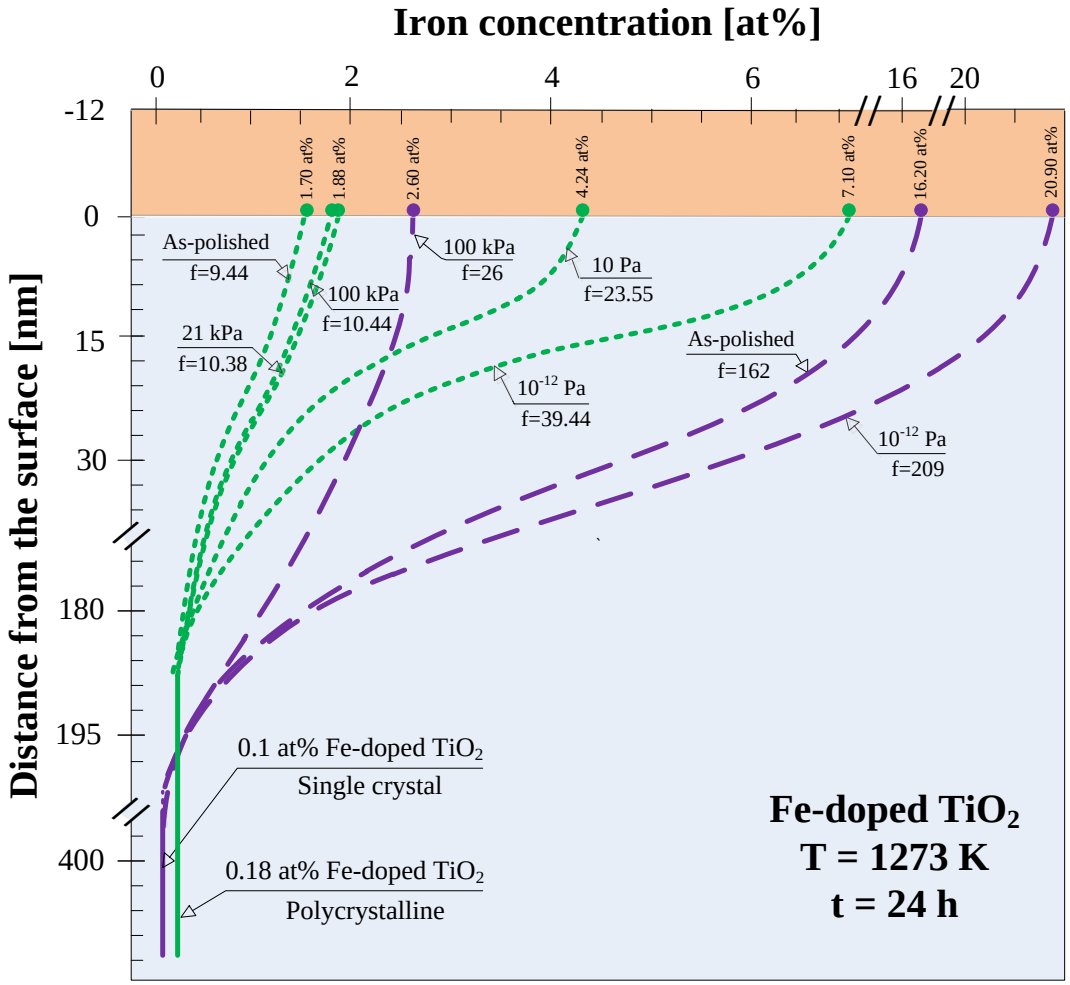

Figure 5-16: The SIMS-related segregation-induced depth profile for Fe-doped TiO_2 annealed at 1273 K for 24 hours in the gas phase of different oxygen activities. The bulk concentration of iron for polycrystalline specimen was determined by PIXE analysis.

The results from **Figure 5-16** on the segregation-induced enrichment factor of iron are summarised in **Figure 5-17**.

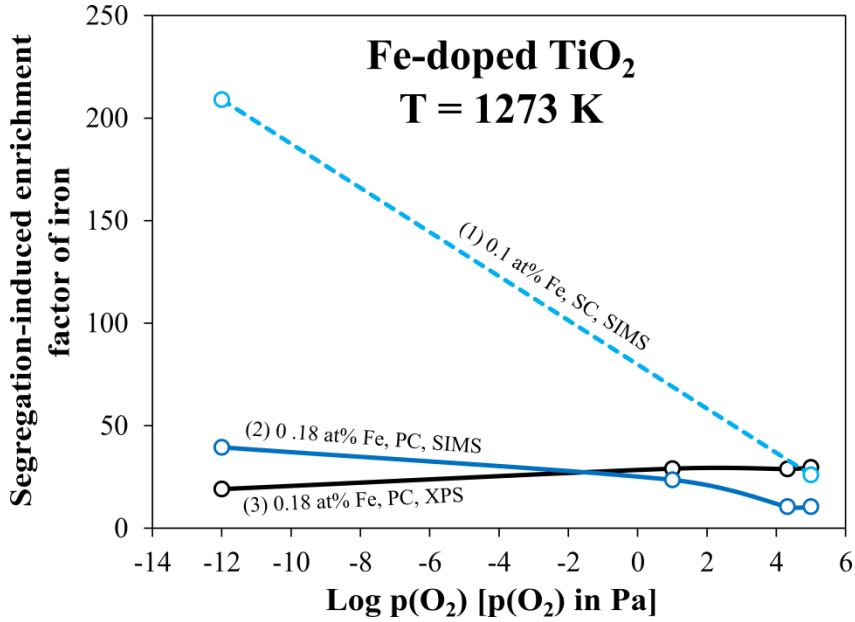

Figure 5-17: The effect of oxygen activity on the segregation-induced enrichment factor of iron for Fe-doped TiO_2 annealed at 1273 K for 24 hours in the gas phase of controlled oxygen activity for both single crystal and polycrystalline specimens.

The results in **Figure 5-16** and **Figure 5-17** allow the following points to be made:

- ***Polycrystalline specimen***
  - The increase of oxygen activity results in a decrease of the segregation-induced iron concentration (the related enrichment factor change from approximately 40 to 11).
  - The reference, an as-polished specimen, exhibits the iron enrichment level at the surface comparable to that for Fe-doped TiO_2 annealed in oxidising condition.
- ***Single crystal***
  - The decrease of oxygen activity results in an increase of the segregation-induced iron concentration and the related enrichment factor from approximately 26 to 209 in oxidising and reducing conditions,

respectively. Therefore, the related enrichment factors are larger from those for polycrystalline specimens by the factor of 2-5.

- The as-polished reference specimen exhibits the iron enrichment level of f = 162 that is comparable to that of Fe-doped TiO_2 SC annealed in reducing conditions.

Enrichment factors for the single crystal and polycrystalline specimens may be considered in terms of the related microstructures. The single crystal, which is free of grain boundaries, allows for the unobstructed transport of segregating species directly to the external surface. Therefore, the segregating iron species are extracted from the entire bulk phase. On the other hand, the species segregating towards the external surface of polycrystalline specimens are trapped by grain boundaries. As a result, the amount of iron reaching the external surface is reduced by the amount segregating to grain boundaries.

5.2.3 Theoretical model of segregation

The predominant driving forces of segregation in metal oxides include (i) the strain energy related to the mismatch of ionic radii between the segregating species and the host lattice species, and (ii) the electrostatic force.

5.2.3.1 Strain energy

The ionic radii of Fe^{3+}, Fe^{2+} and Ti^{4+} species are 0.64 nm, 0.77 nm and 0.60 nm, respectively [4]. The only mismatch that could contribute to the strain energy component originates from di-valent iron ions, while the strain energy component related to tri-valent iron ions can be ignored.

5.2.3.2 Electrostatic field

The electrostatic field, which is imposed by the electrically charged surface layer, promotes the migration of iron species that are electrically charged. The proposed model on the segregation of iron species in Fe-doped TiO_2 due to the gradient of electric field is represented in **Table 5-1**.

Table 5-1: The model representing the effect of oxygen activity on defect disorder of the surface layer and the bulk phase and the associated transport of the segregating iron species in Fe-doped TiO_2.

Conditions	Oxidising	Reducing
Surface layer	V_{Ti}'''', $Ti_{1-x}O_{2-y}$	$V_O^{\bullet\bullet}$, Ti_8O_{15}, H_4TiO_4
Surface charge	⊖	⊕
	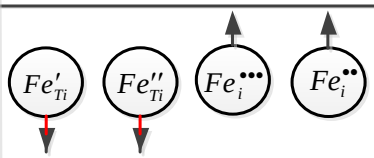	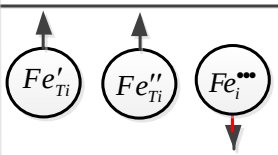
Bulk phase	$Fe_2O_3 + \frac{1}{2}O_2 \leftrightarrow 2Fe_{Ti}' + 2h^{\bullet} + 4O_O^x$ $FeO + \frac{1}{2}O_2 \leftrightarrow Fe_{Ti}'' + 2h^{\bullet} + 2O_O^x$ $2Fe_2O_3 \leftrightarrow 4Fe_i^{\bullet\bullet\bullet} + 3V_{Ti}'''' + 6O_O^x$ $Fe_2O_3 + \frac{1}{2}O_2 \leftrightarrow 2Fe_i^{\bullet\bullet\bullet} + 2V_{Ti}'''' + 2h^{\bullet} + 4O_O^x$ $FeO + \frac{1}{2}O_2 \leftrightarrow Fe_i^{\bullet\bullet} + V_{Ti}'''' + 2h^{\bullet} + 2O_O^x$	$Fe_2O_3 \leftrightarrow 2Fe_{Ti}' + V_O^{\bullet\bullet} + 3O_O^x$ $FeO \leftrightarrow Fe_{Ti}'' + V_O^{\bullet\bullet} + O_O^x$ $Fe_2O_3 \leftrightarrow 2Fe_i^{\bullet\bullet\bullet} + 6e' + \frac{3}{2}O_2$

The model considers both oxidising and reducing conditions. Annealing TiO_2 in oxidising conditions results in imposition of a negative surface charge that is related to the presence of immobile titanium vacancies, which are the predominant species at the surface, when oxygen activity in the gas phase is high [5]. The resulting electrostatic field is the driving force for segregation of negatively charged iron species from the surface to the bulk phase and positively charged iron species from

the bulk to the surface. On the other hand, annealing TiO_2 in reducing conditions results in imposition of positive surface charge that is associated with oxygen vacancies. The resulting electrostatic field is the driving force for segregation of negatively charged iron species from the bulk to the surface. A Ti_8O_5 type surface structure can also form at the surface in reducing condition. An H_4TiO_4 type structure may also appear at the surface as low oxygen activity in the gas phase was achieved by the means of Ar/H_2 atmosphere.

Taking into account the above considerations, the segregation of iron in reducing conditions may be pondered in terms of both the strain energy contribution and the electrostatic contribution. At low oxygen activity, $Fe^{2+}$is the preferred oxidation state of iron, hence, the strain energy increases due to the larger ionic radius of these ions. On the other hand, the predominant driving force of segregation in oxidising conditions is the electrostatic contribution.

5.3 Effect of iron concentration on photocatalytic performance of TiO_2

5.3.1 Photocatalytic degradation of MB

Figure 5-18 depicts the photocatalytic degradation of methylene blue (MB) with reaction time using 0.09 at% Fe-doped TiO_2 photocatalyst. Absorbance spectra of MB, obtained in the presence of other photocatalytic specimens, are similar in shape. The decreasing in the height of the absorbance peak determined after soaking in the dark is related to the adsorption of MB on the surface of the catalyst. As seen in **Figure 5-18,** the 0.09 at% Fe-doped TiO_2 ceramic samples can absorb around 30% of MB from the solution into the open pores within 2 hours. The continuous decrease

of the MB absorption peaks over the reaction time clearly indicates the progress of MB degradation in the solution.

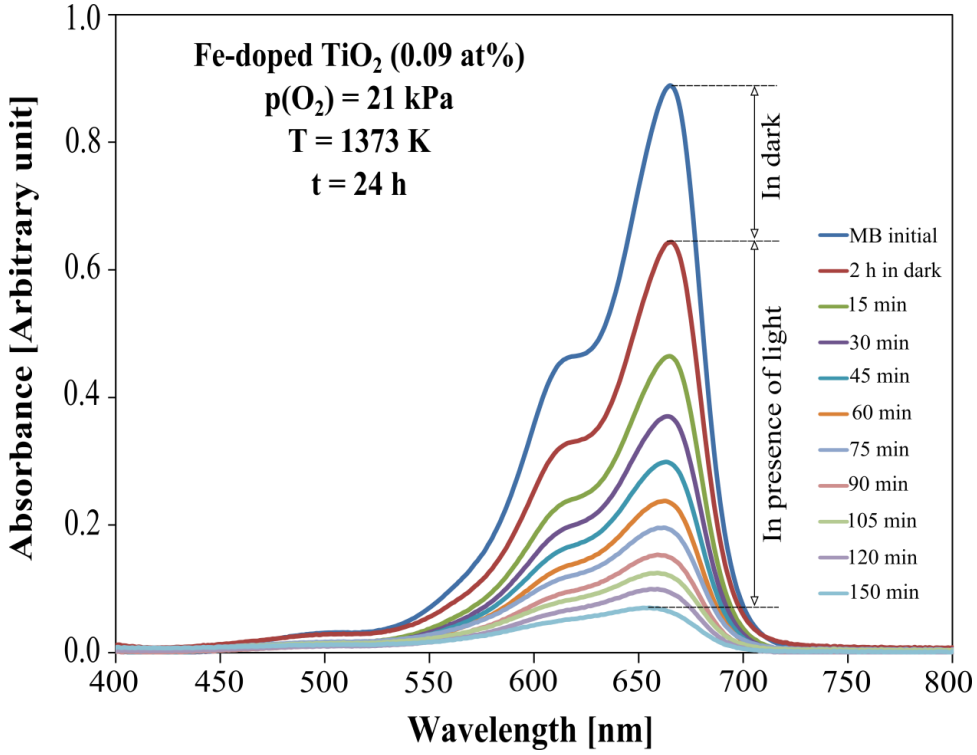

Figure 5-18: The UV–Vis absorption spectra of methylene blue (MB) with wavelength corresponding to the decomposition of MB after different reaction times for Fe-doped TiO_2, containing 0.09 at% Fe, specimen annealed at 1373 K for 24 hours in artificial air, $p(O_2)$ = 21 kPa. The absorption peaks decreases with the reaction time.

Figure 5-19 represents the effect of different iron concentration in TiO_2 on the degradation of MB. As seen, the degradation of MB progresses with the illumination time. Note that the fastest decrease of MB concentration was obtained for the photocatalyst containing 0.09 at% iron in TiO_2, after annealing in oxidising condition, $p(O_2)$ = 21 kPa. The photocatalytic activity towards MB decomposition decreases with increased iron concentration in TiO_2 (beyond 0.09 at% Fe). These results contradict with the previous studies claiming that iron doping into TiO_2 always results in a decrease of photocatalytic activity [6-8]. Amongst samples

annealed in reducing condition (10^{-10} Pa of oxygen activity), the fastest MB decomposition was observed for undoped TiO_2, therefore, incorporation of iron into TiO_2 at low oxygen activity does not improve its photocatalytic activity.

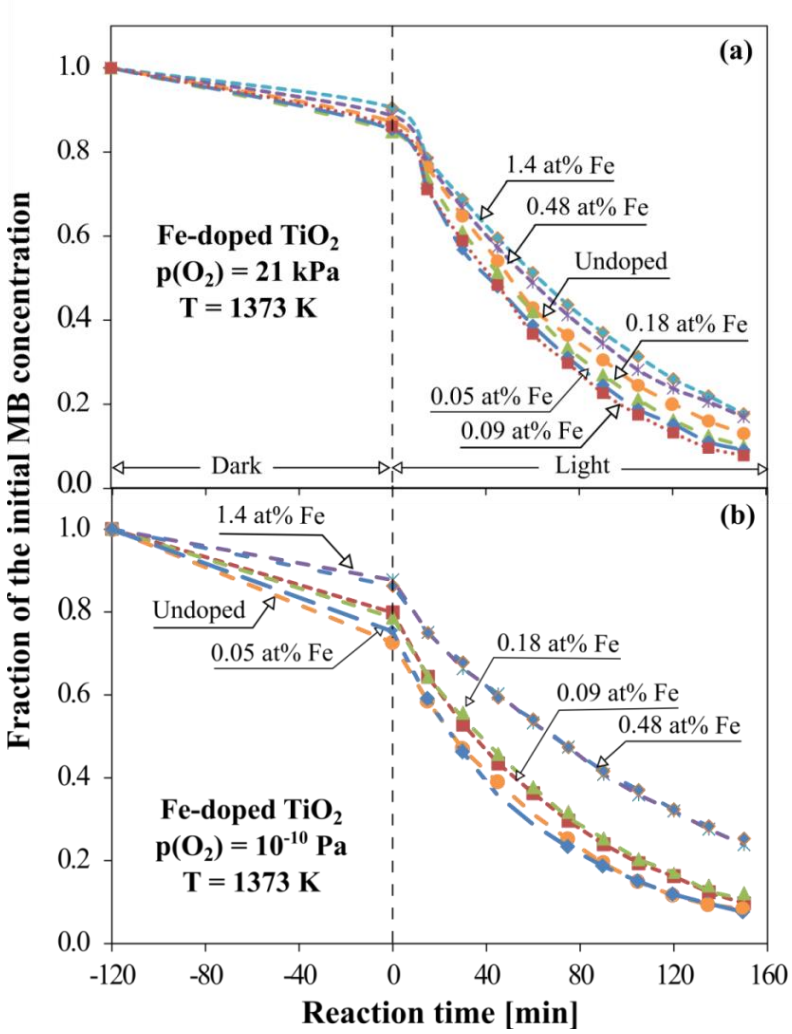

Figure 5-19: The photocatalytic decomposition of MB for Fe-doped TiO_2 as a function of reaction time. The specimens were annealed at 1373 K for 24 hours in two different oxygen activities: 21 kPa (a) and 10^{-10} Pa (b).

Plotting $ln\ (C_o/C_t)$ versus reaction time gives the apparent rate constant, k, which is shown in **Figure 5-20**. The rate constants of the MB decomposition reaction for Fe-doped TiO_2, involving iron concentration from 0.05 to 1.4 at%, are shown in **Table 5-2**.

Table 5-2: The effect of iron concentration on the photocatalytic activity of Fe-doped TiO_2 in terms of rate constant.

Fe-doped TiO_2	Fe [at%]					
	Undoped	**0.05**	**0.09**	**0.18**	**0.48**	**1.4**
Rate constant, $k \times 10^3$ [min^{-1}]	12.2	14.5	15.5	13.5	10.8	10.3

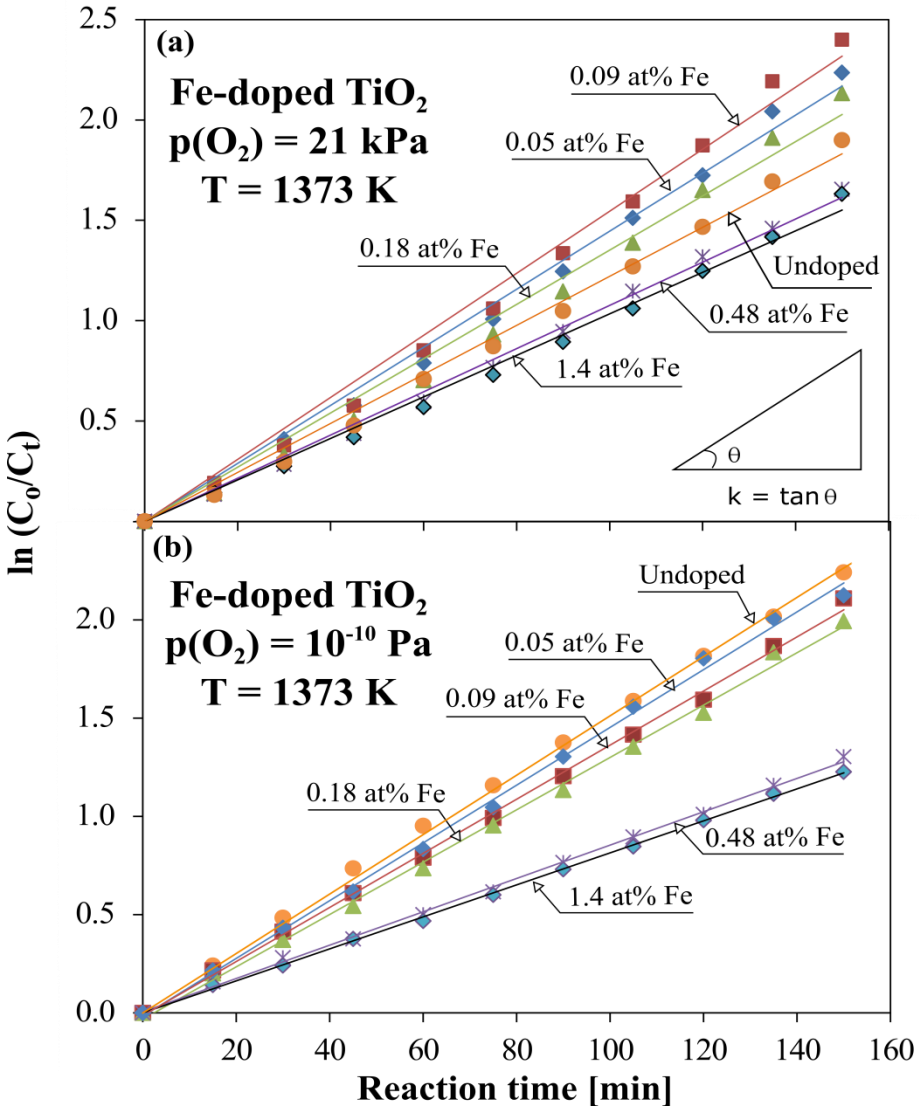

Figure 5-20: The changes of *ln* (C_o/C_t) with reaction time for the specimens of Fe-doped TiO_2, involving iron concentration from 0.05 to 1.4 at%, annealed at 1373 K in two different oxygen activities: (a) 21 kPa and (b)10^{-10} Pa. The inside image indicates the procedure of rate constant (k) determination.

Figure 5-21 compares the effects of iron concentration on the photocatalytic activity (a) and band gap (b) of TiO_2. As seen, the incorporation of iron leads to a reduction of the band gap of TiO_2. However, it has been observed that the photocatalytic performance increases only up to a certain iron concentration (0.09 at%) incorporated in oxidising condition (21 kPa). This coincides with the segregation-induced iron enrichment factor which assumes a maximum value at the same concentration of iron (**Figure 5-11**). On the other hand, incorporation of iron into host lattice in reducing condition (10^{-10} Pa) results in a decrease of photocatalytic activity, despite a significant reduction of the band gap.

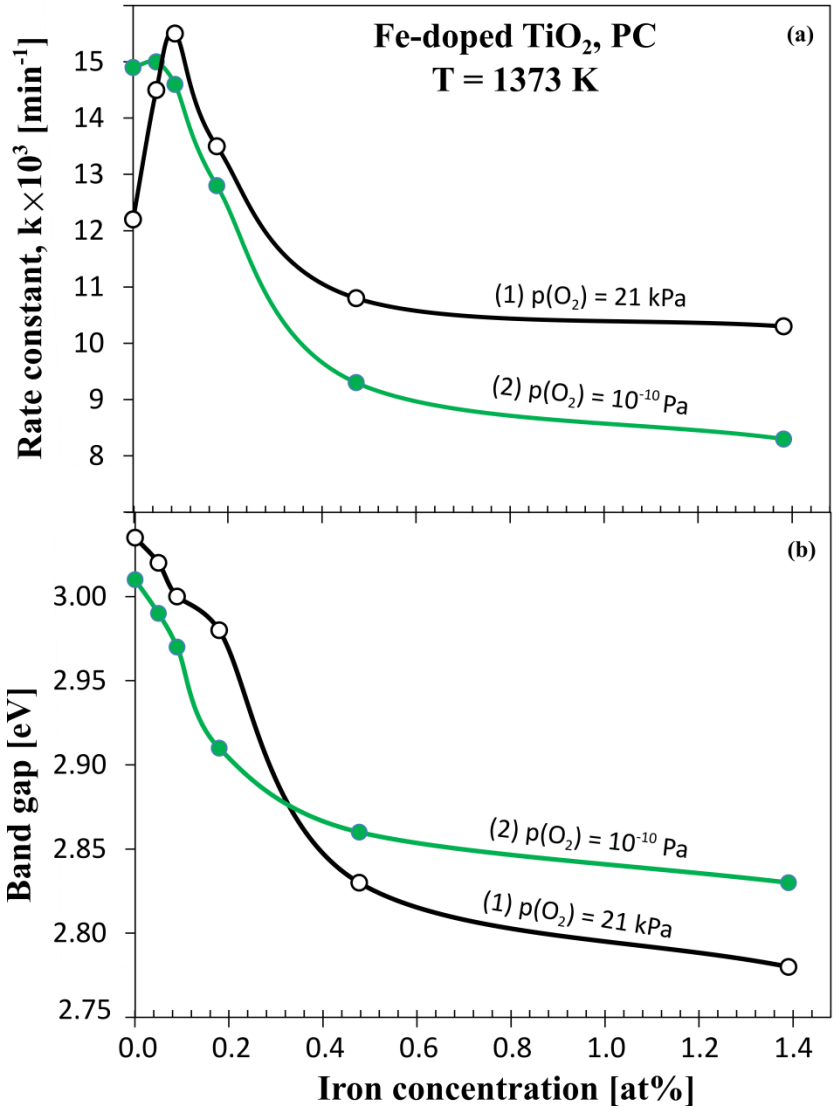

Figure 5-21: The effect of iron concentration on the photocatalytic activity (a) and band gap (b) of TiO_2 annealed at 1373 K in two different oxygen activities: 21 kPa and 10^{-10} Pa.

In oxidising condition, $p(O_2)$ = 21 kPa, the effect of iron concentration on the photocatalytic performance of TiO_2 cannot be explained by considering only the band gap narrowing (**Figure 5-21**). Rather, the effect must be discussed in terms of KPPs, comprising surface active sites, Fermi level, and charge transport.

- ***Concentration of surface active sites.*** Titanium vacancies which are generated during the incorporation of tri-valent iron into interstitial positions

and iron ions in Ti position with negative effective charge act as surface active sites for water oxidation in Fe-doped TiO_2, with the subsequent formation of active radicals. At a higher iron concentration (beyond 0.09 at%), the photocatalytic activity decreases due to the formation of surface structure like Fe_2TiO_5 [9] and defect complexes.

- ***Band gap.*** Incorporation of iron results in a reduction of the band gap of Fe-doped TiO_2 from 3.04 for undoped TiO_2 to 2.78 eV. However, photocatalytic activity does not follow this trend, which indicates that other predominant effects affecting the performance (discussed in **section 2.5**).
- ***Fermi level.*** Incorporation of iron into titanium sites and subsequent ionisation of these acceptor states shifts the Fermi level towards the valence band of TiO_2. That increases the anodic behaviour which is required for the oxidation reaction.
- ***Charge transport.*** High charge transport is essential for enhancing the photocatalytic activity. However, both the concentration and the mobility of charge carriers in Fe-doped TiO_2 decrease with the increase of iron concentration. Consequently, this property has a negative impact on photocatalytic activity.

In reducing condition, $p(O_2) = 10^{-10}$ Pa, different incorporation mechanism of iron into host lattice results in a decrease of photocatalytic activity as it shifts the Fermi level towards the conduction band leading to more cathodic behaviour. Additionally, due to the increased concentration of oxygen vacancies the concentration of titanium vacancies must decrease to preserve the Schottky equilibrium. Consequently, the

numbers of active sites for water oxidation are reduced and photocatalytic performance is poorer.

5.3.2 Theoretical model on surface reaction mechanism

Figure 5-22 shows the graphical representation of mechanism of Fe-doped TiO_2 surface reaction with water.

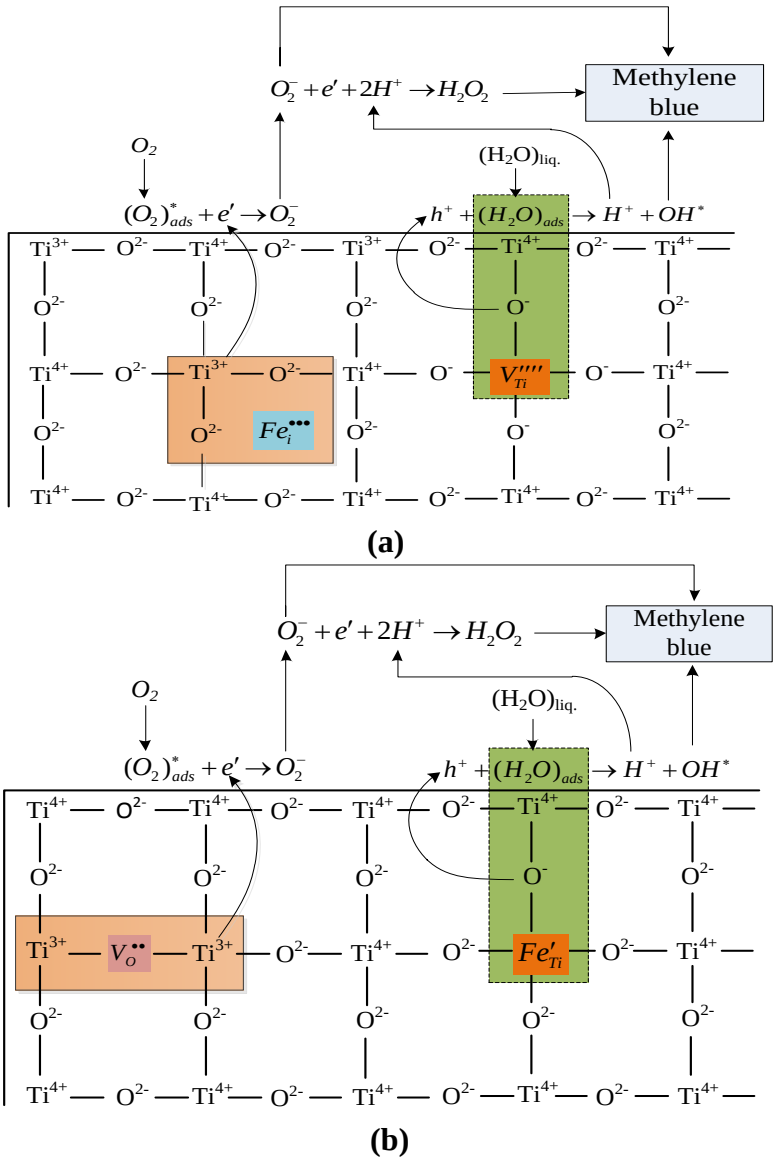

Figure 5-22: Proposed surface reaction mechanism of Fe-doped TiO_2 with water when titanium vacancies (a) and tri-valent iron substituted in Ti position (b) form within the surface layer.

As seen, the adsorption of water molecules on the negative-type defects, such as titanium vacancies (a), and tri-valent iron in Ti position (b) results in formation of an active complex and the removal of electrons from water. In other words, an electron hole reacts with water molecule and generates a hydroxyl radical which subsequently oxidises MB. Concurrently, the surface adsorbed oxygen molecule reacts with an electron and forms a superoxide anion, which also participates in the oxidation of MB.

Figure 5-23 shows the graphical representation of the example of associated defects in Fe-doped TiO_2 which could form at higher iron concentrations (beyond 0.09 at% Fe). These defects do not take part in any photocatalytic reactions due to the electrical neutrality of the complexes.

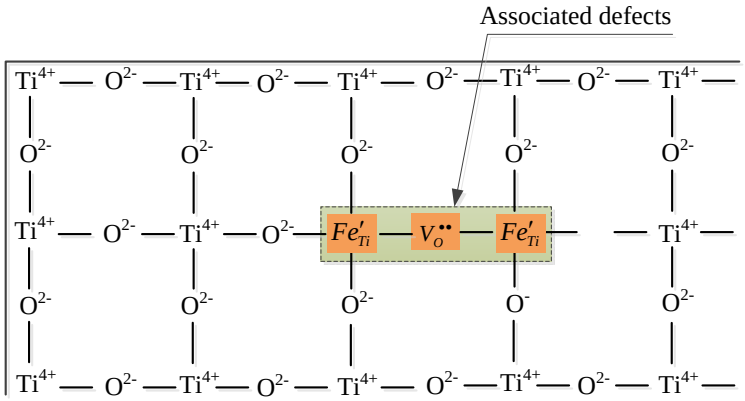

Figure 5-23: The formation of defect complex in Fe-doped TiO_2 at higher iron concentration (beyond 0.09 at% Fe).

5.3.3 Schematic representation of the effect of iron concentration on photocatalytic activity of TiO_2

Figure 5-24 schematically represents the effect of iron concentration on the photocatalytic activity of TiO_2. **Figure 5-24** is divided into two parts: regime-I and regime-II.

Regime-I: Photocatalytic activity increases with the incorporation of iron (up to 0.09 at%). It has been reported that both divalent and trivalent iron oxidation states exist at the surface of Fe-doped TiO_2 when the sample was treated in oxidising conditions [10]. However, in such a case, Fe^{3+} is the predominant oxidation state at the surface of the Fe-doped TiO_2 (confirmed by XPS data, **Figure 5-13**). Both titanium vacancies and iron ions in titanium positions can act as surface active sites for water oxidation and their population increases with the iron concentration, enhancing photocatalytic activity.

Regime-II: As seen in **Figure 5-24**, there is a critical concentration beyond which photocatalytic activity decreases with the addition of more iron (beyond 0.09 at%). The plausible origin of this effect is the formation of a defect complex that can be formed according to the reaction:

$$2Fe'_{Ti} + V_O^{\bullet\bullet} \rightarrow \left\{(Fe'_{Ti})_2 V_O^{\bullet\bullet})\right\}^x \qquad \textbf{(5-1)}$$

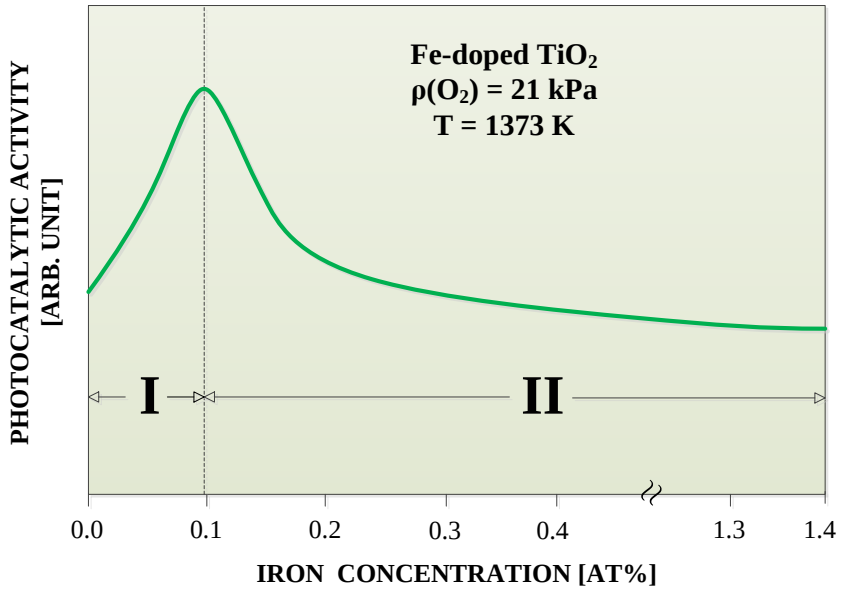

Figure 5-24: The schematic representation of the effect of bulk iron concentration on photocatalytic activity of TiO_2.

5.4 Effect of oxygen activity on photocatalytic activity of TiO_2

5.4.1 Photocatalytic oxidation of MB

Figure 5-25 depicts the changes in the absorbance spectra of the MB solution with the reaction time for Fe-doped TiO_2 (0.18 at%) specimen annealed in 100 kPa of oxygen activity. As seen in this figure, around 28% of MB was absorbed inside open pores of the solid catalyst, when the catalyst and solution were placed in darkness for 2 hours. The image within **Figure 5-25** shows the changes in appearance of the solution. More than 92% of MB was degraded after 150 minutes of reaction time.

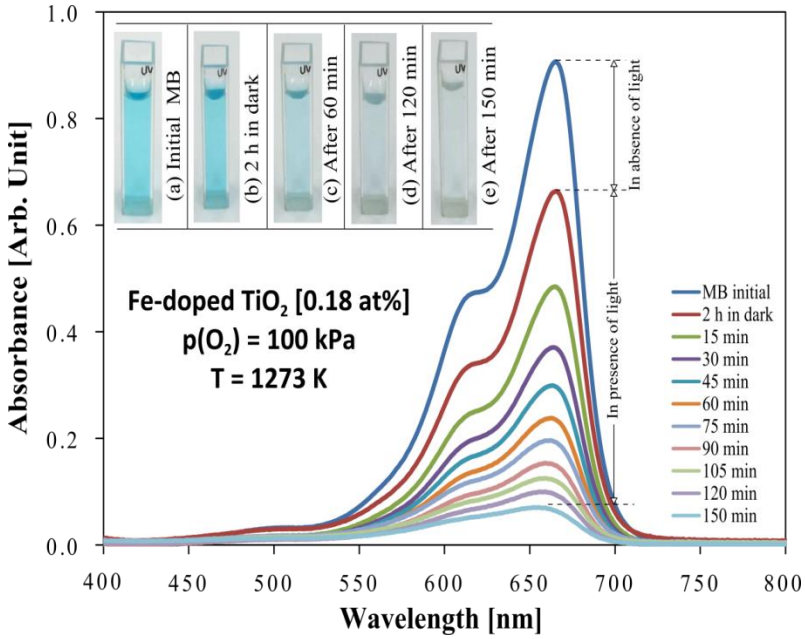

Figure 5-25: The absorbance spectra of MB solution after several irradiation times, demonstrating the photocatalytic decomposition of MB on 0.18 at% Fe-doped TiO_2 photocatalyst annealed in pure oxygen at 1273 K for 24 hours. The inside images indicate (a) initial MB solution; (b) after 120 min. in dark; (c) after 60 min. irradiation; (d) after 120 min. irradiation, and (e) after 150 min. irradiation.

Using the height of the MB absorbance peak as a measure of its concentration in the solution, **Figure 5-26** was constructed, taking into account the data obtained for photocatalysts annealed in different oxygen activities. Plotting $ln\ (C_0/C_t)$ versus

reaction time provides the apparent rate constant, determined using equation (**4-5**) and shown in **Table 5-3**.

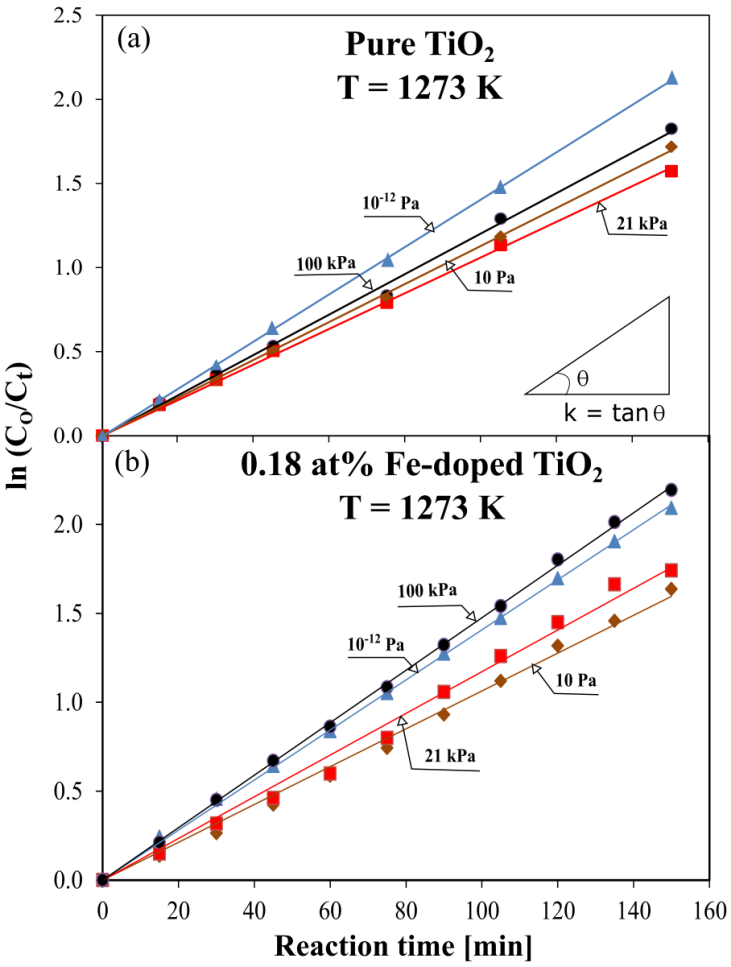

Figure 5-26: The changes of *ln* (C_o/C_t) for pure (a), and 0.18 at% Fe-doped TiO_2 (b) as a function of reaction time for the specimens annealed at 1273 K in the gas phase of different oxygen activities.

Table 5-3: The effect of oxygen activity on the photocatalytic activity of pure and Fe-doped TiO_2 (0.18 at%) in terms of rate constant.

#	Rate constant, $k \times 10^3$ [min^{-1}]			
	10^{-12} Pa	**10 Pa**	**21 kPa**	**100 kPa**
Pure TiO_2	14.1	11.3	10.6	12
0.18 at% Fe-doped TiO_2	14.0	11.3	10.6	14.8

Figure 5-27 represents the effect of oxygen activity on the photocatalytic activity (a), and band gap (b) of pure and 0.18 at% Fe-doped TiO_2. As seen, oxygen activity has a negligible effect on the band gap and a rather, substantial effect on photocatalytic performance. As seen, in the case of Fe-doped TiO_2 the highest rate of MB decomposition was obtained for the specimen annealed in pure oxygen followed by the Ar/H_2 mixture, artificial air, and argon. The results in **Figure 5-27** can be summarised as follows:

- ***Pure TiO_2.*** The maximum and minimum of photocatalytic activity was observed for samples annealed at 10^{-12} Pa and 21 kPa of oxygen activity, respectively. The increased concentration of electrons in reducing condition (10^{-12} Pa) is responsible for enhancing photocatalytic activity due to higher charge transport. On the other hand, the minimum of photocatalytic activity at $p(O_2)$ = 21 kPa can be attributed to the very low concentration of charge carriers in the vicinity of the n-p transition, which can be confirmed by electrical conductivity data, as shown in **Figure 3-2**.
- ***Fe-doped TiO_2.*** The maximum and minimum of photocatalytic activity occurred for the sample annealed at 100 kPa and 10 Pa, respectively. The increased population of surface active sites, titanium vacancies, play a major role in enhancing photocatalytic activity for the specimen processed at 100 kPa of oxygen activity. As the n-p transition point shifts towards the lower oxygen activity owing to the incorporation of iron into TiO_2, the corresponding drop in charge carrier concentration also shifts. As a result, the sample equilibrated in argon [$p(O_2)$ = 10 Pa] displays the lowest photocatalytic activity.

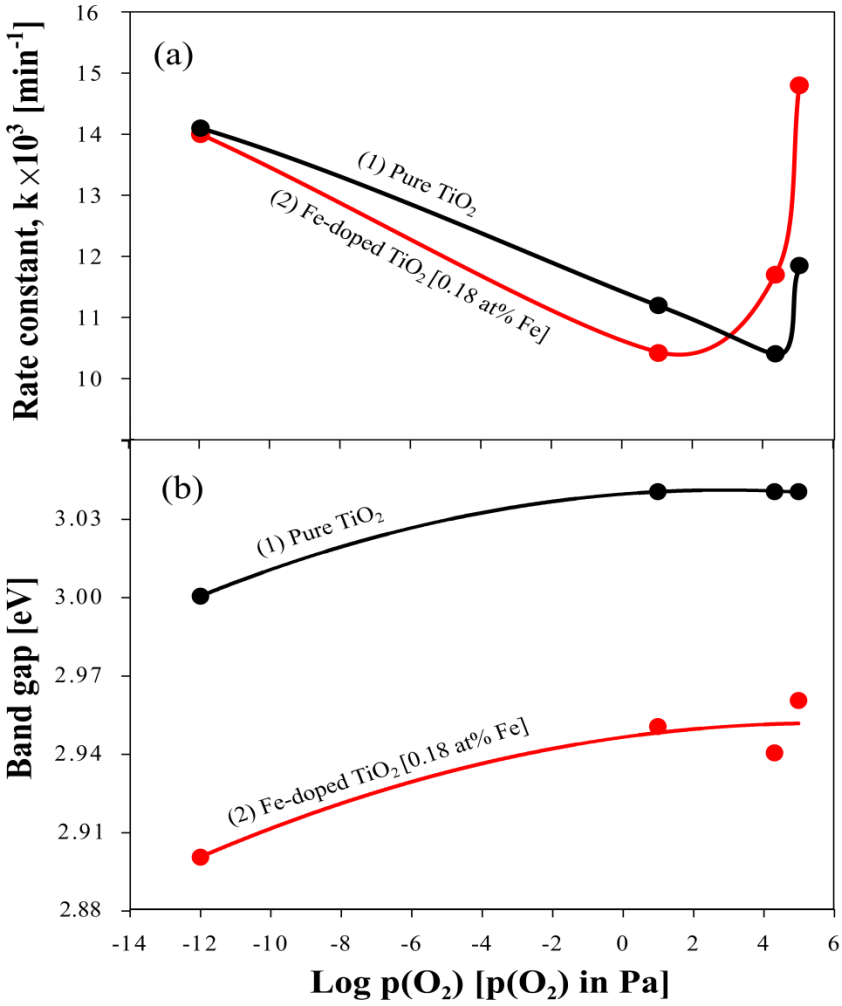

Figure 5-27: The effect of oxygen activity on the photocatalytic activity (a) and band gap (b) of pure and Fe-doped TiO_2 (0.18 at%) annealed in different oxygen activities at 1273 K for 24 hours.

5.4.2 Schematic representation of the effect of oxygen activity on photocatalytic activity of Fe-doped TiO_2

Figure 5-28 shows the schematic diagram explaining the effect of oxygen activity on the photocatalytic performance of Fe-doped TiO_2, which considers both reducing and oxidising conditions. It is known that annealing of TiO_2 in oxidising conditions results in an imposition of negative surface charge that is related to the presence of low-mobile titanium vacancies, which are the predominant species at the surface [5].

Incorporation of a small amount of iron into TiO_2 does not change this effect significantly; therefore in this case, the concentration of titanium vacancies also increases with the increase of oxygen activity. Additionally, iron ions substituting titanium ions in their lattice positions can act as active sites for water oxidation, further enhancing photocatalytic activity. On the other end of oxygen activities, photocatalytic performance is elevated as well, because the decrease of oxygen activity increases the charge transport. The poorest photocatalytic performance is observed for the specimens processed in the conditions corresponding to the n-p transition point where the concentration of charge carriers is the lowest.

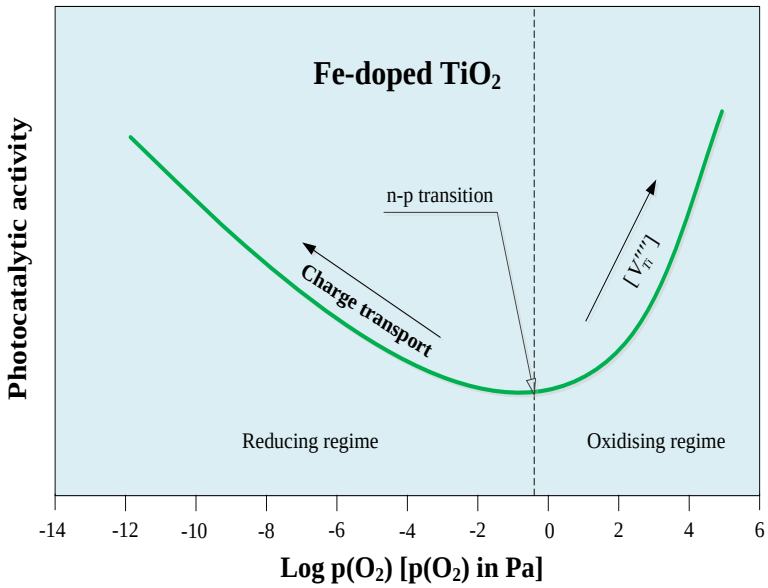

Figure 5-28: The schematic representation of the effect of oxygen activity on photocatalytic activity of Fe-doped TiO_2.

References

1. Albetran, H., B. O'Connor, and I. Low, *Effect of calcination on band gaps for electrospun titania nanofibers heated in air–argon mixtures.* Materials & Design, 2016. **92**: p. 480-485.

2. Castro, C.A., A. Centeno, and S.A. Giraldo, *Iron promotion of the TiO_2 photosensitization process towards the photocatalytic oxidation of azo dyes*

under solar-simulated light irradiation. Materials Chemistry and Physics, 2011. **129**(3): p. 1176-1183.

3. Mangham, A.N., et al., *Photochemical properties, composition, and structure in molecular beam epitaxy grown Fe "doped" and (Fe, N) codoped rutile TiO_2 (110).* The Journal of Physical Chemistry C, 2011. **115**(31): p. 15416-15424.

4. Korotcenkov, G., *Handbook of gas sensor materials-Properties, Advantages and Shortcomings for Applications.* Springer, 2013. **1**.

5. Bak, T., et al., *Photocatalytic Properties of TiO_2: Evidence of the Key Role of Surface Active Sites in Water Oxidation.* The Journal of Physical Chemistry A, 2015. **119**(36): p. 9465-9473.

6. Fàbrega, C., et al., *Location and catalytic role of iron species in TiO_2:Fe photocatalysts: An EPR study.* Journal of Photochemistry and Photobiology A: Chemistry, 2010. **211**(2–3): p. 170-175.

7. Castro, A.L., et al., *Doped titanium dioxide nanocrystalline powders with high photocatalytic activity.* Journal of Solid State Chemistry, 2009. **182**(7): p. 1838-1845.

8. Li, Z., et al., *Effect of Fe-doped TiO_2 nanoparticle derived from modified hydrothermal process on the photocatalytic degradation performance on methylene blue.* Journal of Hazardous Materials, 2008. **155**(3): p. 590-594.

9. Pal, B., et al., *Photocatalytic degradation of o-cresol sensitized by iron–titania binary photocatalysts.* Journal of Molecular Catalysis A: Chemical, 2001. **169**(1-2): p. 147-155.

10. Fan, L., J. Dongmei, and M. Xueming, *The effect of milling atmospheres on photocatalytic property of Fe-doped TiO_2 synthesized by mechanical alloying.* Journal of Alloys and Compounds, 2009. **470**(1–2): p. 375-378.

CHAPTER SIX

6 Comparative effects of oxygen activity on the segregation-induced concentration gradients of solutes in TiO_2. Data comparison for Cr-doped TiO_2 and Fe-doped TiO_2

The segregation-induced concentration profiles in **Figure 6-1** indicate that the increase of oxygen activity leads to entirely different effects for Cr-doped TiO_2 and Fe-doped TiO_2:

(i) The results reported by Rahman et al., 2018 [1] indicate the increase of chromium surface concentration, and

(ii) The results determined in this work attest a decrease of iron surface concentration.

The dissimilar effects result from different influence of oxygen activity on ionisation degree of chromium and iron in the surface layer of TiO_2. While iron is incorporated into the cation sublattice of the surface as two- or tri-valent ions forming acceptors, chromium is forming both tri and hexavalent ionic species, while the concentration of Cr^{6+} ions increase with the increase of oxygen activity leading, consequently, to the formation of donor-type defects. The data in **Figure 6-1** also show that segregation-induced enrichment factor is much stronger for single crystals [2] than that for polycrystalline specimens for both Cr- and Fe-doped TiO_2. This effect is reflective of the retarding effect of grain boundaries in polycrystalline specimens.

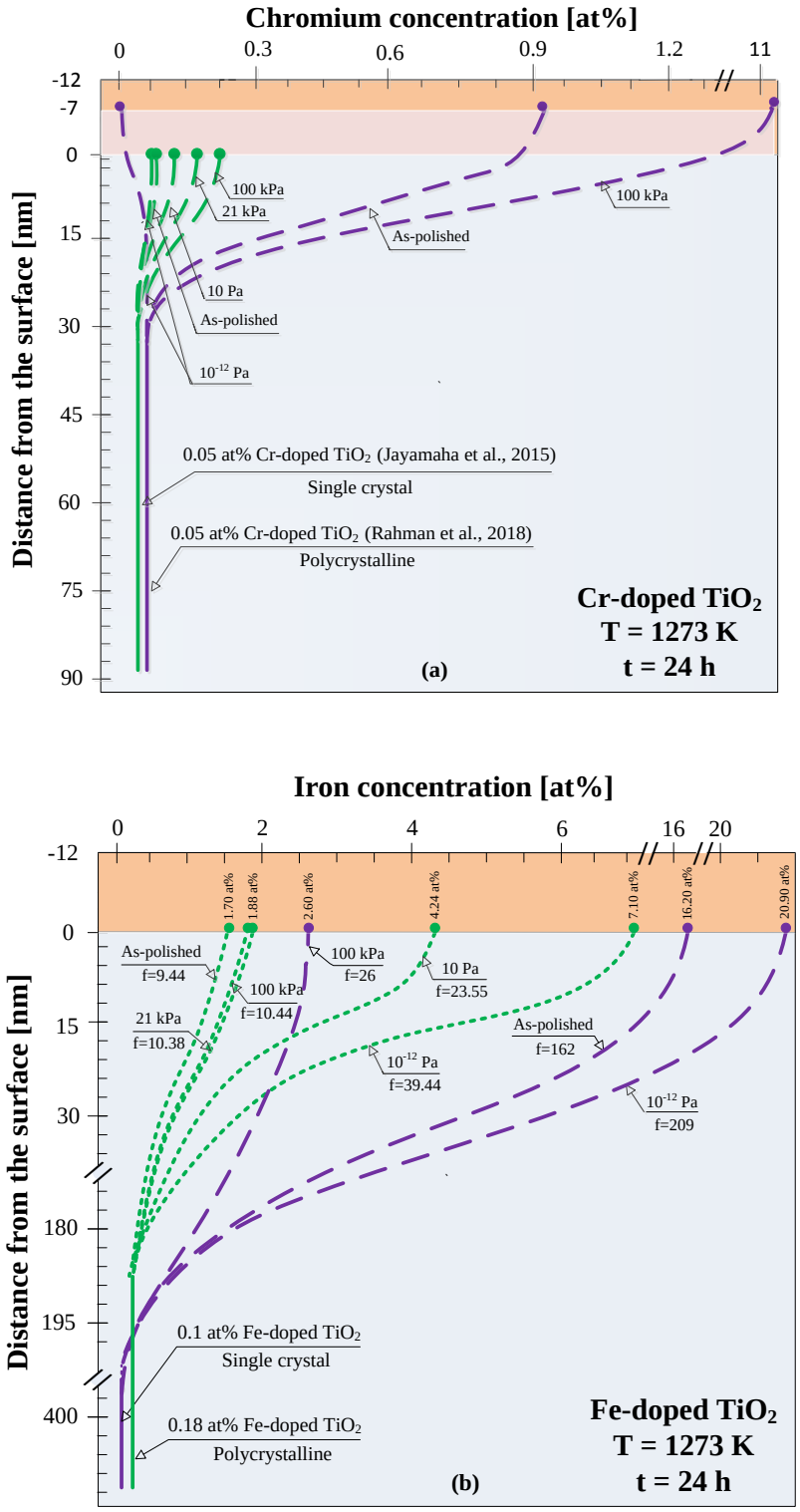

Figure 6-1: Comparative representation of the effect of oxygen activity on surface vs. bulk concentration of (a) chromium [1, 2] and (b) iron according to SIMS analysis. The results in the shaded outermost gold affected surface layer are not taken into account.

References

1. Rahman, K.A., et al., *Towards sustainable energy: photocatalysis of Cr-doped TiO_2. 5. Effect of segregation on surface versus bulk composition.* Ionics, 2018. **24**(4): p. 1211-1219.

2. Jayamaha, U., et al., *Effect of oxygen activity on chromium segregation in Cr-doped TiO_2 single crystal.* Ionics, 2015. **21**(3): p. 785-790.

CHAPTER SEVEN

7 Summary and conclusions

The present project, which is a part of the WSU PhD research program on POSs materials for solar energy conversion, studied the effect of point defects and the related properties of TiO_2-based semiconductors, including electronic structure and segregation on photocatalytic activity. The applied experimental procedures aimed at the modification of defect disorder in two ways:

(i) By incorporation of iron into TiO_2 lattice, and

(ii) By modification of oxygen activity leading to alteration of intrinsic defect disorder.

The project resulted in the following findings:

(1) Establishment of the effect of iron concentration on electronic structure of TiO_2

1.1 The incorporation of iron into TiO_2 lattice at $p(O_2)$ = 21 kPa results in a reduction of the band gap from 3.04 eV for pure TiO_2 to 2.78 eV for 1.4 at% Fe-doped TiO_2 (**Figure 5-3**).

1.2 Isothermal increase of oxygen activity results in an insignificant increase of the band gap for Fe-doped TiO_2 from 2.90 eV at 10^{-12} Pa to 2.96 eV at 100 kPa (**Figure 5-6**).

1.3 Incorporation of iron results in the formation of an acceptor energy level located at 0.71 eV - 0.73 eV above the valence band (**Figure 5-2**).

(2) Determination of the effect of segregation on surface vs. bulk composition of iron-doped TiO_2

2.1 The segregation-induced concentration of iron at the surface of Fe-doped TiO_2 increases to a level greatly above the bulk iron concentration (**Figure 5-11a**). This work also determined the related segregation-induced iron enrichment factor (**Figure 5-11b**) which has a tendency to increase with the decrease of bulk iron concentration (except of the most diluted solid solution).

2.2 The segregation-induced concentration of iron at the surface of Fe-doped TiO_2 varies with oxygen activity (**Figure 5-17**). The increase of oxygen activity results in a substantial decrease of iron concentration for the single crystal (**Figure 5-17**, **1**). The effect for the polycrystalline specimen is insignificant (**Figure 5-17**, **2** and **3**).

2.3 The surface ratio of di- to tri-valent iron species for Fe-doped TiO_2 at $p(O_2) = 10^{-12}$ Pa assumes a maximum value ($Fe^{2+}/Fe^{3+} = 1.63$). This ratio decreases with the increase of oxygen activity to the level of $Fe^{2+}/Fe^{3+} = 0.39$ at 100 kPa (**Figure 5-13**).

(3) Establishment of the photocatalytic activity of iron-doped TiO_2

3.1 Oxidising condition. The increase of iron concentration up to 0.09 at% Fe of bulk concentration (1.8 at% Fe at the surface) results in an initial increase of photocatalytic activity. Further increase of iron concentration results in a decrease of photocatalytic activity (**Figure**

5-21, **a-1**). The latter effect is observed despite the continuing band gap reduction with the increase of iron concentration (**Figure 5-22**, **b-1**).

3.2 ***Reducing condition.*** The increase of iron concentration results in a decrease of photocatalytic activity within the entire range of iron concentrations (**Figure 5-22**, **a-2**) regardless of the reduced band gap (**Figure 5-21**, **b-2**).

3.3 ***Variable oxygen activity.*** The photocatalytic activity of Fe-doped TiO_2 assumes the largest value for the specimens annealed in the gas phase of $p(O_2)$ = 100 kPa and minimum for the specimens processed at oxygen activities corresponding to the n-p transition point [10 Pa < $p(O_2)$ < 10^5 Pa]. The decrease of $p(O_2)$ below that corresponding to the n-p transition point results in an increase of photocatalytic activity (**Figure 5-27**, **a-2**).

(4) Derivation of theoretical models on several properties of iron-doped TiO_2

4.1 Electronic structure. The derived band model describes the effect of iron concentration on the electronic structure of TiO_2, including the position of the iron energy level and the related band gap (**Figure 5-7**).

4.2 Effect of segregation. The derived model describes the effect of surface charge of Fe-doped TiO_2 on the transport of charged iron species from bulk to surface or vice versa due to segregation-induced electrostatic field generated by non-uniform distribution of charged native defects (**Table 5-1**).

4.3 Photocatalytic activity. The reaction mechanism between the surface active sites (anodic and cathodic) of Fe-doped TiO_2 with water and associated charge transfer is described by two alternative models:

(i) Iron is incorporated into interstitial sites leading to the formation of positively charged iron species, which act as cathodic surface active sites, and anodic surface active sites which are titanium vacancies (**Figure 5-22a**). The enhanced photocatalytic activity is influenced by the concentration of titanium vacancies.

(ii) Iron ions located in titanium sites exhibit negative effective charge and are compensated by oxygen vacancies (**Figure 5-22b)**. At the surface, this acceptor-type defects act as anodic active sites.

(iii) The incorporation of iron above 0.09 at% Fe results in the formation of defect complexes, which exhibit reduced photocatalytic activity (**Figure 5-23**).